

University of Windsor

Scholarship at UWindor

Electronic Theses and Dissertations

Theses, Dissertations, and Major Papers

2009

Experimental determination of the yield locus of anisotropic metal sheets using digital image correlation

Neil D. Turton
University of Windsor

Follow this and additional works at: <https://scholar.uwindsor.ca/etd>

Recommended Citation

Turton, Neil D., "Experimental determination of the yield locus of anisotropic metal sheets using digital image correlation" (2009). *Electronic Theses and Dissertations*. 7930.
<https://scholar.uwindsor.ca/etd/7930>

This online database contains the full-text of PhD dissertations and Masters' theses of University of Windsor students from 1954 forward. These documents are made available for personal study and research purposes only, in accordance with the Canadian Copyright Act and the Creative Commons license—CC BY-NC-ND (Attribution, Non-Commercial, No Derivative Works). Under this license, works must always be attributed to the copyright holder (original author), cannot be used for any commercial purposes, and may not be altered. Any other use would require the permission of the copyright holder. Students may inquire about withdrawing their dissertation and/or thesis from this database. For additional inquiries, please contact the repository administrator via email (scholarship@uwindsor.ca) or by telephone at 519-253-3000ext. 3208.

NOTE TO USERS

This reproduction is the best copy available.

UMI[®]



EXPERIMENTAL DETERMINATION OF THE YIELD LOCUS OF ANISOTROPIC METAL SHEETS USING DIGITAL IMAGE CORRELATION

By

Neil D. Turton

A Thesis

Submitted to the Faculty of Graduate Studies
through Mechanical, Automotive, & Materials Engineering
in Partial Fulfillment of the Requirements for
the Degree of Master of Applied Science at the
University of Windsor

Windsor, Ontario, Canada

2009

© 2009 Neil D. Turton



Library and Archives
Canada

Published Heritage
Branch

395 Wellington Street
Ottawa ON K1A 0N4
Canada

Bibliothèque et
Archives Canada

Direction du
Patrimoine de l'édition

395, rue Wellington
Ottawa ON K1A 0N4
Canada

Your file *Votre référence*
ISBN: 978-0-494-57613-7
Our file *Notre référence*
ISBN: 978-0-494-57613-7

NOTICE:

The author has granted a non-exclusive license allowing Library and Archives Canada to reproduce, publish, archive, preserve, conserve, communicate to the public by telecommunication or on the Internet, loan, distribute and sell theses worldwide, for commercial or non-commercial purposes, in microform, paper, electronic and/or any other formats.

The author retains copyright ownership and moral rights in this thesis. Neither the thesis nor substantial extracts from it may be printed or otherwise reproduced without the author's permission.

AVIS:

L'auteur a accordé une licence non exclusive permettant à la Bibliothèque et Archives Canada de reproduire, publier, archiver, sauvegarder, conserver, transmettre au public par télécommunication ou par l'Internet, prêter, distribuer et vendre des thèses partout dans le monde, à des fins commerciales ou autres, sur support microforme, papier, électronique et/ou autres formats.

L'auteur conserve la propriété du droit d'auteur et des droits moraux qui protègent cette thèse. Ni la thèse ni des extraits substantiels de celle-ci ne doivent être imprimés ou autrement reproduits sans son autorisation.

In compliance with the Canadian Privacy Act some supporting forms may have been removed from this thesis.

While these forms may be included in the document page count, their removal does not represent any loss of content from the thesis.

Conformément à la loi canadienne sur la protection de la vie privée, quelques formulaires secondaires ont été enlevés de cette thèse.

Bien que ces formulaires aient inclus dans la pagination, il n'y aura aucun contenu manquant.


Canada

Author's Declaration of Originality

I hereby certify that I am the sole author of this thesis and that no part of this thesis has been published or submitted for publication.

I certify that, to the best of my knowledge, my thesis does not infringe upon anyone's copyright nor violate any proprietary rights and that any ideas, techniques, quotations, or any other material from the work of other people included in my thesis, published or otherwise, are fully acknowledged in accordance with the standard referencing practices. Furthermore, to the extent that I have included copyrighted material that surpasses the bounds of fair dealing within the meaning of the Canada Copyright Act, I certify that I have obtained a written permission from the copyright owner(s) to include such material(s) in my thesis and have included copies of such copyright clearances to my appendix.

I declare that this is a true copy of my thesis, including any final revisions, as approved by my thesis committee and the Graduate Studies office, and that this thesis has not been submitted for a higher degree to any other University or Institution.

Abstract

The focus of this research was to determine the yielding and work hardening behaviour of two anisotropic steel sheets (DP600 and HSLA). Uniaxial tension and compression tests were performed in the rolling and transverse directions and at 45 degrees to the rolling direction for each sheet. Plane-strain tension tests were carried out along the rolling and transverse directions. Digital image correlation was used to determine the strain distribution throughout the gauge region.

The stress-strain response of the plane-strain tension specimen was estimated through a comparison of the experimental and numerically predicted load-strain response.

Yield stresses in uniaxial tension were obtained for various yield offsets, and R-values were obtained, allowing for the anisotropy of each steel sheet to be determined. Yield data was also obtained in plane-strain and equibiaxial tension, pure shear, and uniaxial compression for corresponding values of plastic work per unit volume from the stress-strain response.

Hill's 1948 R-based and stress-based yield criteria, Hill's 1979 planar-isotropic yield criterion and Barlat's Yld2000-2d yield function were evaluated at each value of plastic work per unit volume, and compared against the experimental yield data obtained.

A low degree of anisotropy was noted for both materials. While all yield functions provided similar results for DP600, it was noted that Hill's 1948 R-based criterion and Hill's 1979 yield criterion were unable to accurately predict material behaviour for all yield offsets for HSLA. It was found that Barlat's Yld2000-2d provided the most accurate representation of the experimental data.

To my family and friends for their encouragement and support

Acknowledgements

I would like to express my sincere appreciation and gratitude to Dr. D. E. Green for his guidance and support over the course of this study. His assistance over the course of my research has been invaluable.

I would also like to thank my committee members for their support, especially Dr. W. Altenhof for his assistance with the development of the numerical model.

The assistance of the laboratory technicians, Mr. A. Jenner, Mr. L. Pop, Mr. M. St Louis, and Mr. P. Seguin is greatly appreciated. The assistance of Mr. A. Jenner in specimen preparation is especially appreciated.

Finally, I would like to thank my fellow researchers, including Mr. A. Taherizadeh, Mr. A. Ghaei, and Mr. H. An for their assistance over the course of the study.

Table of Contents

AUTHOR'S DECLARATION OF ORIGINALITY	iii
ABSTRACT.....	iv
DEDICATION.....	v
ACKNOWLEDGEMENTS.....	vi
LIST OF TABLES.....	x
LIST OF FIGURES.....	xii
LIST OF SYMBOLS.....	xvii
1 . INTRODUCTION.....	1
2 . LITERATURE REVIEW	5
2.1 PLASTIC ANISOTROPIC COEFFICIENT.....	5
2.2 ANISOTROPIC YIELD FUNCTIONS.....	6
2.2.1 Hill's 1948 criterion	7
2.2.2 Hill's 1979 criterion	8
2.2.3 YLD2000-2d	9
2.3 EXPERIMENTAL DETERMINATION OF THE YIELD LOCUS.....	11
2.3.1 Plane-strain tension	12
2.3.2 Equibiaxial tension	13
2.3.3 Uniaxial compression.....	15
2.3.4 Pure shear	17
2.4 DIGITAL IMAGE CORRELATION.....	19
3 . EXPERIMENTAL PROCEDURES.....	21
3.1 TEST SPECIMENS.....	21
3.1.1 Material grades	21

3.1.2	Specimen geometries.....	22
3.1.3	Specimen preparation.....	25
3.2	TESTING PROCEDURES	27
3.2.1	Testing equipment	27
3.2.2	System calibration.....	28
3.2.3	Strain measurement accuracy	30
3.2.4	Testing procedure	31
3.2.5	Numerical analysis of plane-strain tension tests	34
3.3	OUTSOURCED TESTS.....	36
3.4	ANALYSIS OF DATA	37
4	RESULTS AND DISCUSSION.....	39
4.1	UNIAXIAL TENSION RESULTS	39
4.1.1	DP600.....	39
4.1.2	HSLA	43
4.2	NUMERICAL PREDICTION OF PLANE-STRAIN TENSION BEHAVIOUR.....	47
4.2.1	DP600.....	48
4.2.2	HSLA	54
4.3	EXPERIMENTAL PLANE-STRAIN TENSION RESULTS	61
4.3.1	DP600.....	61
4.3.2	HSLA	65
4.4	UNIAXIAL COMPRESSION RESULTS	70
4.5	OUTSOURCED TEST RESULTS.....	72
4.6	YIELD FUNCTIONS.....	76
4.6.1	DP600.....	88
4.6.2	HSLA	93

5 . CONCLUSION.....	99
APPENDIX A. ARAMIS SPECIFICATIONS	101
APPENDIX B. PLANE-STRAIN ANALYSIS.....	104
APPENDIX C. OUTSOURCED STRESS-STRAIN RESULTS.....	113
REFERENCES.....	120
VITA AUCTORIS	124

List of Tables

Table 1 Flow stress of DP600 tensile specimens tested in the rolling direction for various values of plastic strain offset and corresponding values of plastic work per unit volume.....	42
Table 2 Flow stress of DP600 tensile specimens tested at 45 degrees to the rolling direction for various values of plastic strain offset and corresponding values of plastic work per unit volume.....	42
Table 3 Flow stress of DP600 tensile specimens tested at 90 degrees to the rolling direction for various values of plastic strain offset and corresponding values of plastic work per unit volume.....	43
Table 4 Flow stress of HSLA tensile specimens tested in the rolling direction for various values of plastic strain offset and corresponding values of plastic work per unit volume.....	46
Table 5 Flow stress of HSLA tensile specimens tested at 45 degrees to the rolling direction for various values of plastic strain offset and corresponding values of plastic work per unit volume.....	46
Table 6 Flow stress of HSLA tensile specimens tested at 90 degrees to the rolling direction for various values of plastic strain offset and corresponding values of plastic work per unit volume.....	47
Table 7 Flow stress in DP600 plane-strain specimens loaded in the sheet rolling direction	64
Table 8 Flow stress in DP600 plane-strain specimens loaded in the sheet transverse direction.....	65
Table 9 Flow stress in HSLA plane-strain specimens loaded in the sheet rolling direction.....	69
Table 10 Flow stress in HSLA plane-strain specimens loaded in the sheet transverse direction.....	70
Table 11 Flow stress in DP600 uniaxial compression specimens loaded in the sheet rolling direction.....	71
Table 12 Flow stress in DP600 uniaxial compression specimens loaded at 45 degrees to the sheet rolling direction.....	72
Table 13 Flow stress in DP600 uniaxial compression specimens loaded at 90 degrees to the sheet rolling direction.....	72
Table 14 Flow stress in DP600 uniaxial compression specimens loaded in the sheet rolling direction.....	73
Table 15 Flow stress in DP600 uniaxial compression specimens loaded at 90 degrees to the sheet rolling direction.....	73
Table 16 Flow stress in HSLA uniaxial compression specimens loaded in the sheet rolling direction.....	73

Table 17 Flow stress in HSLA uniaxial compression specimens loaded at 90 degrees to the sheet rolling direction.....	74
Table 18 Equibiaxial tension stress coefficients	74
Table 19 Flow stress in DP600 equibiaxial tension specimens.....	75
Table 20 Flow stress in HSLA equibiaxial tension specimens	75
Table 21 DP600 - Simple shear yield values.....	76
Table 22 HSLA - Simple shear yield values.....	76
Table 23 Anisotropy coefficients for Hill's 1948 stress-based yield function.....	88
Table 24 Anisotropy coefficients for Barlat's Yld2000-2d	89
Table 25 Anisotropy coefficients for Hill's 1948 stress-based yield function.....	94
Table 26 Anisotropy coefficients for Barlat's Yld2000-2d	94
Table A.1 Calibration parameters.....	102

List of Figures

Figure 1.1 Schematic of advanced high strength steels, high strength steels, and mild steels	2
Figure 2.1 Schematic of cold rolling process showing rolling (X) and transverse (Y) directions	5
Figure 2.2 Effect of m coefficient on yield function	9
Figure 2.3 Yield locus representing key points for measurement	11
Figure 2.4 Strain distribution of major and minor strain in plane-strain test	12
Figure 2.5 a) Wagoner's 'H' design for plane-strain specimen b) Wagoner's 'B' design for plane-strain specimen.....	13
Figure 2.6 Cruciform specimen.....	14
Figure 2.7 Methods for compression testing.....	17
Figure 2.8 Geometry of pure shear specimen	18
Figure 2.9 Simple shear device developed at the Université de Bretagne-Sud.....	18
Figure 3.1 Uniaxial tension specimen corresponding to ASTM Standard E8M	23
Figure 3.2 Uniaxial compression specimen	24
Figure 3.3 Plane-strain specimen.....	25
Figure 3.4 Plane-strain specimen prepared for analysis using ARAMIS system.....	26
Figure 3.5 Plane-strain tension clamps.....	28
Figure 3.6 Calibration panel	29
Figure 3.7 (A) Location of ARAMIS strain measurements on specimen (B) Stress-strain profiles from ARAMIS and extensometer	31
Figure 3.8 Experimental set-up for uniaxial tension test with ARAMIS cameras	32
Figure 3.9 Experimental set-up for plane-strain tension tests	33
Figure 3.10 Experimental set-up for uniaxial compression tests	34
Figure 3.11 Numerical model of plane strain specimen.....	35
Figure 4.1 Engineering stress-strain behaviour of DP600 in uniaxial tension	40
Figure 4.2 True stress-true strain behaviour of DP600 in uniaxial tension	40

Figure 4.3 Distribution of the true major strains in the gauge area of DP600 uniaxial tension specimens	41
Figure 4.4 Engineering stress-strain behaviour of HSLA in uniaxial tension.....	44
Figure 4.5 True stress-true strain behaviour of HSLA in uniaxial tension.....	44
Figure 4.6 Distribution of the true major strains in the gauge area of HSLA uniaxial tension specimens	45
Figure 4.7 Load-Stress behaviour of DP600 specimens in plane-strain tension obtained from numerical analysis.....	48
Figure 4.8 Numerical prediction of stress-strain behaviour for DP600 specimen subjected to plane-strain tension in the rolling direction before and after scaling	49
Figure 4.9 Estimated stress-strain behaviour of DP600 in plane-strain tension	50
Figure 4.10 Comparison of the plane-strain behaviour of DP600 in the rolling direction as predicted by the Wagoner analysis method and by scaling the curves obtained from finite element simulation	51
Figure 4.11 Comparison of the plane-strain behaviour of DP600 at 90 degrees to the rolling direction as predicted by the Wagoner analysis method and by scaling the curves obtained from finite element simulation.....	52
Figure 4.12 (A) Major and (a) minor strain distribution in DP600 plane-strain specimen predicted with LS-Dyna	53
Figure 4.13 Distribution of major and minor true strains computed across the width of the gauge for numerical model of plane-strain DP600 specimen loaded in the rolling direction.	54
Figure 4.14 Load-stress behaviour of HSLA specimens in plane-strain tension obtained from numerical analysis.....	55
Figure 4.15 Numerical results for HSLA specimen in rolling direction before and after scaling in rolling direction.....	56
Figure 4.16 Estimated true stress-true strain behaviour of HSLA in plane-strain tension.	57
Figure 4.17 Comparison of the plane-strain behaviour of HSLA in the rolling direction as predicted by the Wagoner analysis method and by scaling the curves obtained from finite element simulation	58
Figure 4.18 Comparison of the plane-strain behaviour of HSLA at 90 degrees to the rolling direction as predicted by the Wagoner analysis method and by scaling the curves obtained from finite element simulation.....	59

Figure 4.19 (A) Major and (a) minor strain distribution in DP600 plane-strain specimen predicted with LS-Dyna	59
Figure 4.20 Distribution of axial major and minor true strains computed across the width of the gauge for numerical model of plane-strain HSLA specimen loaded in the rolling direction.	60
Figure 4.21 Distribution of axial major and minor engineering strains measured across the width of the gauge for plane-strain DP600 specimens loaded in the rolling direction.	61
Figure 4.22 Distribution of axial major and minor engineering strains measured across the width of the gauge for plane-strain DP600 specimens loaded at 90 degrees to the rolling direction.	62
Figure 4.23 Distribution of (A-D) axial and (a-d) transverse true strains measured in the gauge area of DP600 plane-strain specimens	64
Figure 4.24 Distribution of axial major and minor engineering strains measured across the width of the gauge for plane-strain HSLA specimens loaded in the rolling direction.	66
Figure 4.25 Distribution of axial major and minor engineering strains measured across the width of the gauge for plane-strain HSLA specimens loaded at 90 degrees to the rolling direction.	67
Figure 4.26 Distribution of axial (A-D) and transverse (a-d) true strains measured in the gauge area of HSLA plane-strain specimens	69
Figure 4.27 Engineering stress-strain response of DP600 specimens loaded in uniaxial compression.....	71
Figure 4.28 DP600 yield loci for plastic work value of 0.870 MJ/m^3 (0.2% plastic strain offset in uniaxial tension).....	78
Figure 4.29 DP600 yield loci for plastic work value of 2.30 MJ/m^3 (0.5% plastic strain offset in uniaxial tension).....	79
Figure 4.30 DP600 yield loci for plastic work value of 4.95 MJ/m^3 (1.0% plastic strain offset in uniaxial tension).....	80
Figure 4.31 DP600 yield loci for plastic work value of 10.7 MJ/m^3 (2.0% plastic strain offset in uniaxial tension).....	81
Figure 4.32 DP600 yield loci for plastic work value of 30.4 MJ/m^3 (5.0% plastic strain offset in uniaxial tension).....	82
Figure 4.33 HSLA yield loci for plastic work value of 0.918 MJ/m^3 (0.2% plastic strain offset in uniaxial tension).....	83
Figure 4.34 HSLA yield loci for plastic work value of 4.22 MJ/m^3 (1.0% plastic strain offset in uniaxial tension).....	84

Figure 4.35 HSLA yield loci for plastic work value of 8.34 MJ/m ³ (2.0% plastic strain offset in uniaxial tension).....	85
Figure 4.36 HSLA yield loci for plastic work value of 20.9 MJ/m ³ (5.0% plastic strain offset in uniaxial tension).....	86
Figure 4.37 HSLA yield loci for plastic work value of 44.4 MJ/m ³ (10.0% plastic strain offset in uniaxial tension).....	87
Figure 4.38 Yield loci in σ_1, σ_2 quadrant with error bars.....	91
Figure 4.39 Comparison of experimental flow stresses to stresses predicted using yield functions for plane-strain specimen in transverse direction.....	92
Figure 4.40 Comparison of experimental flow stresses to stresses predicted using yield functions for simple shear.....	93
Figure 4.41 Comparison of Yld2000-2d plane strain prediction to experimental results.....	96
Figure 4.42 Comparison of experimental flow stresses to stresses predicted using yield functions for plane-strain specimen in transverse direction.....	97
Figure 4.43 Comparison of experimental flow stresses to stresses predicted using yield functions for simple shear.....	98
Figure A.1 Calibration set-up.....	102
Figure A.2 True stress-true strain behaviour of DP600 in uniaxial compression (provided by Dr Wagoner, Ohio State University).....	114
Figure A.3 True stress-true strain behaviour of HSLA in uniaxial compression (provided by Dr Wagoner, Ohio State University).....	114
Figure A.4 Experimental true stress-true strain behaviour of DP600 in equibiaxial tension (provided by Dr Yoon, Alcoa Technical Centre).....	115
Figure A.5 Equibiaxial work hardening behaviour of DP600 described by Hollomon's law and fitted to experimental data.....	116
Figure A.6 Equibiaxial work hardening behaviour of DP600 described by Voce's law and fitted to experimental data.....	116
Figure A.7 Experimental true stress-true strain behaviour of HSLA in equibiaxial tension (provided by Dr Yoon, Alcoa Technical Centre).....	117
Figure A.8 Equibiaxial work hardening behaviour of HSLA described by Hollomon's law and fitted to experimental data.....	118

Figure A.9 Equibiaxial work hardening behaviour of HSLA described by Voce's law and fitted to experimental data.....118

Figure A.10 True stress-true strain behaviour of DP600 in pure shear (provided by Dr. Thuillier, Université de Bretagne-Sud).....119

Figure A.11 True stress-true strain behaviour of HSLA in pure shear (provided by Dr. Thuillier, Université de Bretagne-Sud).....119

List of Symbols

Latin Symbols

a	material parameter for Barlat's Yld2000-2d
b	specimen thickness
C'_{ij}, C''_{ij}	anisotropy coefficients of Barlat's Yld2000-2d ($i=1-6, j=1-6$)
e	engineering strain
E	Young's modulus
F_{cr}	critical buckling force
F, G, H, N	anisotropy coefficients of Hill's 1948 stress-based yield criterion
f, g, h	anisotropy coefficients of Hill's 1979 yield criterion
h	specimen height (in mass moment of inertia)
H	height of calibrated volume
I	second mass moment of inertia
L	length of calibrated volume
l	gauge length
l_0	initial gauge length
m	material characteristic in Hill's 1979 yield criterion
R_i	plastic anisotropic coefficient, where i represents the angle with respect to rolling direction
R_{be}	plastic anisotropic coefficient in equibiaxial tension
\bar{R}	normalized anisotropic coefficient
s_{ij}	deviatoric stress components ($i=x,y, j=x,y$)
t	specimen thickness
t_0	initial specimen thickness
W	width of calibrated volume
w	specimen width
w_0	initial specimen width
X'_i, X''_i	principal values of stress deviation tensors ($i=1,2$)
X'_{ii}, X''_{ii}	components of X'_i and X''_i ($i=1,2$)

Greek Symbols

α_i	anisotropy coefficients in Barlat's Yld2000-2d (i=1-8)
ε	true strain
ε_1	major strain
ε_2	minor strain
ε_L	strain in the rolling direction
ε_T	strain in the transverse direction
$\bar{\sigma}_{eff}$	effective stress
σ_0	yield stress in uniaxial tension in the rolling direction
σ_1	major principal stress
σ_2	minor principal stress
σ_{Eng}	engineering stress
σ_L	stress in the rolling direction
σ_T	stress in the transverse direction
σ_{True}	true stress
σ_x	stress in rolling direction
σ_y	stress in transverse direction
σ_z	stress through specimen thickness
$\sigma_{xy}, \sigma_{xz}, \sigma_{yz}$	shear stresses

1. INTRODUCTION

During the 1970's, oil shortages in the United States prompted the National Highway Traffic Administration to establish Corporate Average Fuel Economy (CAFE) regulations in order to improve the fuel economy of passenger cars and light trucks. One method that contributed towards this was the reduction of vehicle mass.

In the 1990's, many factors, including increased safety and environmental regulations, and increased comfort and performance requirements from customers resulted in mass increases compared to previous generation vehicles. Systems such as reinforced body structures and driver assistance systems result in additional components and increased mass. An increase in automobile mass has many undesirable effects including increased fuel consumption and vehicle emissions.

In 1998, the UltraLight Steel Auto Body (ULSAB) report [1, 2] was released, detailing the results of work to reduce automobile mass, while increasing safety performance. Mass reductions result in increased fuel efficiency, and a reduction in toxic emissions. The ULSAB Consortium achieved this through the introduction of a new generation of steel grades and advanced manufacturing processes.

One contribution to the reduction of vehicle mass was the introduction of advanced high strength steels (AHSS) into the body and structure. Due to their increased strength, AHSS allow for a reduction in thickness of sheet metal components without compromising impact resistance: this down-gauging leads to a decrease in the mass of vehicle body-in-white compared to vehicles manufactured from conventional mild steel grades. Figure 1.1 indicates the relative strength and formability of advanced high strength steels (in colour), high strength steels (in light gray), and mild steels (in dark gray).

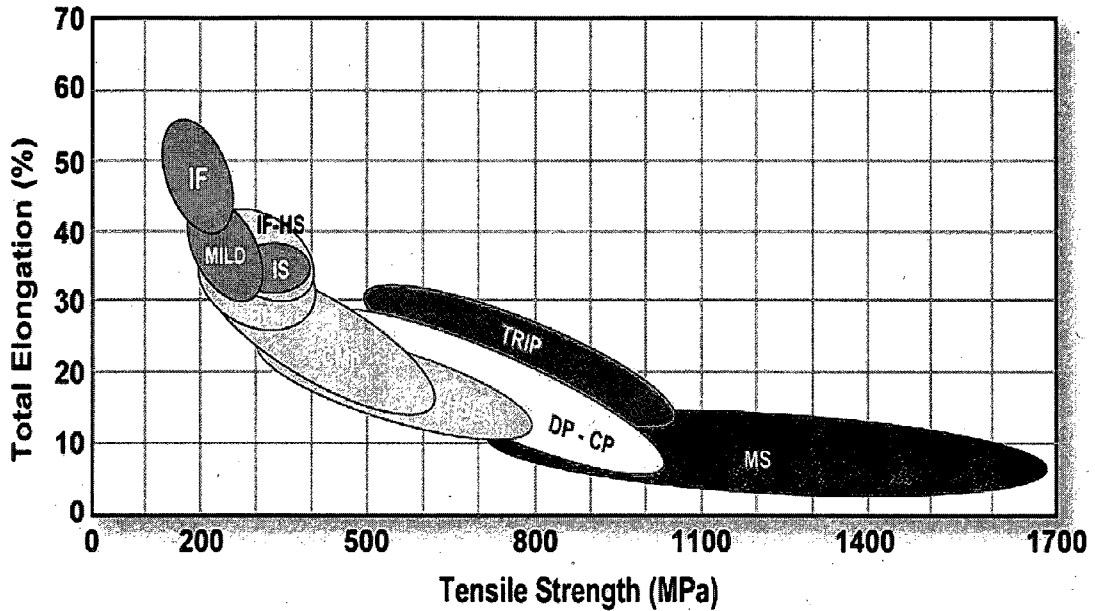


Figure 1.1: Schematic of advanced high strength steels, high strength steels, and mild steels [3]

Other technologies for achieving mass savings include the use of advanced manufacturing processes, such as hydroforming and tailor-welded blanking. Tailored blanking is a process in which steels of different strengths or thicknesses are laser welded to create an engineered blank that can then be stamped or drawn into shape. This allows for larger quantities of steel in desired areas while allowing for reduced steel quantities in areas where mass can safely be removed.

Hydroforming is a process in which hydraulic pressure is applied to a tube or sheet specimen in order to obtain a desired shape. Tubular hydroforming allows for the creation of variable cross-sections in a single tube allowing for a reduction in the number of required parts. Sheet hydroforming achieves improved surface quality through the use of hydraulic pressure, by eliminating metal-on-metal contact that exists in conventional stamping.

Through the implementation of advanced high strength steels and advanced manufacturing processes, the ULSAB Consortium was able to obtain mass reductions up to 25%, while providing

increased safety and maintaining manufacturing costs. Furthermore, the ULSAB design achieved an 80% increase in torsional stiffness, and a 50% increase in bending stiffness over benchmark vehicles.

One disadvantage with the implementation of advanced high strength steels is their increased springback after the forming process. Springback results from residual stresses which develop in a sheet metal during the stamping process, and causes a recovery of some of the elastic deformation that occurs during the forming process. In order to determine the desired final geometry, springback is predicted using finite element simulation. The geometry of the stamping dies is subsequently modified to compensate for the springback. This entire die design process is carried out virtually, as this reduces the time and costs associated with product development.

Another method for reducing costs associated with producing new vehicle models, is the creation of virtual models to predict the crash response of the automobile. Numerical modelling of automobile crash response allows analysis and improvement of component and system behaviour before physical prototypes are created. This results in a decrease in the number of prototype models required before a vehicle is commercially released. In order to accurately simulate the crash response of an automobile, many factors are considered. These include, but are not limited to, contact response, load application, and material behaviour.

The numerical simulations required to predict springback in individual components and those carried out to predict the vehicle response under dynamic impact loads are generally based on phenomenological models of material behaviour. Research conducted over the last few decades has contributed towards improving the accuracy of material models and thus enhancing the reliability of predictive simulations. Two of the most important elements of material models that are used to simulate the plastic behaviour of sheet metal are the yield function that describes the states of stress that lead to plastic deformation and a stress-strain relationship that describes the work hardening of the sheet material under consideration. It is essential to accurately model both these functions in order to correctly predict sheet metal behaviour.

The purpose of this research was to experimentally determine the yield locus of a dual-phase (DP600) steel sheet material and a more conventional high-strength low-alloy (HSLA) sheet steel. Both these sheet materials were used in Numisheet 2005 Benchmark #3 [4], and therefore a considerable body of experimental data already exists. However, in order to take advantage of this benchmark data to validate advanced material models more extensive material characterization is needed for these materials. These experimental yield loci will therefore expand the existing data set and enhance the value of this benchmark.

Chapter 2 provides an overview of anisotropy, including yield functions used to describe the yield behaviour of anisotropic materials, and experimental methods used to define key points on the anisotropic yield locus. An introduction to digital image correlation is also presented. Chapter 3 provides details of the experimental procedure used for defining the yield loci. The stress-strain response was obtained for uniaxial tension and uniaxial compression in the rolling and transverse directions, as well as at 45 degrees to the rolling direction. Moreover the stress-strain behaviour was also determined for plane strain tension in the rolling and transverse directions. Yield data were obtained from the stress-strain curves for all tests. The experimental yield data were then compared to theoretical anisotropic yield functions, and the most appropriate yield function was selected for each of these two sheet materials. Experimental results are presented and discussed in chapter 4, and chapter 5 provides conclusions obtained from this research.

2. LITERATURE REVIEW

This chapter provides an overview of the literature relevant to this study. Section 2.1 provides an overview of anisotropy, and discusses the plastic anisotropy coefficient. Section 2.2 discusses various yield functions used to describe the yield behaviour of anisotropic materials, including Hill's 1948 and 1978 yield functions and Barlat's Yld2000-2d. Section 2.3 provides an overview of experimental tests used for obtaining points on the yield locus of anisotropic materials. An overview of digital image correlation (DIC) is provided in Section 2.4.

2.1 PLASTIC ANISOTROPIC COEFFICIENT

Anisotropy is a characteristic of materials whose mechanical properties vary with orientation. Anisotropy typically results from the cold rolling of sheet metal, during which crystallographic texture develops to strengthen the sheet metal in certain directions. Figure 2.1 provides a schematic of the cold rolling process, showing the rolling and transverse directions.

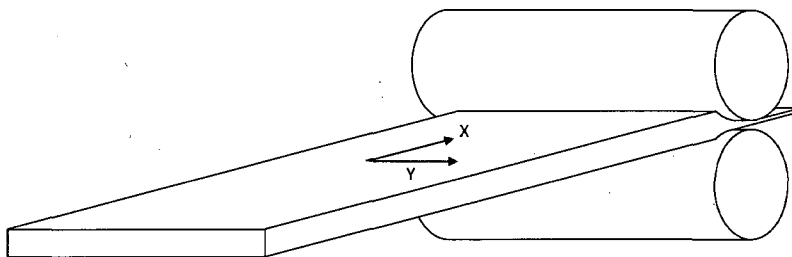


Figure 2.1 Schematic of cold rolling process showing rolling (X) and transverse (Y) directions

The degree of anisotropy can be described by the R-value, also known as Lankford's coefficient. The R-value is the width-to-thickness true strain ratio, typically obtained after 10 to 15% strain in uniaxial tension, and is defined in Equation 2.1.

$$R = \frac{\ln\left(\frac{w}{w_0}\right)}{\ln\left(\frac{t}{t_0}\right)} \quad (2.1)$$

Typical R-values range from 0.4 to 5 [5]. Since the thickness strain is difficult to measure, the R-value can also be obtained through Equation 2.2. [6]

$$R = \left\{ \frac{1}{\frac{\ln\left(\frac{l}{l_0}\right)}{\ln\left(\frac{w_0}{w}\right)}} - 1 \right\} \quad (2.2)$$

This equation can be deduced from the assumption that the volume of material remains constant. This assumption only holds true when the elastic strains are negligible in comparison to the plastic strains. In order to obtain a mean R-value for a sheet material with normal anisotropy, the R-value is measured in the rolling direction, the transverse direction, and at 45 degrees to the rolling direction, and averaged using Equation 2.3.

$$\bar{R} = \frac{R_0 + 2R_{45} + R_{90}}{4} \quad (2.3)$$

2.2 ANISOTROPIC YIELD FUNCTIONS

The yield point of a material is theoretically defined by its elastic limit. Yield offsets can also be defined based upon other characteristics, including set values of plastic work or strain. A 0.2% offset is typically used in engineering applications, especially when an elastic limit cannot be clearly defined.

Von Mises' yield function provides an accurate prediction for stress states at which yielding will occur for many ductile materials. However, von Mises' yield criterion is only applicable for isotropic materials, and is unable to accurately predict yielding for anisotropic materials. Multiple yield functions have been proposed to define the plastic anisotropy of sheet metals.

2.2.1 Hill's 1948 criterion

In 1948, Hill proposed one of the first anisotropic yield functions [7], as an extension of von Mises' yield criterion. Hill's 1948 criterion makes use of the yield stresses in different orientations of a sheet metal to determine the yield locus, as indicated by Equation 2.4.

$$\bar{\sigma}_{eff} = F(\sigma_y - \sigma_z)^2 + G(\sigma_z - \sigma_x)^2 + H(\sigma_x - \sigma_y)^2 + 2L\sigma_{yz}^2 + 2M\sigma_{zx}^2 + 2N\sigma_{xy}^2 = 1 \quad (2.4)$$

Where $\bar{\sigma}_{eff}$ represents the effective stress, typically chosen as the uniaxial flow stress in the rolling direction. For thin sheet metals, out-of-plane stress components can generally be neglected.

$$\sigma_z = \sigma_{zx} = \sigma_{zy} = 0 \quad (2.5)$$

and the anisotropic parameters in equation 2.4 are determined using Equations 2.6 - 2.9.

$$2F = \frac{1}{(\sigma_y^Y)^2} - \frac{1}{(\sigma_x^Y)^2} + \frac{1}{(\sigma_B^Y)^2} \quad (2.6)$$

$$2G = \frac{1}{(\sigma_x^Y)^2} - \frac{1}{(\sigma_y^Y)^2} + \frac{1}{(\sigma_B^Y)^2} \quad (2.7)$$

$$2H = \frac{1}{(\sigma_x^Y)^2} + \frac{1}{(\sigma_y^Y)^2} - \frac{1}{(\sigma_B^Y)^2} \quad (2.8)$$

$$2N = \frac{4}{(\sigma_x^Y)^2} - \frac{1}{(\sigma_B^Y)^2} \quad (2.9)$$

where σ_x^Y , σ_y^Y and σ_B^Y are the yield stress in the rolling direction, the transverse direction and in equibiaxial tension, respectively.

Hill's 1948 yield criterion can also be written in terms of R-values, as shown in equation 2.10.

$$R_0 \sigma_y^2 + R_{90} \sigma_x^2 + R_0 R_{90} (\sigma_x - \sigma_y)^2 + (2R_{45} + 1)(R_0 + R_{90}) \sigma_{xy}^2 = (R_{90} + R_0 R_{90}) \bar{\sigma}_{eff}^2 \quad (2.10)$$

While no direct relationship exists between Hill's 1948 R-based and stress-based yield functions, similar yield loci are typically obtained regardless of which expression is used.

Due to the simplicity of Hill's 1948 criterion, it is often used to model the behaviour of low-carbon sheet steels.

2.2.2 Hill's 1979 criterion

It has been shown that Hill's 1948 criterion fails to provide an accurate analysis for materials with R-values less than 1 [8]. In order to overcome this limitation, Hill's 1979 yield criterion was proposed [9, 10] which incorporates a material characteristic (m) as shown in Equation 2.11. The m value causes distortion of the yield ellipse along the equibiaxial direction. When the value of m is less than 2, the yield surface is elongated, as shown in Figure 2.2.

$$\bar{\sigma}_{eff} = f(\sigma_y - \sigma_z)^m + g(\sigma_z - \sigma_x)^m + h(\sigma_x - \sigma_y)^m = 1 \quad (2.11)$$

When m is equal to 2, Hill's 1979 criterion reduces to Hill's 1948 criterion. Coefficients F , G , and H in Hill's 1948 yield criterion are equal to the values of $f/\bar{\sigma}_{eff}^2$, $g/\bar{\sigma}_{eff}^2$, and $h/\bar{\sigma}_{eff}^2$, respectively.

In the case of in-plane isotropy (normal anisotropy), for plane-stress deformation, Hill's 1979 yield criterion can be written as shown in Equation 2.12.

$$\bar{\sigma}_{eff} = \left\{ \frac{1}{2(1+\bar{R})} \left[(1+2\bar{R})(\sigma_1 - \sigma_2)^m + (\sigma_1 + \sigma_2)^m \right] \right\}^{\frac{1}{m}} \quad (2.12)$$

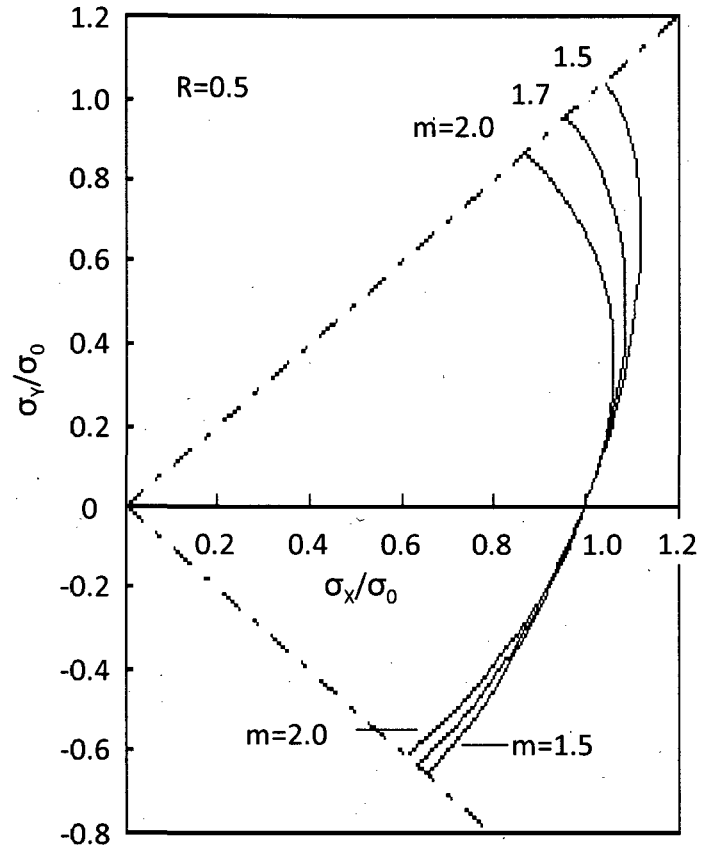


Figure 2.2 Effect of coefficient m in Hill's 1979 yield function on the shape of the yield locus [9]

2.2.3 YLD2000-2d

In 2003, Barlat et al. [11, 12] proposed another plane-stress anisotropic yield function. This yield function uses linear transformations of the Cauchy stress tensor to define the yield locus of a material.

$$2\bar{\sigma}_{eff}^a = |X'_1 - X'_2|^a + |2X''_2 + X''_1|^a + |2X''_1 + X''_2|^a \quad (2.13)$$

where X'_i and X''_i are principal values of the stress deviation tensors, as defined by equations 2.14 and 2.15 and a is a material-dependant parameter – typically $a = 6$ for body-centred-cubic (bcc) materials and $a = 8$ for face-centred-cubic (fcc) materials.

$$X'_1 = \frac{1}{2} \left(X'_{xx} + X'_{yy} + \sqrt{(X'_{xx} - X'_{yy})^2 + 4X'^2_{xy}} \right) \quad (2.14a)$$

$$X'_2 = \frac{1}{2} \left(X'_{xx} + X'_{yy} - \sqrt{(X'_{xx} - X'_{yy})^2 + 4X'^2_{xy}} \right) \quad (2.14b)$$

$$X''_1 = \frac{1}{2} \left(X''_{xx} + X''_{yy} + \sqrt{(X''_{xx} - X''_{yy})^2 + 4X''^2_{xy}} \right) \quad (2.15a)$$

$$X''_2 = \frac{1}{2} \left(X''_{xx} + X''_{yy} - \sqrt{(X''_{xx} - X''_{yy})^2 + 4X''^2_{xy}} \right) \quad (2.15b)$$

X'_{ij} and X''_{ij} are defined by:

$$\begin{bmatrix} X'_{xx} \\ X'_{yy} \\ X'_{xy} \end{bmatrix} = \begin{bmatrix} C'_{11} & C'_{12} & 0 \\ C'_{21} & C'_{22} & 0 \\ 0 & 0 & C'_{66} \end{bmatrix} \begin{bmatrix} S_{xx} \\ S_{yy} \\ S_{xy} \end{bmatrix}$$

(2.16)

$$\begin{bmatrix} X''_{xx} \\ X''_{yy} \\ X''_{xy} \end{bmatrix} = \begin{bmatrix} C''_{11} & C''_{12} & 0 \\ C''_{21} & C''_{22} & 0 \\ 0 & 0 & C''_{66} \end{bmatrix} \begin{bmatrix} S_{xx} \\ S_{yy} \\ S_{xy} \end{bmatrix}$$

where C'_{ij} and C''_{ij} represent the anisotropy coefficients. In order to obtain these coefficients, a system of equations is developed based on the yield stresses and R-values from uniaxial tension tests at 0°, 45° and 90° to the rolling direction, and the equibiaxial stress state. Barlat's yld2000-2d is often defined by anisotropy coefficients α_1 - α_8 , which are related to the C'_{ij} and C''_{ij} coefficients through equation 2.17.

$$\begin{aligned} \alpha_1 &= C'_{11} \\ \alpha_2 &= C'_{22} \\ \alpha_3 &= 2C''_{21} + C''_{11} \\ 2\alpha_4 &= 2C''_{22} + C''_{12} \\ 2\alpha_5 &= 2C''_{11} + C''_{21} \\ \alpha_6 &= 2C''_{12} + C''_{22} \\ \alpha_7 &= C'_{66} \\ \alpha_8 &= C''_{66} \end{aligned} \quad (2.17)$$

When all 8 alpha coefficients are equal to 1, Barlat's yld2000-2d reduces to an isotropic yield function.

While this function was developed for aluminum alloys, it can be applied to describe the anisotropic behaviour of sheet steels under plane-stress conditions. YLD2000-2d provides an accurate yield locus, matching experimental results, and is considered a valid yield function for linear strain paths.

2.3 EXPERIMENTAL DETERMINATION OF THE YIELD LOCUS

In order to obtain the experimental yield locus, several yield stresses were determined in principal stress space. These stress states, represented in Figure 2.3, provide a basis upon which the yield locus can be estimated. Once the yield stress is determined in uniaxial tension (1), plane-strain tension (2), uniaxial compression (3), equibiaxial tension (4), and pure-shear (5) points, a curve is fitted through these points. Due to the nature of anisotropic materials, these points must be measured in both the rolling and transverse directions, for both tension and compression (note: the equibiaxial point involves testing in both the rolling and transverse direction). Materials are assumed to be orthotropic, with the anisotropic characteristics being symmetric about the rolling and transverse axes.

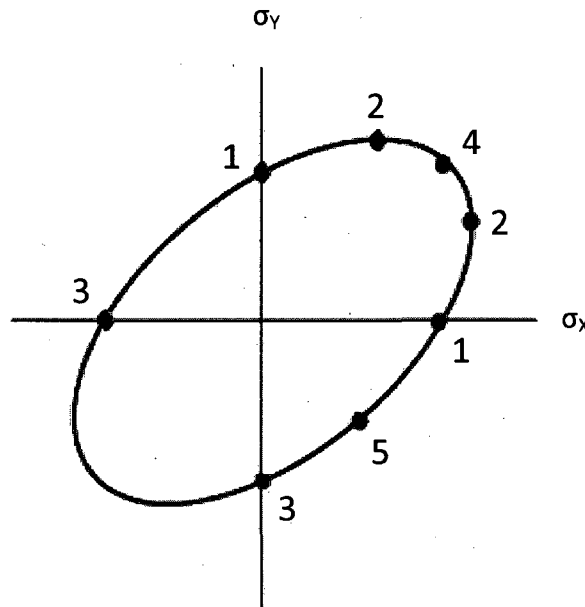


Figure 2.3 Yield locus representing key points for measurement (1 – uniaxial tension, 2 – plane-strain tension, 3 – uniaxial compression, 4 – equibiaxial tension, 5 – pure shear)

2.3.1 Plane-strain tension

Plane-strain conditions exist in specimens that are very wide, and where the strain across the width is zero. Plane-strain tension tests generate the maximum positive values of the yield stress for the rolling and transverse directions.

When a force is applied to a wide plane-strain specimen, stresses occur in the direction of the applied force as well as in the direction perpendicular to the applied force. Figure 2.4 shows the strain vs. position graph for a plane-strain specimen, with a well-defined section of plane-strain ($\epsilon_y/\epsilon_x > 5$) [13] from approximately 7 - 72 mm along the width.

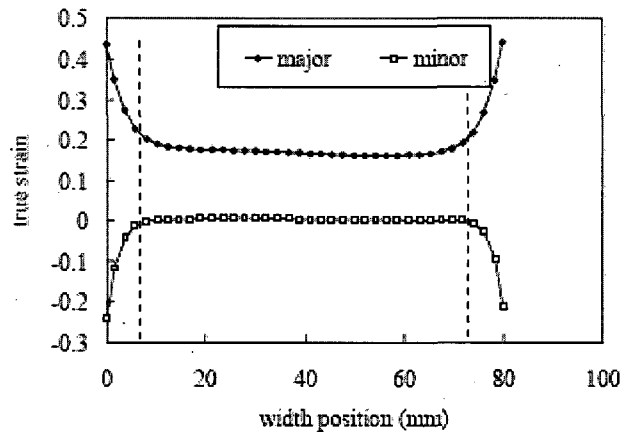


Figure 2.4 Strain distribution of major and minor strain in plane-strain test (LC-steel, W=81mm) [14]

As no ASTM standard exists for plane-strain tension tests, specimens used in plane-strain testing contain only basic similarities. Work was performed by Wagoner [5, 13, 15] to create a specimen with a large plane-strain region. This specimen, Wagoner's 'H' design, is shown in Figure 2.5, as well as Wagoner's 'B' design. Tests by Vegter et al. [14] concluded that plane-strain conditions were not dependant on specimen width, once plane-strain conditions were obtained.

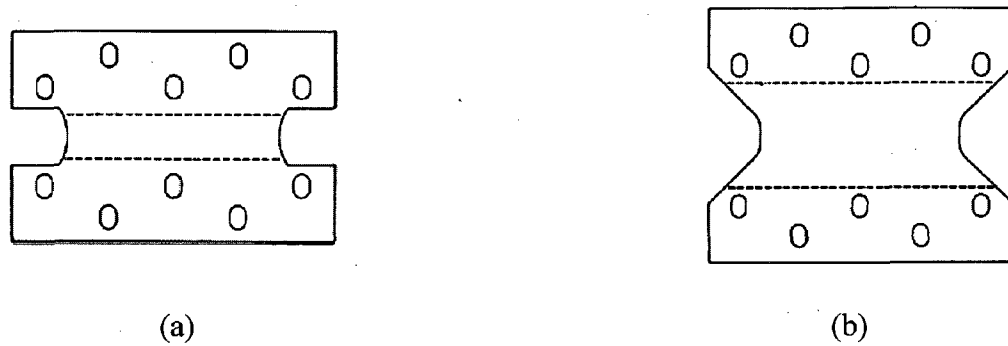


Figure 2.5 a) Wagoner's 'H' design for plane-strain specimen b) Wagoner's 'B' design for plane-strain specimen [5]

In order to obtain approximations of the stresses in a plane-strain specimen, Wagoner used uniaxial tension results to obtain an estimate of the load supported in the edge region, defined by the region where $|\epsilon_y / \epsilon_x| < 5$. These loads were then removed from the total load applied to the specimen in order to obtain an estimate of the load applied to the plane-strain region. The effective stress was obtained using Hill's 1948 yield criterion, and the effective strain was obtained by averaging the strains measured over the plane-strain region.

2.3.2 Equibiaxial tension

Equibiaxial tension occurs when equal tensile loads are applied to a specimen along perpendicular axes. This provides the stress state where the stress in the rolling direction is equal to the stress in the transverse direction. While there are methods for obtaining this point on the yield locus, they often require the use of expensive equipment.

One method, the hydrostatic bulge test, involves clamping a circular blank and applying water pressure to one side of the specimen [16]. The hydrostatic pressure causes the specimen to bulge out in such a way that the stresses in the specimen are equal in all directions expanding radially from the specimen center.

Another popular method for determining the equibiaxial tensile yield stress involves the use of cruciform specimens. Multiple designs of cruciform specimens exist [17-25], one of which is shown in Figure 2.6. By applying equal forces to all arms of the cruciform, the central section of the specimen undergoes equibiaxial tension.

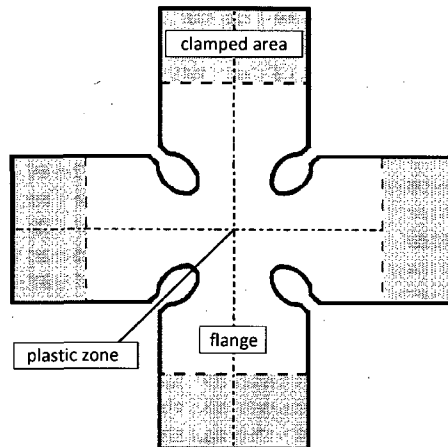


Figure 2.6 Cruciform specimen [24]

The hydrostatic bulge testing provides stress and strain data up to large strains, however as the onset of bulging can occur suddenly, it is often difficult to obtain accurate results at low strains. By changing the specimen shape from a circular blank to an elliptical blank, the bulge test can also be used to obtain other biaxial stress ratios on the yield locus, however as indicated earlier, the hydrostatic bulge test requires testing equipment that is not always readily available.

The cruciform specimen can also be used to obtain multiple points on the yield locus – by modifying the ratio of the applied forces, every stress state in the positive quadrant of the yield locus can be obtained – however the equipment required to perform testing on a cruciform specimen is, as with the hydrostatic bulge, not often available. Furthermore, the stress concentrations in the corners of the specimen limit the useful range of stress and strain data to levels of effective strain below 0.2.

Various methods exist for calculating the R-value during an equibiaxial tension test [26]. The first method, as shown in Equation 2.18, relates the transverse (ϵ_T) and longitudinal (ϵ_L) strains.

$$R_{be} = \frac{\epsilon_T}{\epsilon_L} \quad (2.18)$$

According to the associated flow rule of plasticity, the R-value of a material is related to the tangent of the yield locus, as shown in Equation 2.19.

$$\frac{d\sigma_T}{d\sigma_L} = \frac{1+r_0}{r_0}; \sigma_T = 0; \frac{d\sigma_L}{d\sigma_T} = \frac{r_0}{1+r_0}; \sigma_L = 0 \quad (2.19)$$

If this is assumed, the R-value for the equibiaxial tension test can be obtained through Equation 2.20.

$$R_{be} = \frac{R_0}{R_{90}} \quad (2.20)$$

2.3.3 Uniaxial compression

Unlike the uniaxial and plane-strain tension tests, compression testing provides many difficulties for sheet metal specimens. Due to the reduced thickness of sheet metal specimens, elastic buckling can occur very easily. Buckling is a failure mode that occurs in compression, often before the ultimate compressive stress of the material, and occasionally before the yield stress, due to elastic instability of the specimen. As a result, the specimen must be designed so that yielding will occur before buckling.

There are two potential methods to increase the critical buckling force for buckling, as defined by the Euler equation (Equation 2.21). The first method involves reducing the length of the specimen. As shown in Euler's equation, the critical force is inversely proportional to the length squared, and a decrease in specimen length results in an increase in the critical force. The second method involves increasing the thickness of the specimen. As indicated by the second moment of the cross-sectional area (Equation 2.22), an increase in specimen width results in a direct increase of the critical force, while an increase in specimen thickness results in a cubic increase of the critical buckling force.

$$F_{cr} = \frac{\pi^2 EI}{(Kl)^2} \quad (2.21)$$

where

$$I = \frac{bh^3}{12} \quad (2.22)$$

Multiple testing procedures exist for uniaxial compression tests. One method is the use of small, narrow specimens [27]. Other methods exist for obtaining the uniaxial compression yield point, involving other methods of support for the specimen [28-32], examples of which are shown in Figure 2.7. Measurements are obtained by strain gauges located either along the edge of the specimen, or through slots located on the surface of the support fixture. ASTM standard E9 [33] provides specimen geometries for various support fixtures, however no standard exists for a single thickness specimen. One method for obtaining a thicker specimen involves bonding multiple specimens together [34]. Due to the cubic relation, by gluing two specimens together, the force required for buckling increases eight times. While using laminated specimens results in a significant increase in the buckling force, the adhesive involved in laminating the specimens will affect the characteristics of the specimen. This must be accounted for in order to obtain accurate stress data.

Specimen support can produce other difficulties that must be overcome. Use of a support structure introduces the potential for friction between the specimen and the support fixture. This friction will affect the yield point, and must be accounted for in order to obtain accurate results. Another problem involves obtaining in process data. As the support structure is meant to enclose the specimen, it is often difficult to obtain strain measurements until the test is complete. In order to obtain the strains at the yield point, the support structure must be designed to allow for in-process strain measurements. The use of a support system causes frictional and biaxial loads which can be overcome with the use of lubricants [34] or accounted for in the calculation of stresses [35].

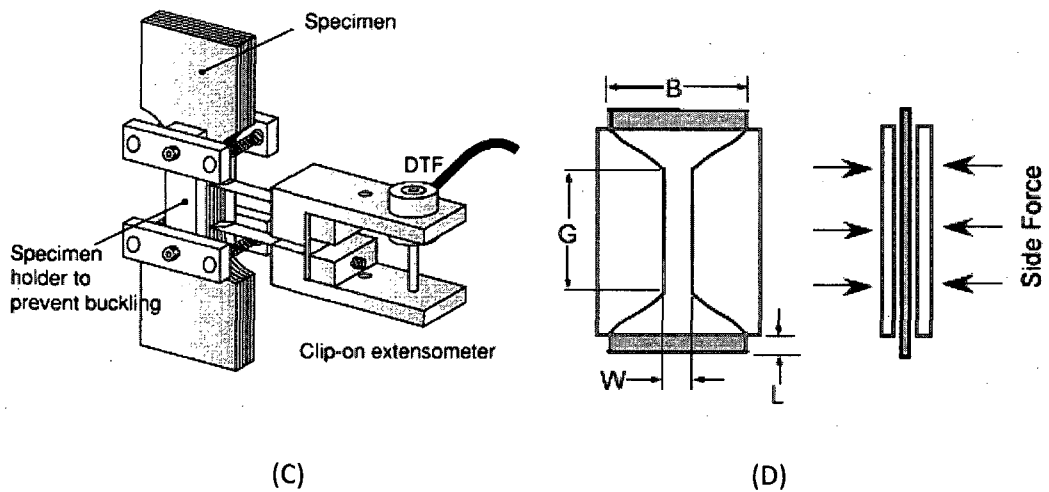
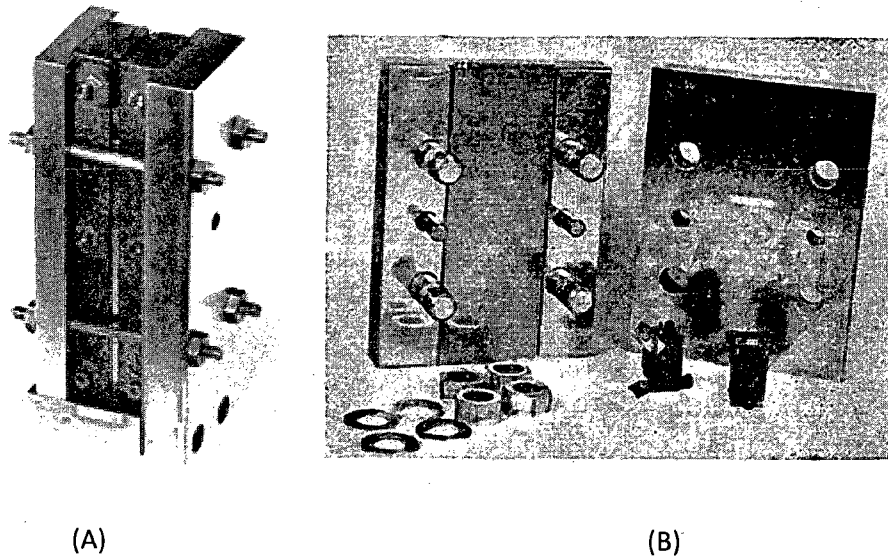


Figure 2.7 Methods for compression testing. A [36] B [37] C [34] D[35]

2.3.4 Pure shear

A final test can be performed to determine a yield point in quadrants II and IV where the stress in the rolling direction is equal to the negative value of the stress in the transverse direction. While the pure shear test is often considered unnecessary due to minimal curvature in quadrants II and IV, cyclic shear tests were performed to measure the Bauschinger effect on a material [38]. Figure 2.8

shows the shear specimen proposed by Miyauchi [39], which causes simple shear in the shaded region through the application of opposing loads as indicated.

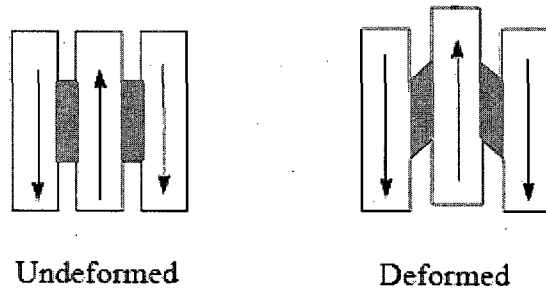


Figure 2.8 Geometry of pure shear specimen [14]

Another method for obtaining shear stresses was presented by Thuillier and Manach [40] and Carbonnière et al. [41] and involves the use of a rectangular specimen, and the testing apparatus shown in Figure 2.9. This procedure involves the use of a single fixed clamp, and a moveable clamp which is used to apply shear loads.

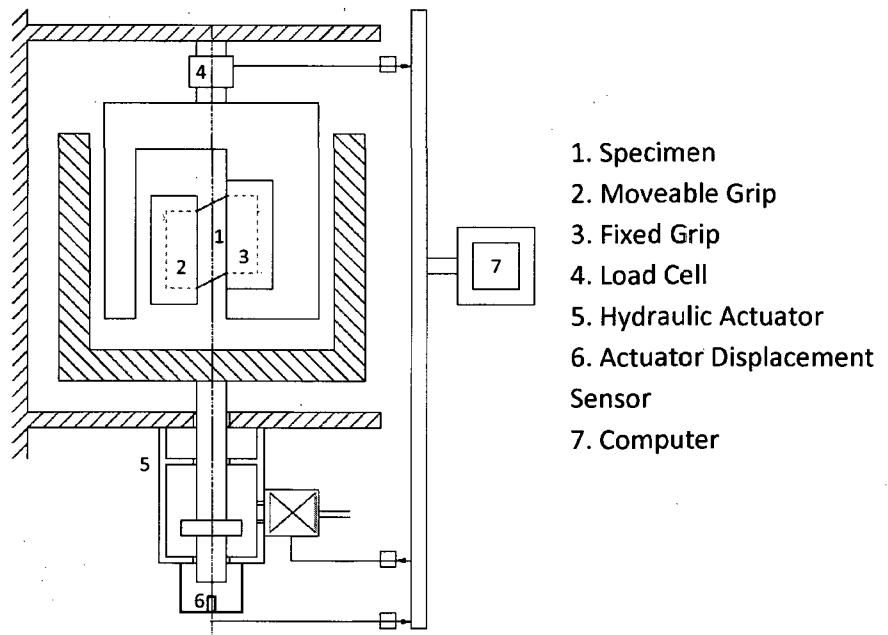


Figure 2.9 Schematic of a simple shear test apparatus developed at the Université de Bretagne-Sud [40]

2.4 DIGITAL IMAGE CORRELATION

The accurate measurement of strain is important to properly define material response. Strain gauges are often used to experimentally measure strains. Strain gauges provide an average one-dimensional strain over the length of the gauge. Unfortunately, in order to obtain an accurate representation of strains across a large surface with varying strains, multiple strain gauges in multiple orientations are required.

Another method for obtaining surface strains on a deformed sheet specimen is the circle grid technique. This process involves the application of a circular grid pattern of a known radius. Once surface deformation has occurred, strains are obtained through the measurement of circle deformation, allowing for multi-directional surface strains to be obtained. This is often a lengthy and tedious process, as the deformation of many circles must be measured in order to obtain a complete surface strain distribution. The accuracy of the circle grid technique is dependent on the size of the grid, and a reduction in grid size causes an increase in the time required to obtain strain measurements.

A faster and more efficient way of measuring multi-directional surface strains is to use DIC measurement techniques. DIC is a process in which displacements and strains are measured from digital images. DIC works through the tracking of a pattern on the surface of a specimen. The use of images in calculating strains is not new; Wagoner [5, 13, 15] used a circle-grid pattern on his plane-strain specimens, and took a series of images throughout the test. Strain values were then calculated at each image through measurement of the deformation of the individual circles. Rao [42, 43] applied a grid pattern to tensile specimens, and strains were obtained through the deformation of the grid. Development of computer technology and digital camera resolutions allow for increased accuracy of calculated strains on a finer scale.

Macro-image facets are created through the image using a series of pixels (typically 5-20 pixels per side) across the image, allowing for sub-pixel accuracy [44]. The number of facets within an image depends on the resolution of the cameras used, and the defined size and overlay of the facets, however it is possible to get thousands of facets over an image (a 13 x 13 pixel facet with a 2 pixel overlap allows for the formation of over 10,000 facets on an image with a resolution of 1280 x 1024). The centre location of each facet provides surface coordinates, and the locations of these facets are tracked through the series of images. In order to obtain strain values, the centre location of the facet is measured with respect to the surrounding facets.

At each stage, the strain, displacement and rotation values are obtained with respect to a reference stage. Typically, the initial image provides the reference frame from which measurements are taken, and further images are taken either during or after the deformation of a specimen. However strains can also be obtained with respect to a reference stage other than the initial stage.

A single camera DIC system is able to measure in-plane deformation, while a multi-camera system is able to obtain 3-dimensional measurements of strains and displacements. DIC provides a non-contact measurement technique which is able to analyse strain fields over an entire surface, and is not restricted to a single axis, as with most extensometer measurements.

High sensitivity can be obtained using DIC, with a displacement sensitivity on the order of 1/30,000 the field of view [44], and with a strain sensitivity of 50-100 micro-strain.

The accuracy of results obtained using DIC techniques is dependent on many factors [45], including the resolution and configuration of the cameras used, the quality of the light source, the accuracy of calibration, and the quality of the surface pattern. Using DIC equipment, it is possible to measure strains from 0.05% to several 100% [46], depending on the quality of the aforementioned factors.

3. EXPERIMENTAL PROCEDURES

The objective of this study is to experimentally determine the yield locus for HSLA and DP600 sheet steels, with a view to more accurately modelling the behaviour of automotive steel sheets used in complex forming processes. This chapter provides an overview of the procedure used to obtain yield loci. The experimental testing performed in this research included uniaxial tension, plane-strain tension, and uniaxial compression of HSLA and DP600 specimens under quasi-static loading to determine the yield locus of both materials. Both uniaxial tension and uniaxial compression tests were performed in the rolling and transverse direction, as well as at 45 degrees to the rolling direction. Plane-strain tests were performed in the rolling and transverse direction. Strain measurements were obtained using DIC techniques.

Section 3.1 discusses the specimens used in the study, including the specimen geometries and specimen preparation procedure. Section 3.2 discusses the experimental and analysis procedure, including an overview of the testing equipment and the validation of the digital image correlation equipment. Section 3.3 discusses the procedure for obtaining plane-strain results. All tests were performed in the Engineering Mechanics Lab at the University of Windsor. Section 3.4 discusses shear tests and equibiaxial tension tests carried out by third-parties and which were used to obtain yield points.

3.1 TEST SPECIMENS

3.1.1 Material grades

Experimental testing was performed on DP600 and HSLA steels used for the Numisheet 2005 benchmark tests. Materials were cold rolled then hot-dipped in a zinc coating.

DP600 is a dual-phase steel, which consists of ferrite and martensite phases. Dual phase steels exhibit excellent ductility, as well as high work-hardening characteristics. These properties result in increased ultimate tensile strengths of dual-phase steels compared to other steels with similar yield strength.

HSLA is a ferrite steel which is strengthened by the presence of micro-alloying elements including manganese, chromium, and copper. These alloys contribute to fine carbide precipitation and grain-size refinement.

3.1.2 Specimen geometries

Three types of tests were carried out in this research - uniaxial tension, uniaxial compression, and plane-strain tension tests. The geometry of the specimens used for each test is presented below. The DP600 specimens were 1.0mm in thickness, and the HSLA specimens were 0.8mm.

3.1.2.1 Uniaxial tension

The most common method for determining sheet mechanical properties is the uniaxial tension test. This involves applying a tensile load to a 'dog bone' shaped specimen. Due to the constant cross-section, the strain distribution in the gauge area is uniform, allowing for high measurement accuracy. Unlike other testing methods, the geometry of specimens for the uniaxial tension test is controlled by the ASTM E8 standard [47].

Uniaxial tension tests were performed to obtain yield stress, as well as the plastic anisotropy values of the materials, in the rolling and transverse directions. Specimens were taken in the rolling and transverse directions, as well as at 45 degrees to the rolling direction, in accordance to ASTM standard E8M as shown in Figure 3.1. Five specimens were prepared in each direction to ensure acceptable repeatability in the results.

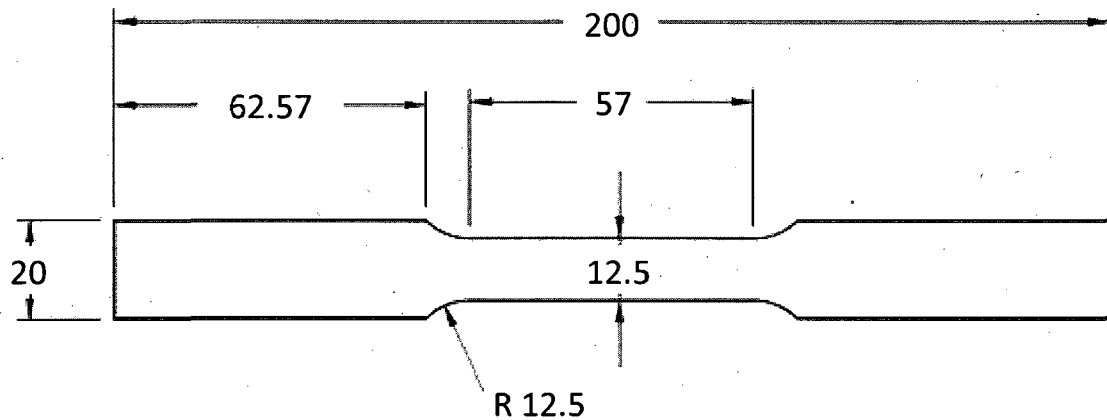


Figure 3.1 Uniaxial tension specimen corresponding to ASTM Standard E8M (dimensions in mm)

3.1.2.2 Uniaxial compression

Uniaxial compression tests were carried out to obtain stress-strain curves and yield stresses for each material. As with uniaxial tension, specimens were prepared in the rolling and transverse directions, as well as at a 45 degree angle to the rolling direction. In order to obtain strain data using DIC, a buckling-prevention support fixture could not be used, since the support fixture would prevent the acquisition of images. Therefore, an unsupported specimen was used. Experimentation showed that buckling occurred at loads far lower than those predicted by the Euler formula due to eccentricity in the loading system. In order to increase the buckling load, the length of the specimen was drastically reduced compared to the uniaxial tension specimen, with a final geometry as shown in Figure 3.2. Tests were also performed with two specimens bonded using Loctite H8600 galvanize bonder in order to increase the cross-section of the specimen. For each material, four compression

tests were performed with a single specimen, and three tests were performed each with two specimens adhesively bonded together.

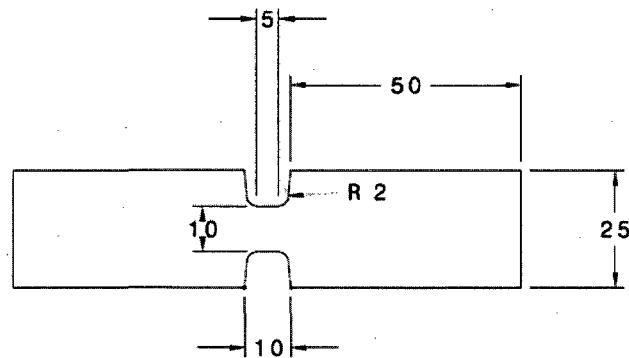


Figure 3.2 Uniaxial compression specimen (dimensions in mm)

3.1.2.3 Plane-strain tension

Plane-strain tension tests were also performed to obtain the plane-strain yield stress values in both the rolling and transverse directions. Unlike uniaxial tests, plane-strain tests were not performed at 45 degrees to the rolling direction. For the plane-strain specimen, a scaled down version of Wagoner's 'B-specimen' was selected (Figure 2.5b). This specimen was chosen over the 'H-specimen' as the presence of a gauge region with uniform strains was necessary in order to take advantage of DIC technology. The dimensions of the 'B-specimen' were reduced by 60%, as shown in Figure 3.3, in order to fit within a calibrated area of $135 \times 108 \text{ mm}^2$ of the DIC system. This calibration panel was selected because it was the largest panel available which could be used with an optical lens with a focal length of 50mm, as indicated by the system provider.

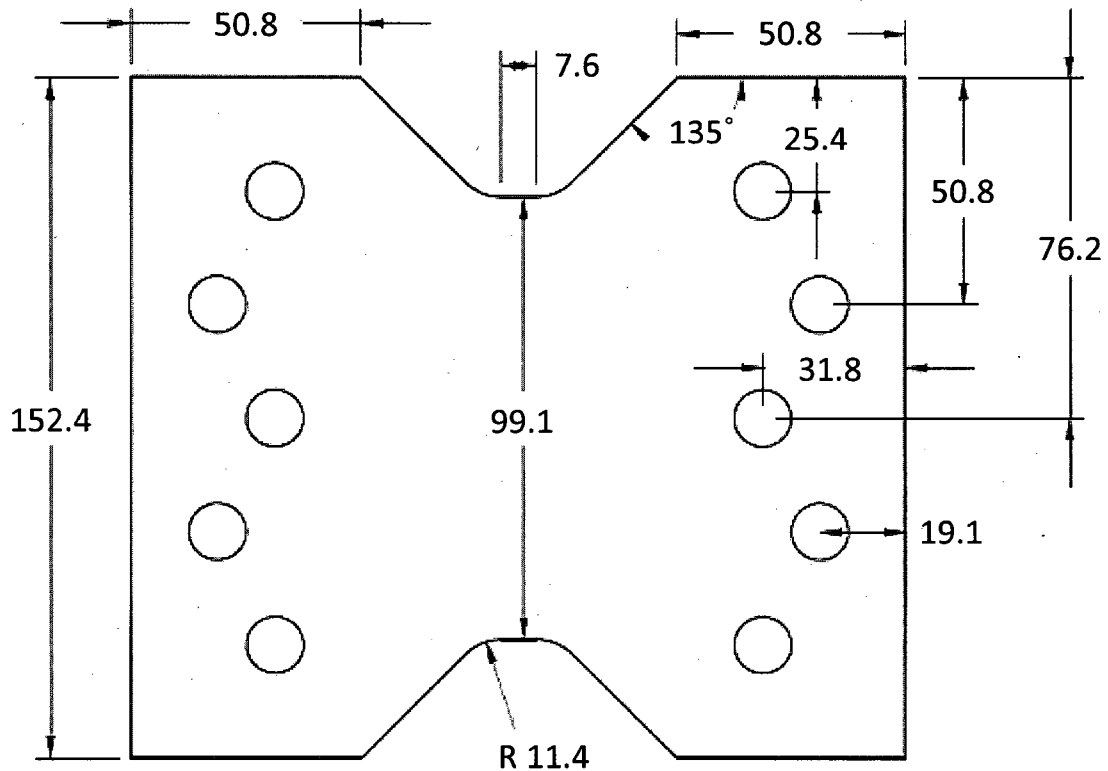


Figure 3.3 Plane-strain specimen (dimensions in mm)

3.1.3 Specimen preparation

All uniaxial and plane-strain test specimens were approximately cut to size using a metal shear, and final specimen geometries were obtained through wire electrical discharge machining (EDM). Use of a wire EDM provides an advantage over other methods, as no residual stresses are incurred on the specimen, whereas other machining methods incur stresses within the specimen that can affect the mechanical response of the specimen.

In order to prepare specimens for use with the ARAMIS DIC system, surfaces were cleaned with a fine synthetic scouring pad and washed in acetone. A flat white paint was applied to the surface in order to reduce glare in the camera image. A black speckle pattern was then applied by using spray

paint in order to obtain a contrast with the white surface coating, and provide surface points from which strain or displacement measurements can be taken using the ARAMIS system. Speckle points were approximately 3 to 5 pixels (less than 0.05mm) in diameter. The same preparation method was performed for all specimens. Figure 3.4 shows a plane-strain specimen prepared for measurement with the ARAMIS system

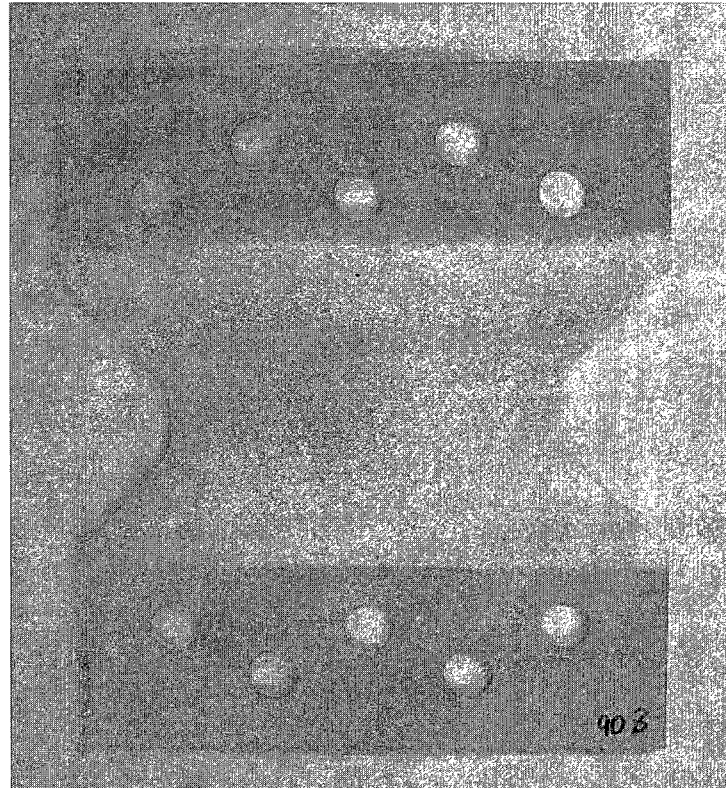


Figure 3.4 Plane-strain specimen prepared for analysis using ARAMIS system

3.2 TESTING PROCEDURES

3.2.1 Testing equipment

All tests were performed on a hydraulic Tinius–Olsen testing machine with a load capacity of 300 kN.

DIC was used to obtain strain profiles of the specimens throughout the testing. The DIC system used for this testing was the ARAMIS system, manufactured by GOM mbH. The ARAMIS system uses two cameras to record images of the specimen during testing. Measurements were obtained from a random pattern, either naturally occurring on the specimen surface, or applied through methods such as spray painting as was done in this work. The distortion of this pattern allows for ARAMIS to calculate strain measurements over the specimen surface at each recorded image. Strains were measured with respect to an initial state, as defined by the first recorded image of the un-deformed specimen. Load values were measured by the Tinius-Olsen load cell and recorded to the ARAMIS data acquisition system using a BNC connector cable.

The clamps typically used to perform tension tests on the Tinius-Olsen machine were not large enough to hold a plane-strain specimen; therefore a new set of clamps was built for plane-strain specimens. Figure 3.5 shows the design of the clamps created for the plane-strain specimen, which were fabricated using 4140 annealed steel. The same clamps were also used for uniaxial compression testing.

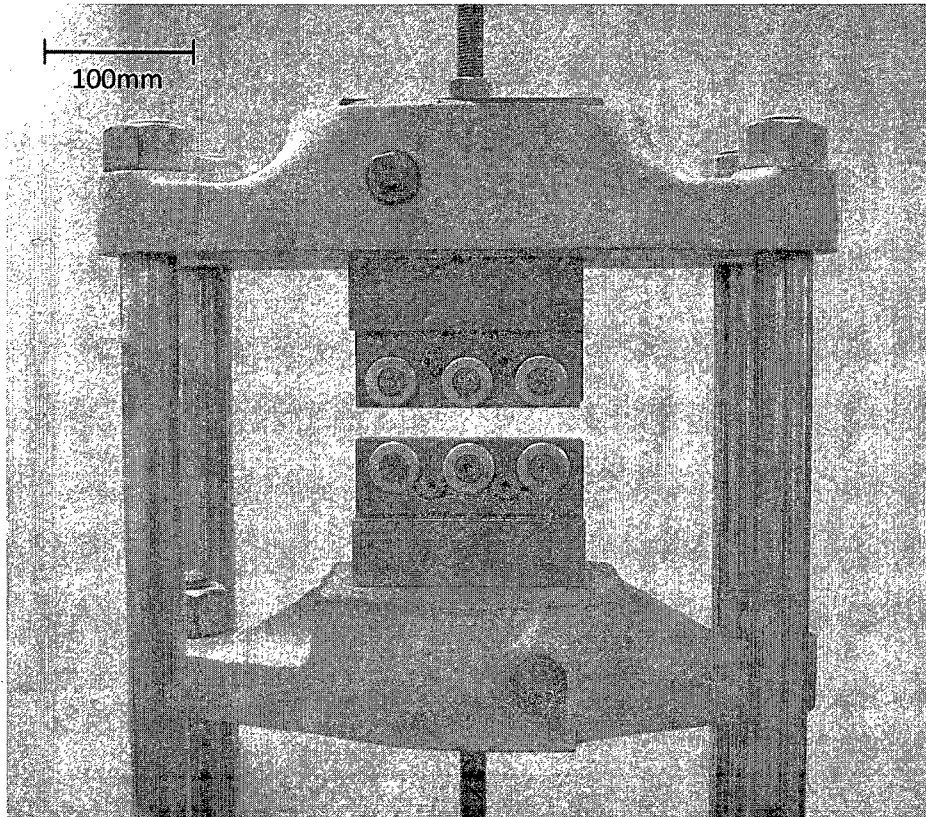


Figure 3.5 Plane-strain tension clamps

3.2.2 System calibration

In order to ensure accurate results were obtained with the ARAMIS system, a calibrated space was prepared within which measurements could be accurately obtained. The calibration volume was set up using calibration panels provided by GOM, with the distance between the cameras, and the distance from the cameras to the calibration volume as specified by the supplier. The calibration procedure was provided by GOM, and involved taking a series of images at the center, and front and back boundaries of the calibrated volume using both cameras, and each camera individually. This process determines the location of the calibrated volume with respect to the cameras, and allows the system to relate the results from each camera. This calibration procedure ensures that the system will compute accurate 3-dimensional surface-strain measurements. Figure 3.6 shows the calibration panel for a 65mm x 52mm x 52mm calibrated volume.

Upon completion of the calibration process, a calibration deviation value is determined by the ARAMIS system, representing the average deviation between each camera through the calibration process. A maximum value of 0.040 pixels was used throughout testing as the limit for acceptable calibration.

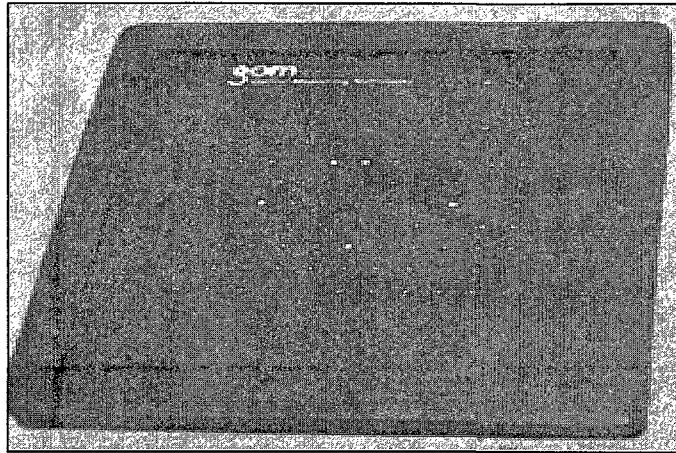


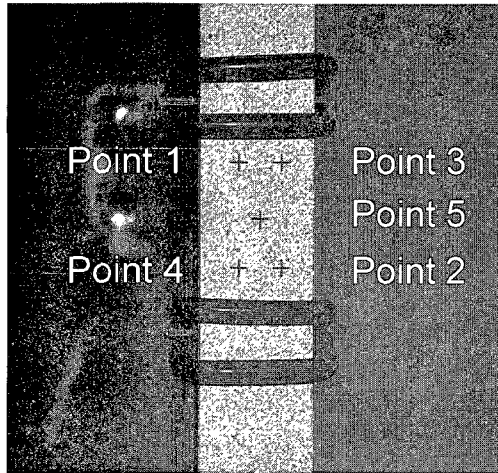
Figure 3.6 Calibration panel

In order to further validate the calibration process, and ensure the quality of the speckle pattern applied to the surface of the specimen, a series of images was taken before testing started. Since no loads were applied, negligible strain values were expected. In the case where strain values greater than 0.05% were obtained, or the ARAMIS system was unable to obtain strains over the entire surface of the specimen, the paint was removed from the specimen, and a new speckle pattern was applied.

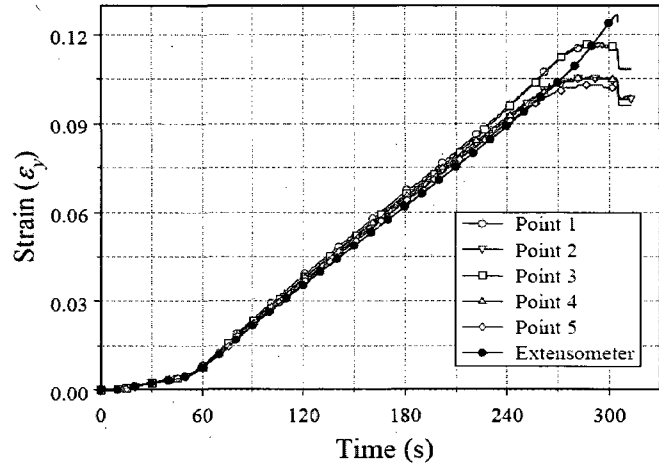
3.2.3 Strain measurement accuracy

The use of DIC allows for the measurement of surface strains with a large degree of accuracy. Displacements can be measured with an accuracy of approximately $1\mu\text{m}$ [48], and strains can be calculated with an accuracy of up to 0.02% [46].

In order to validate results obtained using the ARAMIS system, tension tests were performed following ASTM standard E8M on AA6061-T6 specimens using an INSTRON 8562 tensile testing machine with load capacity of 100kN [49]. The tensile specimens were prepared according to the process described previously for use with the ARAMIS system, and an extensometer with a 25.4 mm gauge length was attached. Extensometer readings were recorded at a rate of 40 Hz and images were obtained using the ARAMIS system at a rate of 0.5 Hz. Strain values were located at five points on the tensile specimen, and compared to values obtained through the extensometer as shown in Figure 3.7. Deviation can be observed at the end of the test, however this is as a result of localized necking, and the location of the measured points with respect to the neck. Before necking occurs (at approximately 280 seconds), deviations no greater than 7% were observed between the measurement techniques.



(A)



(B)

Figure 3.7 (A) Location of ARAMIS strain measurements on specimen (B) Stress-strain profiles from ARAMIS and extensometer [49]

3.2.4 Testing procedure

Tension tests were performed on a hydraulic Tinius-Olsen testing machine. Uniaxial tension specimens were clamped using clamps supplied with the Tinius-Olsen. Both uniaxial compression and plane-strain tension specimens were secured using clamps designed for this testing, as discussed in section 3.2.1.

Uniaxial compression and plane-strain specimens were held in place using 12.7 mm shoulder bolts of #3a grade torqued to 80 N·m. For plane-strain tension, both clamps were secured to the Tinius-Olsen using a 19.05 mm grade C1010 threaded rod with a tensile strength of 345 to 415 MPa. For uniaxial compression tests, the weight of the lower clamp (6.40 kg) was sufficient to ensure the clamp remained in place during testing. In order to ensure no movement occurred, magnets were also used to secure the bottom clamp to the lower plate of the Tinius-Olsen.

Specimens were carefully mounted in the clamps in such a way that the specimen centre-line was parallel to the loading direction. In order to prevent settling of the hydraulic Tinius-Olsen testing machine, the application of load occurred immediately after the fastening of the second clamp. A delay between securing the specimen and the application of the load allows for the potential of a decrease in hydraulic pressure within the Tinius-Olsen, causing the application of an undesired load. In order to account for any strains that may occur after the second clamp was secured, an image was taken using the digital image correlation software with only one clamp secured. This image was used as the reference stage from which strains were measured. As such, all loads were accounted for.

All specimens were tested using the same procedure. Tests were performed at strain rates from $0.001\text{-}0.0018\text{ s}^{-1}$. It is important to note that steel is a strain-rate sensitive material, and experimental results can only be considered valid within this strain range. ARAMIS images were obtained at a frequency of 2.0 Hz. Figure 3.8 shows the experimental set-up for the uniaxial tension tests, including the cameras used for the ARAMIS system. Figure 3.9 and Figure 3.10 show the experimental set-up for plane-strain tension and uniaxial compression tests, respectively.

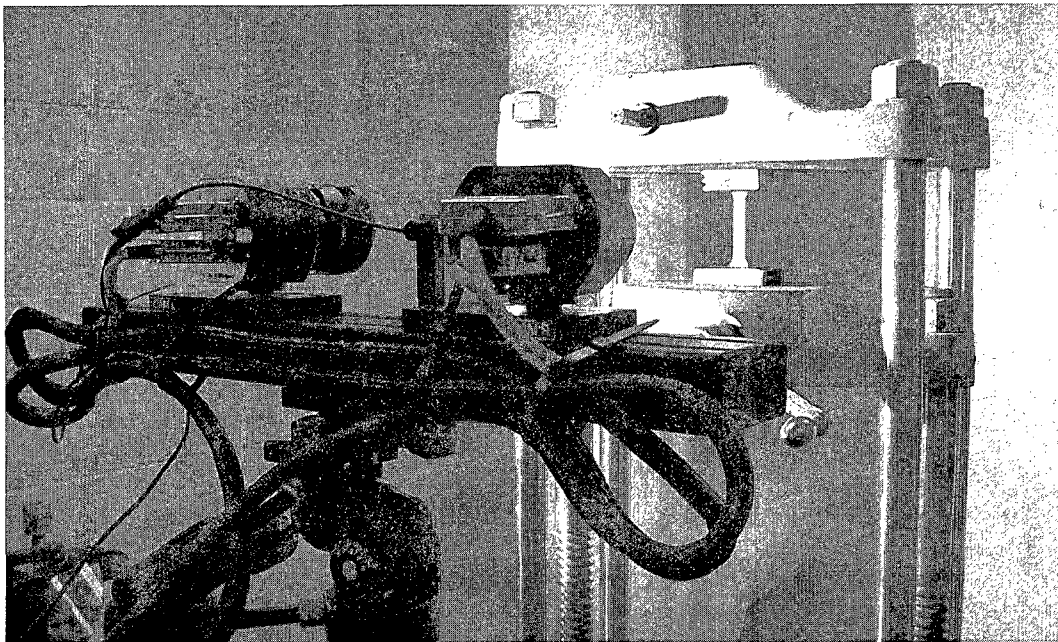


Figure 3.8 Experimental set-up for uniaxial tension test with ARAMIS cameras

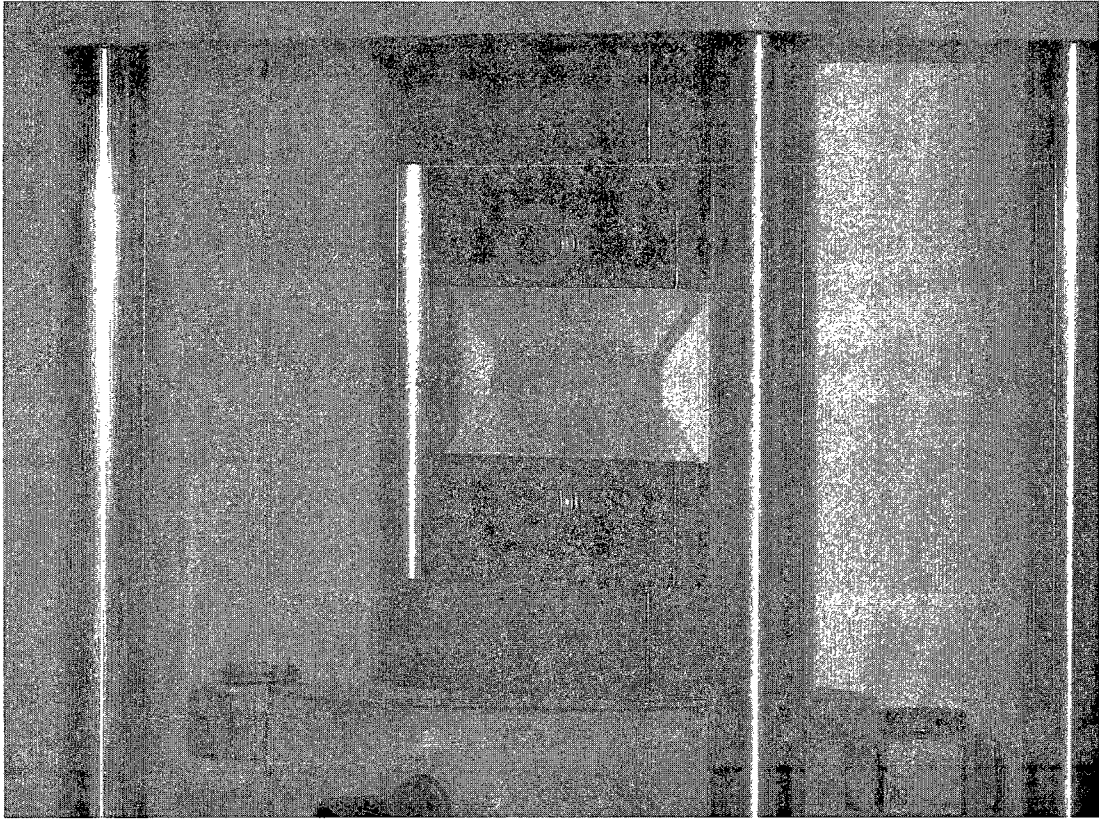


Figure 3.9 Experimental set-up for plane-strain tension tests

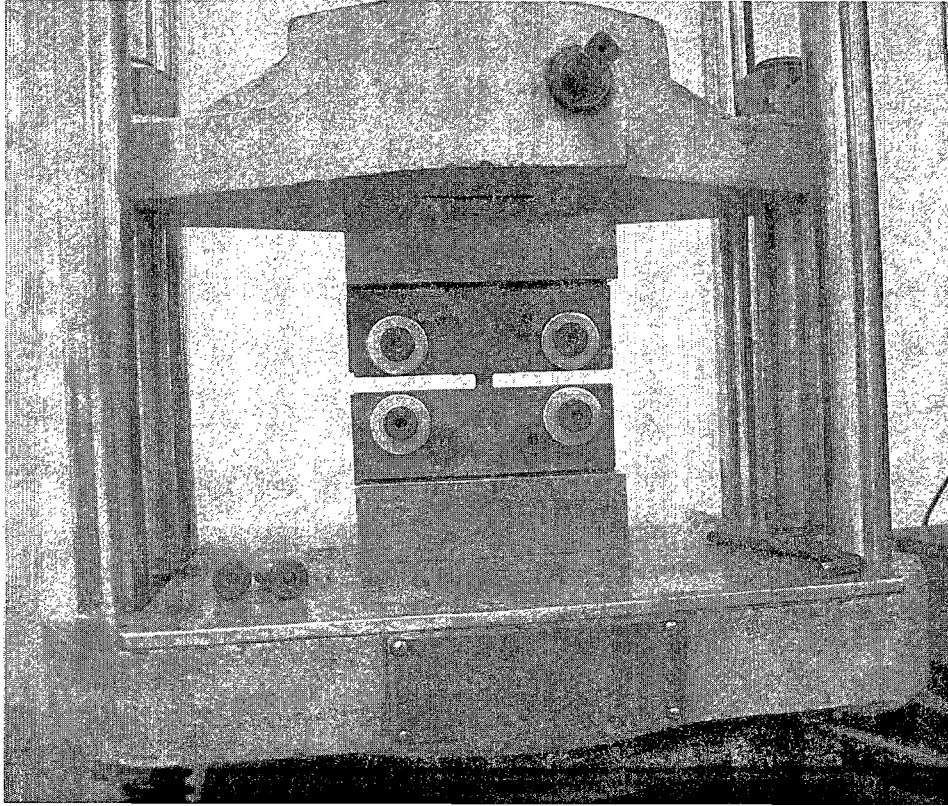


Figure 3.10 Experimental set-up for uniaxial compression tests

3.2.5 Numerical analysis of plane-strain tension tests

Due to an edge effect in plane-strain specimens, the normal axial stress distribution across the gauge area is not uniform. Furthermore, the analysis of the plane-strain specimen must account for the presence of a stress component in the direction transverse to the applied load. In order to obtain an approximation of these principal stresses, an explicit finite element model of the plane-strain specimen was created. Simulations of the plane-strain test were carried out for both materials, in both the rolling and transverse directions. The plane-strain specimen was modeled using 5625 Belytschko-Tsay shell elements, with an element size of $1.32 \times 1.22 \text{ mm}^2$ across the gauge region and a maximum aspect ratio of 2.35. A minimum interior angle of 45 degrees occurred on elements along the edge of the transition region, with elements within the gauge region consisting solely of 90 degree angles. Four-node shell elements were used with five through-thickness integration points. Hill's 3-R material model (equation 2.10) was used to model material

behaviour, with hardening behaviour defined by the uniaxial true stress-true plastic strain curve for the corresponding direction.

The clamps were not included in the numerical model. Tooling was assumed to be rigid, and a prescribed displacement was applied directly to the plane-strain specimen. Nodes lying on the bottom edge of the specimen were completely constrained in both translation and rotation. Rotational constraints were also applied about all three axes to the nodes lying on the upper edge of the specimen. These nodes were also constrained against translation in the width and through-thickness directions, with a displacement of 15mm applied in the axial direction.

The numerical model was run using explicit integration, and a simulation time of 0.010 seconds was used. Numerical models were quasi-static in nature, as evidenced by an internal-to-kinetic energy ratio on the order of 10^5 .

All simulations performed in this research were prepared using LS-PREPOST version 2.2 and run on LS-DYNA version 970 revision 5434a. A personal computer with an AMD Opteron Processor 248 with 4 GB of RAM was used to carry out the simulations of the plane-strain tension tests. The simulation time for each model was approximately 30 minutes.

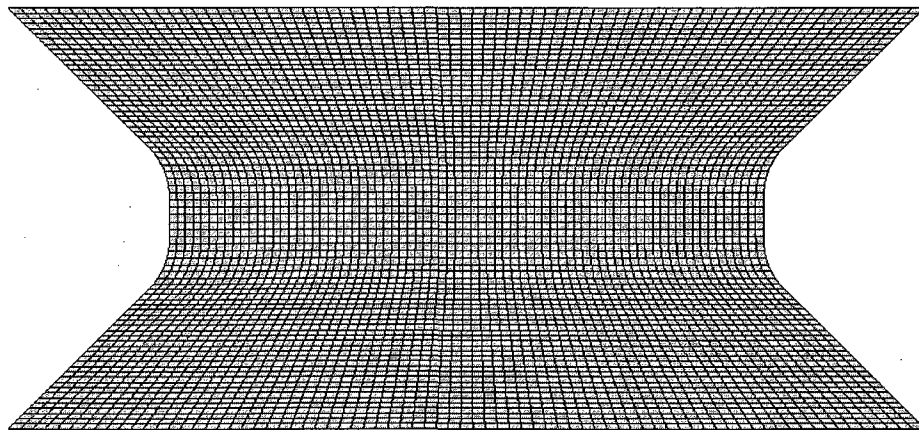


Figure 3.11 Numerical model of plane strain specimen

In order to verify mesh sensitivity, the simulation was performed using specimens with 1369 and 3600 shell elements (with element sizes of $2.68 \times 2.47 \text{ mm}^2$ and $1.65 \times 1.53 \text{ mm}^2$, respectively, across the gauge region. Similar aspect ratios were maintained for all element sizes), and the resulting load-displacement curves were compared for the element at the intersection of both symmetry lines.

3.3 OUTSOURCED TESTS

In order to obtain further information on the mechanical properties of the materials tested, several tests were outsourced. These tests included bulge tests, cyclic shear testing and cyclic compression-tension, which provided additional experimental yield data.

Hydraulic bulge tests (as discussed in section 2.3.2) were performed at the Alcoa Technical Center in order to obtain the equibiaxial tension true stress-true strain response of the materials. Cyclic shear testing was performed at the Université de Bretagne-Sud in France following the procedure indicated in section 2.3.5, with the testing apparatus shown in Figure 2.8. Results from the first cycle were used to obtain the yield values in simple shear. Cyclic tension-compression tests were performed at Ohio State University, following the procedure indicated in section 2.3.4, with the specimen shown in Figure 2.7 D. As with the cyclic shear test, results from the first cycle in a compression-tension-compression cycle were used to obtain the yield stress in uniaxial compression.

3.4 ANALYSIS OF DATA

The purpose of carrying out a range of different tests on these two sheet materials was to experimentally determine the onset of yield when material is loaded along different proportional stress paths. This section will present the methodology for determining the stresses at yield for each of the tests described in the previous section.

For the uniaxial tension specimens, engineering stress-strain curves were experimentally obtained, and converted into true stress-true strain. A one inch gauge length was used to obtain strain data, and the average strain across the full width was used to calculate the R-value for each orientation.

In order to estimate the stress-strain response of the plane-strain specimens, experimental load-strain data was compared with numerically predicted results at the centre of the specimen. A representative theoretical model was chosen based upon its accuracy with respect to the experimental results, as done by Green et al. for cruciform testing [17]. A curve of best fit was applied to the experimentally obtained load-strain response (Curve fit equations and R^2 values are presented in Appendix B). The predicted loads were scaled down point by point in such a way as to make the predicted load-strain curve coincide with the experimental load-strain curve. Assuming a linear relationship between load and stress, the same scaling factor was then applied point by point to the predicted stress-strain curve in order to obtain an estimation of the stress-strain response of the experimental specimen.

This technique of scaling down the predicted stress-strain curves by the same amount as is required to make the predicted load-strain curves coincide with the experimental load-strain curves is obviously not a rigorous one. However, it provides a reasonable estimate of the actual stress-strain behaviour in plane-strain, and consequently should provide a reasonable approximation of the experimental yield stress in plane-strain. It was found that the scaling factor ranged from 0.91 to 1.02 for all plane-strain tests.

In order to validate these results, Wagoner's procedure (as described in section 2.3.2) for predicting the stress-strain response in plane-strain specimens was performed, and compared to the results predicted with LS-DYNA. Wagoner's procedure was performed using principal strain values obtained along a section through the centre-line of the specimen.

In order to obtain the anisotropic coefficients for Barlat's Yld2000-2d, the R-values for equibiaxial tension were calculated using equation 2.16.

Consistency in yield point selection was obtained through measurements of the plastic work done on a specimen during testing. Yield points were selected for uniaxial tension specimens based upon flow stresses at levels of plastic work corresponding to the average plastic work per unit volume (obtained from the area under the true stress-true plastic strain response) for various offset values in uniaxial tension in the rolling and transverse directions. The corresponding plastic work per unit volume values were calculated at these points, and plane-strain tension, equibiaxial tension, pure shear and uniaxial compression yield data were obtained for the same values of plastic work per unit volume. This was repeated for all test data, and average yield stresses and standard deviations were obtained. Once yield stresses and R-values were determined for all tested specimens, all four yield functions (Hill's 1948 criterion using yield stresses and R-values, Hill's 1979 and Barlat's Yld2000 criteria) were obtained and compared to experimental data in order to determine which yield function more adequately represented the behaviour of these two sheet materials.

4. RESULTS AND DISCUSSION

This chapter discusses the experimental results obtained in this research. Section 4.1 discusses the uniaxial tension tests, including yield values, Young's modulus, and R-values. Both experimental and numerical simulation results for plane-strain tension tests are shown in Section 4.2. Section 4.3 presents the uniaxial compression tests performed for this research. Yield values obtained in the outsourced tests are shown in Section 4.4, with stress-strain profiles shown in Appendix B. Finally, section 4.5 shows the yield loci obtained.

4.1 UNIAXIAL TENSION RESULTS

4.1.1 DP600

DP600 exhibits typical ductile yielding behaviour, as shown in Figure 4.1. Representative stress-strain curves for DP600 specimens are shown for specimens oriented at 0, 45, and 90 degrees to the rolling direction. While similar stress-strain curves were obtained for 45 and 90 degree specimens, it can be observed that the specimens taken at 0 degrees to the rolling direction have a stress-strain curve that is slightly lower than for the other two orientations. The engineering stress-strain response of the uniaxial tension specimens was obtained using a 25.4 mm gauge length. The true stress-true strain response was then obtained from the engineering stress-strain data, as shown in Figure 4.2, following the well-known relationships given in Equations 4.1 and 4.2

$$\sigma_{True} = \sigma_{Eng} (1 + e) \quad (4.1)$$

$$\varepsilon = \ln(1 + e) \quad (4.2)$$

where e is the engineering strain.

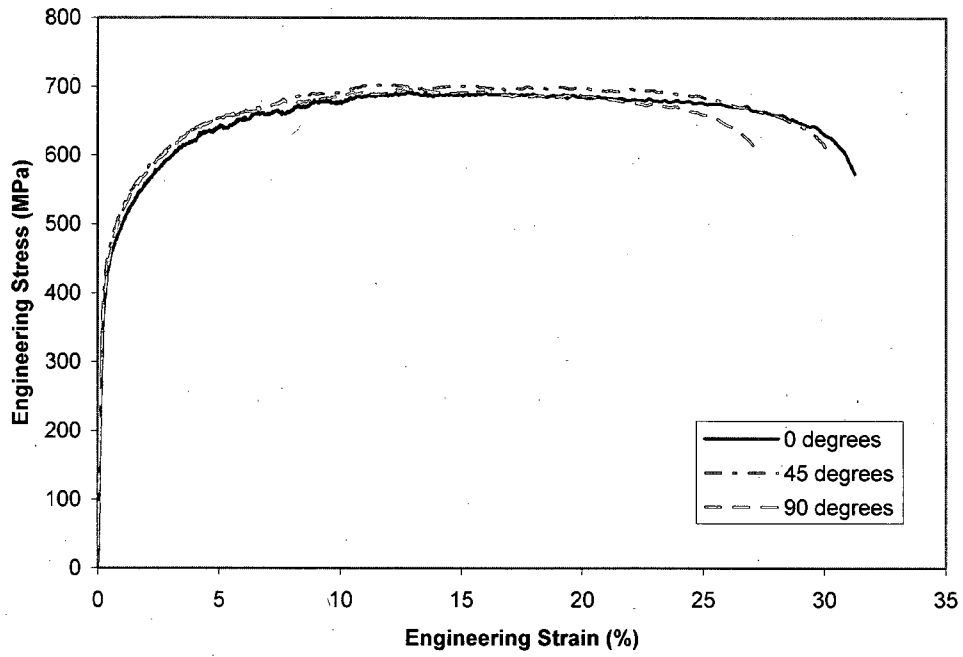


Figure 4.1 Engineering stress-strain behaviour of DP600 in uniaxial tension

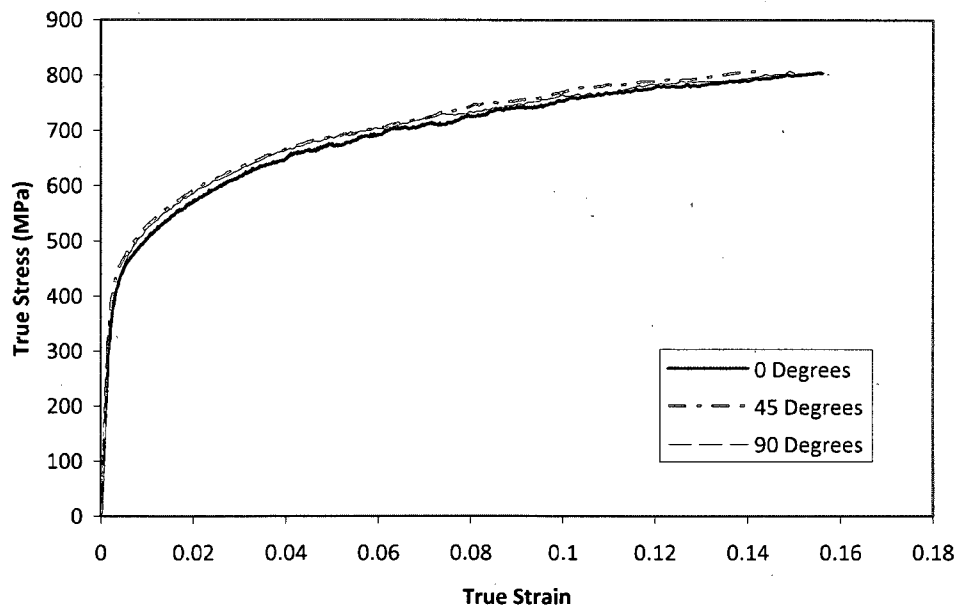


Figure 4.2 True stress-true strain behaviour of DP600 in uniaxial tension

The strain distribution in DP600 uniaxial tension specimens is shown in Figure 4.3 for different levels of strain. As shown in Figure 4.3 A, B and C, a uniform strain distribution developed throughout the specimen. Once the ultimate tensile strength was reached, increased strain values occur in the neck, as shown in Figure 4.3 D. Strain concentrations at the bottom of the specimens occur due to stress concentrations near the transition region.

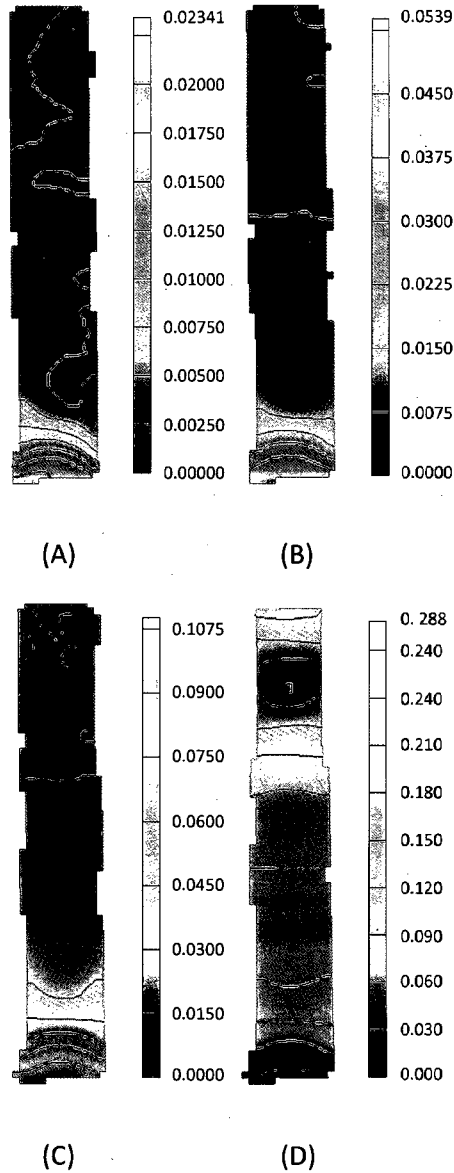


Figure 4.3 Distribution of the true major strains in the gauge area of DP600 uniaxial tension specimens (A) $\epsilon_1=0.0222$ (B) $\epsilon_1=0.0526$ (C) $\epsilon_1=0.103$ (D) $\epsilon_1=0.203$

Flow stress values were obtained for 0.2%, 0.5%, 1.0%, 2.0% and 5.0% offsets from the proportional limit, as shown in Tables 2, 3 and 4. Although the yield stress is rarely defined for plastic offsets greater than 0.2%, the stress values that correspond with increasing values of plastic work per unit volume were recorded with a view to verifying if the yield locus changes its shape as the material work hardens.

Plastic Strain	Yield Stress (MPa)	Standard Deviation (MPa)	Plastic Work Per Unit Volume (MJ/m ³)
0.002	440	5.43	0.82
0.005	486	4.75	2.25
0.01	535	5.84	8.46
0.02	592	5.66	10.5
0.05	681	6.73	29.9

Table 1 Flow stress of DP600 tensile specimens tested in the rolling direction for various values of plastic strain offset and corresponding values of plastic work per unit volume.

Plastic Strain	Yield Stress (MPa)	Standard Deviation (MPa)	Plastic Work Per Unit Volume (MJ/m ³)
0.002	450	6.18	0.873
0.005	496	7.98	2.32
0.01	541	9.12	5.00
0.02	600	9.77	10.8
0.05	690	10.9	30.4

Table 2 Flow stress of DP600 tensile specimens tested at 45 degrees to the rolling direction for various values of plastic strain offset and corresponding values of plastic work per unit volume.

Plastic Strain	Yield Stress (MPa)	Standard Deviation (MPa)	Plastic Work Per Unit Volume (MJ/m ³)
0.002	444	1.31	0.870
0.005	494	4.14	2.30
0.01	541	5.06	4.95
0.02	602	6.00	10.7
0.05	692	9.51	30.4

Table 3 Flow stress of DP600 tensile specimens tested at 90 degrees to the rolling direction for various values of plastic strain offset and corresponding values of plastic work per unit volume.

A region of linear elastic behaviour is clearly visible in Figure 4.1 up to a stress of about 350 MPa. From this region, Young's modulus was determined to be 203 GPa. R-values obtained with ARAMIS strain measurement system for DP600 were 0.875 at 0 degrees, 0.956 at 45 degrees, and 1.112 at 90 degrees to the rolling direction.

4.1.2 HSLA

HSLA steel exhibits yield point elongation, as shown in Figure 4.4, in which 0 degree, 45 degree, and 90 degree representative stress-strain curves are shown. The anisotropy of the tested specimens is evident. True stress-true strain response is shown in Figure 4.5.

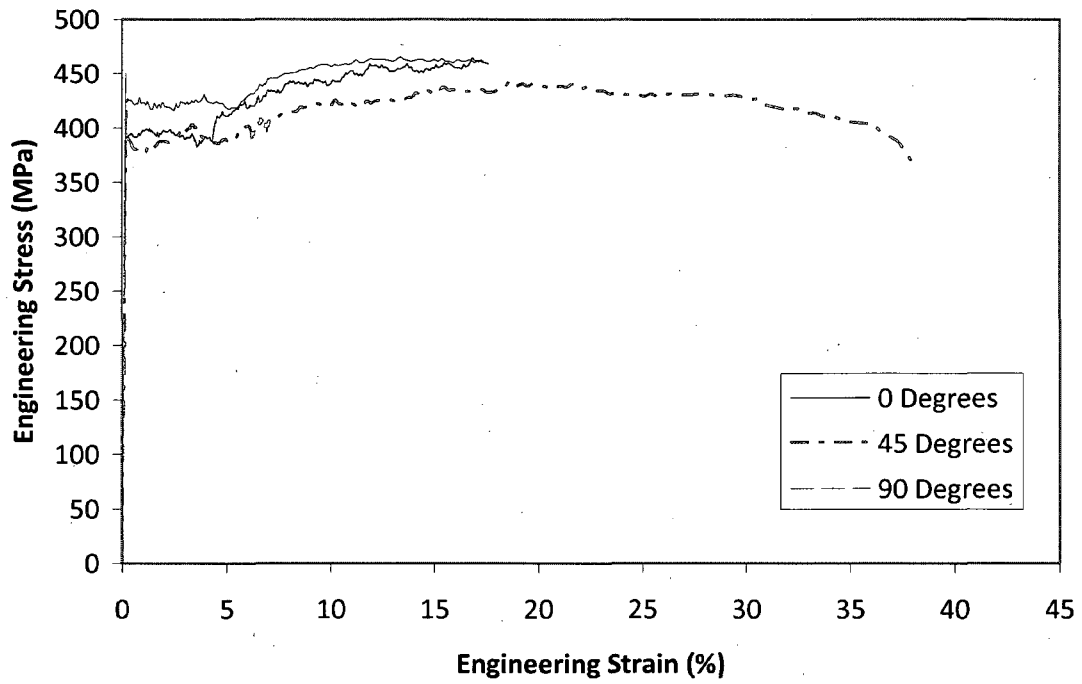


Figure 4.4 Engineering stress-strain behaviour of HSLA in uniaxial tension

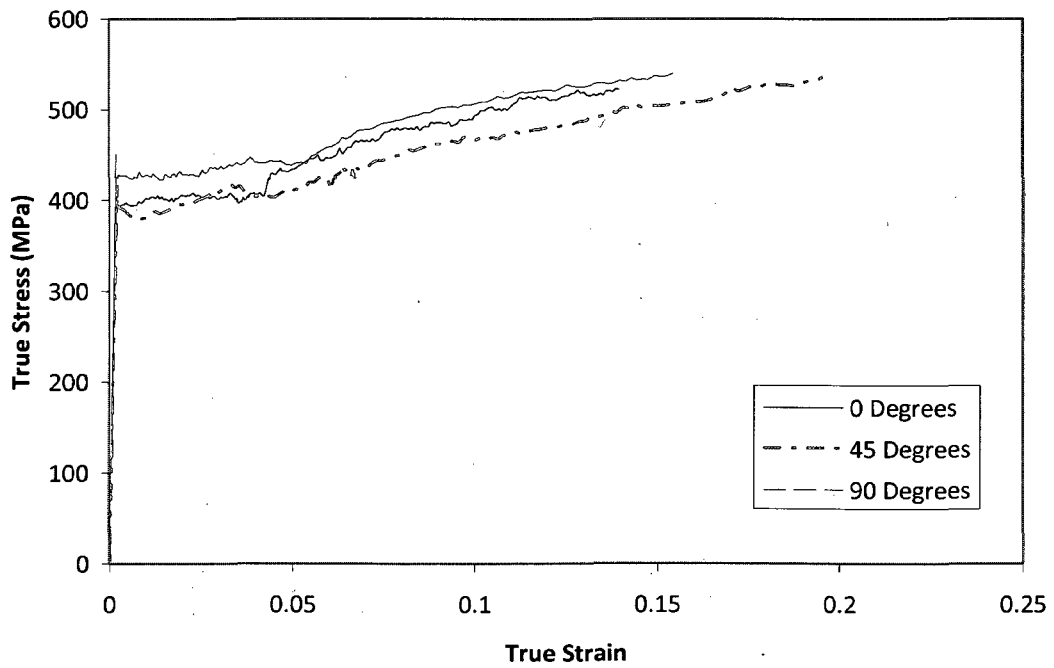


Figure 4.5 True stress-true strain behaviour of HSLA in uniaxial tension

As seen in Figure 4.5, HSLA exhibits yield point elongation from the upper yield value to strain values of 0.042 for the rolling direction to 0.054 at 90 degrees to the rolling direction . This can also be observed by the presence of Lüders bands, as shown in Figure 4.6 A and B. It can be observed that, as the Lüders bands propagate through the specimen, there is little change in the maximum strain value. The Lüders bands occurred at a 35° angle to the horizontal axis. Once the Lüders bands connect, the specimens exhibit typical work hardening behaviour. This can be seen in Figure 4.6 C. Once the ultimate tensile strength is reached, strain concentration occurs as the specimen necks, as shown in Figure 4.6 D.

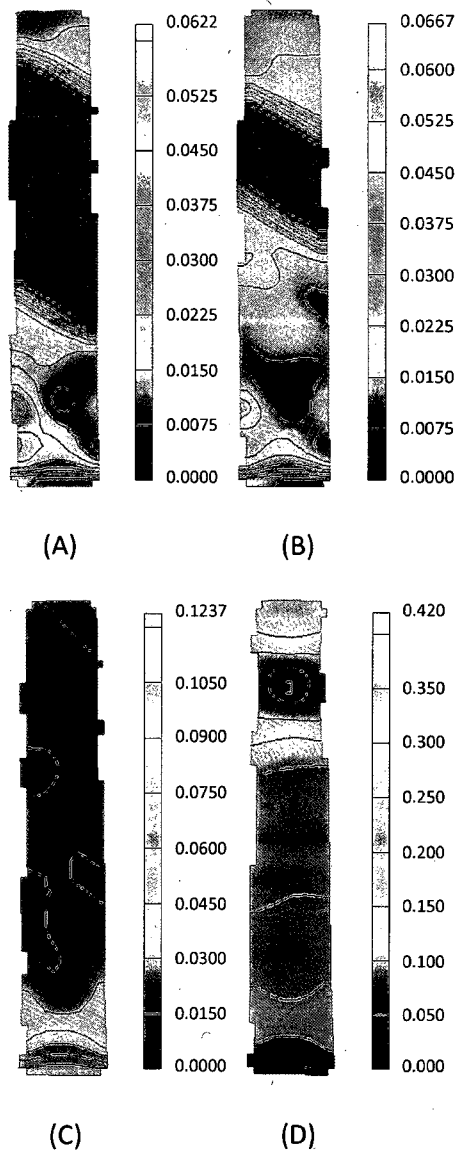


Figure 4.6 Distribution of the true major strains in the gauge area of HSLA uniaxial tension specimens (A) $\epsilon_1=0.00530$ (B) $\epsilon_1=0.0286$ (C) $\epsilon_1=0.119$ (D) $\epsilon_1=0.278$

Stress values at different levels of plastic offset for HSLA are shown in Tables 5, 6 and 7. The similarity in these stresses is due to the yield point elongation.

Plastic Strain	Yield Stress (MPa)	Standard Deviation (MPa)	Plastic Work Per Unit Volume (MJ/m ³)
0.002	394	2.62	0.905
0.01	396	5.41	4.09
0.02	398	4.85	8.09
0.05	432	4.95	20.3
0.10	490	5.23	43.6

Table 4 Flow stress of HSLA tensile specimens tested in the rolling direction for various values of plastic strain offset and corresponding values of plastic work per unit volume.

Plastic Strain	Yield Stress (MPa)	Standard Deviation (MPa)	Plastic Work Per Unit Volume (MJ/m ³)
0.002	387	8.48	0.937
0.01	392	9.41	4.08
0.02	401	3.97	8.04
0.05	407	7.58	20.3
0.10	465	5.59	42.4

Table 5 Flow stress of HSLA tensile specimens tested at 45 degrees to the rolling direction for various values of plastic strain offset and corresponding values of plastic work per unit volume.

Plastic Strain	Yield Stress (MPa)	Standard Deviation (MPa)	Plastic Work Per Unit Volume (MJ/m ³)
0.002	421	8.42	0.931
0.01	422	7.22	4.35
0.02	423	6.78	8.58
0.05	433	7.68	21.5
0.10	499	5.81	45.2

Table 6 Flow stress of HSLA tensile specimens tested at 90 degrees to the rolling direction for various values of plastic strain offset and corresponding values of plastic work per unit volume.

Young's modulus was measured to be 207GPa for the HSLA sheet material. R-values were found to be 0.618 at 0 degrees, 1.547 at 45 degrees and 1.116 at 90 degrees to the rolling direction.

4.2 NUMERICAL PREDICTION OF PLANE-STRAIN TENSION BEHAVIOUR

In order to obtain plane-strain stress-strain data, a numerical model of the plane-strain specimen was created and all plane-strain tension tests were simulated. Stress and strain data were obtained from the centrally located shell element. Predicted load-strain data were compared with experimental data. For each strain value, the ratio of the experimental load values to the numerically predicted load values defined a scaling factor. Assuming a linear relationship between load and stress, this scaling factor was also applied to the stress values in order to obtain a scaled stress-strain curve. It is recognized that this scaling technique is by no means a rigorous way of obtaining the stress-strain behaviour in plane-strain tension. However it is thought to provide a better estimate of the yielding data for relatively small levels of plastic work.

This section discusses the results obtained from numerical modeling, and provides a comparison to experimental results.

4.2.1 DP600

Numerical results for the DP600 plane-strain specimens resulted in a prediction of load values greater than those obtained experimentally. This signifies that experimental stress values are lower than those predicted through numerical modeling. As seen in the yield loci, Hill's 1948 R-based yield function over-predicts the plane-strain values, and this results in an over-prediction of plane-strain values using Hill's 3R material model. Figure 4.7 shows the load-stress response obtained from numerical modeling for DP600 plane-strain specimens. A quasi-linear relationship can be observed to occur in both the rolling and transverse direction until approximately 800MPa.

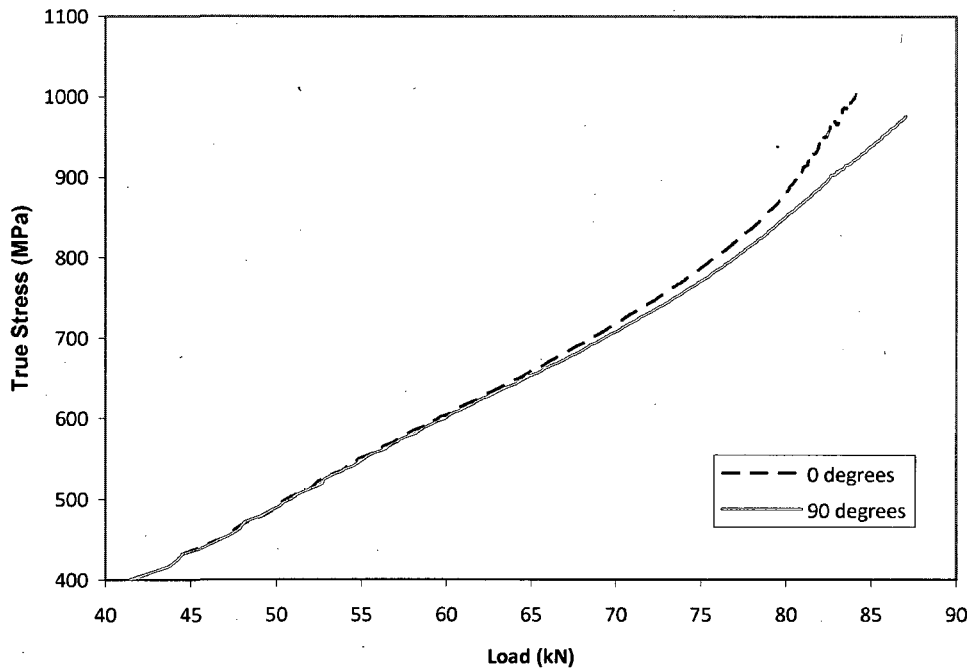


Figure 4.7 Load-Stress behaviour of DP600 specimens in plane-strain tension obtained from numerical analysis

Figure 4.8 provides a comparison of the numerically predicted load versus strain data in plane-strain tension in the rolling direction with that which was obtained after scaling it to correspond with the experimental load versus strain data. The discrepancy between the two curves gives a sense of the

over-prediction of the numerically predicted stress-strain curve. A load decrease can be observed in the scaled numerical results after a true strain of 0.1. It can be shown that this decrease corresponds to the end of the quasi-linear region in the load-true stress response.

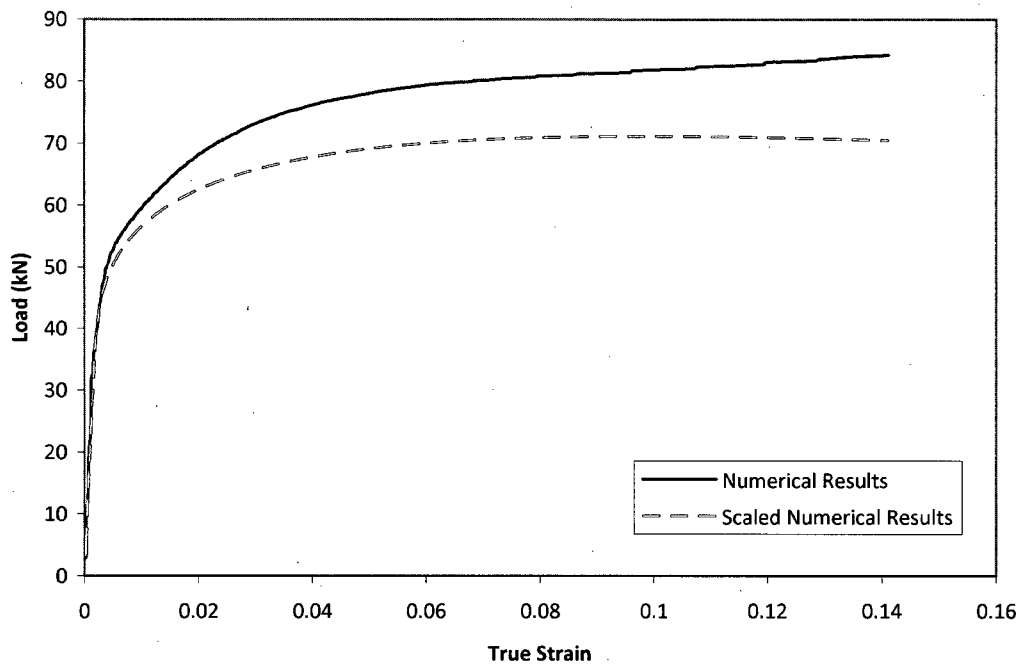


Figure 4.8 Numerical prediction of stress-strain behaviour for DP600 specimen subjected to plane-strain tension in the rolling direction before and after scaling

The stress-strain response of DP600 in plane strain, as estimated by the scaling of results obtained through numerical modelling are shown in Figure 4.9 for specimens tested at 0 degrees and at 90 degrees to the rolling direction. As with the tensile response of DP600, typical ductile yielding behaviour was observed in the plane-strain tension specimens.

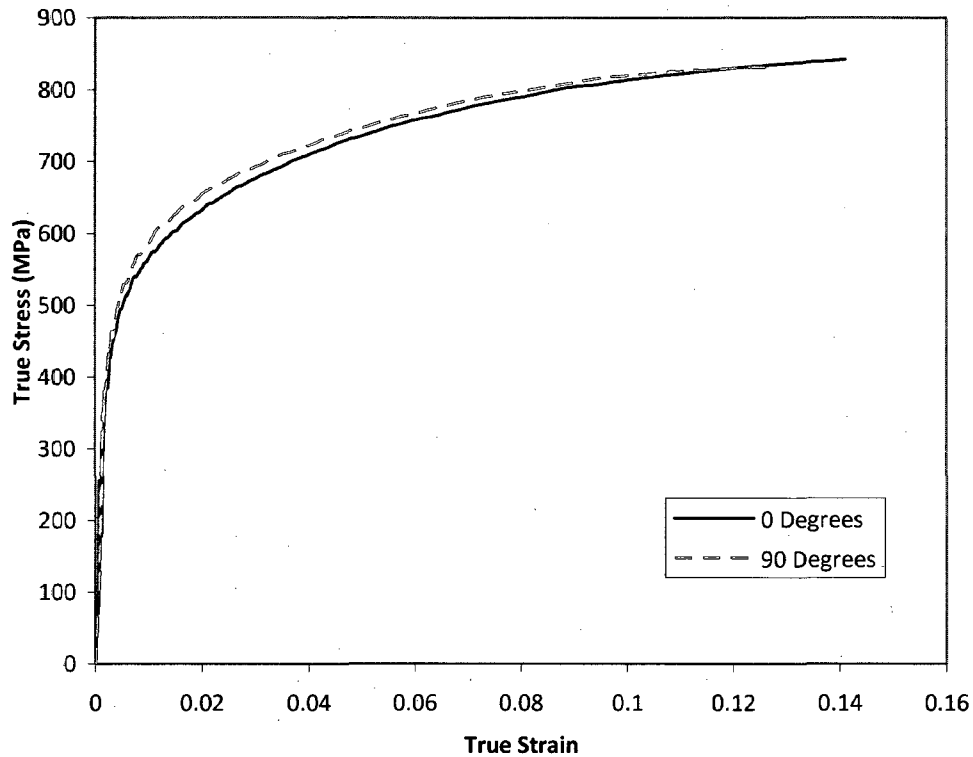


Figure 4.9 Estimated stress-strain behaviour of DP600 in plane-strain tension

A comparison of plane-strain tension results obtained from the scaling of LS-DYNA results (as indicated in section 3.4) and Wagoner's analysis method (as indicated in section 2.3.1, in which plane-strain behaviour is determined through corresponding edge effects to uniaxial tension results in order to obtain an approximation of the load acting over the plane-strain area of the gauge region) are shown in Figure 4.10 and Figure 4.11. While both methods are only approximations of the plane-strain response, the strong correlation between both methods provides a certain level of confidence in the data.

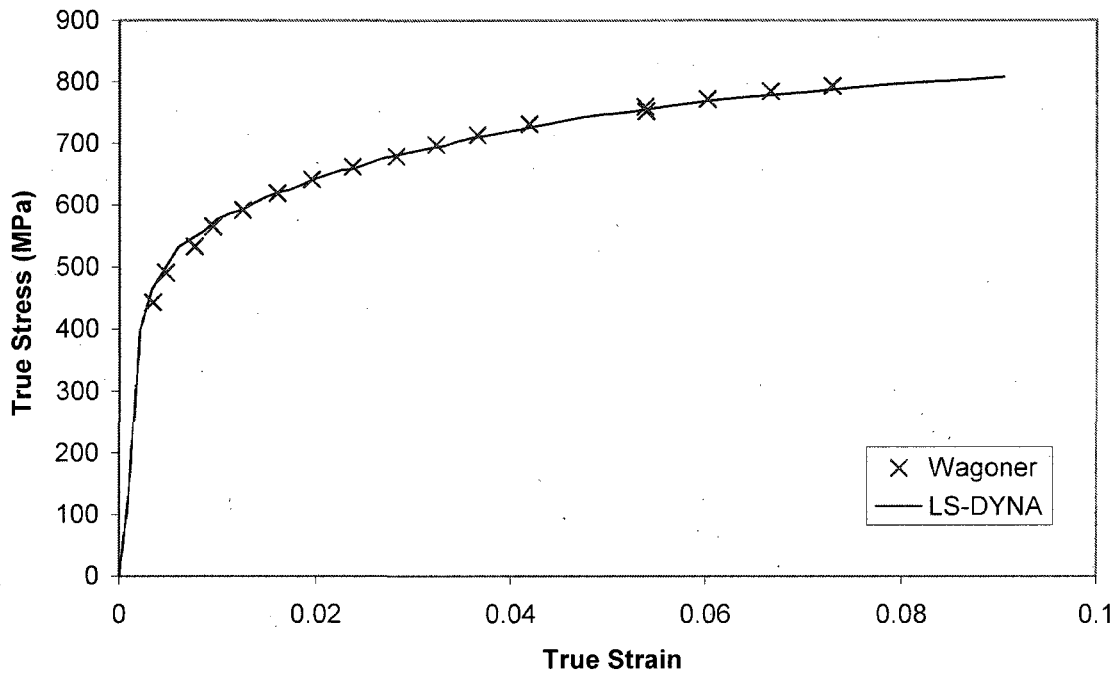


Figure 4.10 Comparison of the plane-strain behaviour of DP600 in the rolling direction as predicted by the Wagoner analysis method and by scaling the curves obtained from finite element simulation

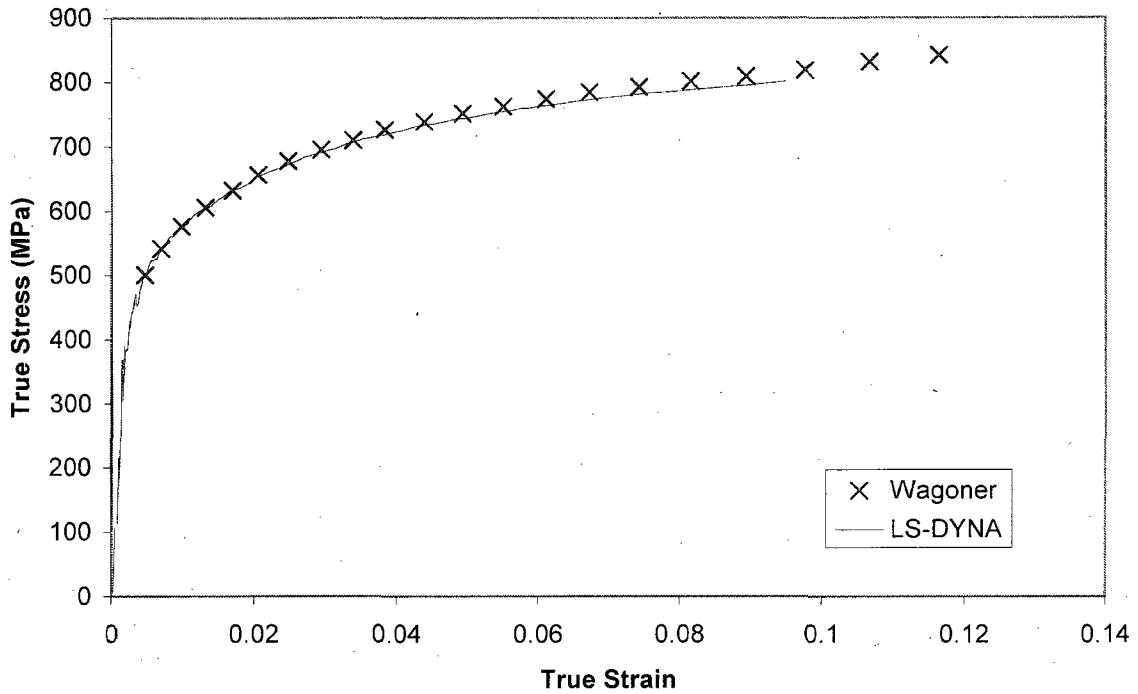


Figure 4.11 Comparison of the plane-strain behaviour of DP600 at 90 degrees to the rolling direction as predicted by the Wagoner analysis method and by scaling the curves obtained from finite element simulation

Figure 4.12 presents the strain distribution predicted by LS-DYNA for a representative plane-strain specimen and corresponds with the experimental strain distribution shown in Figure 4.23 C ($\epsilon_1=0.0391$).

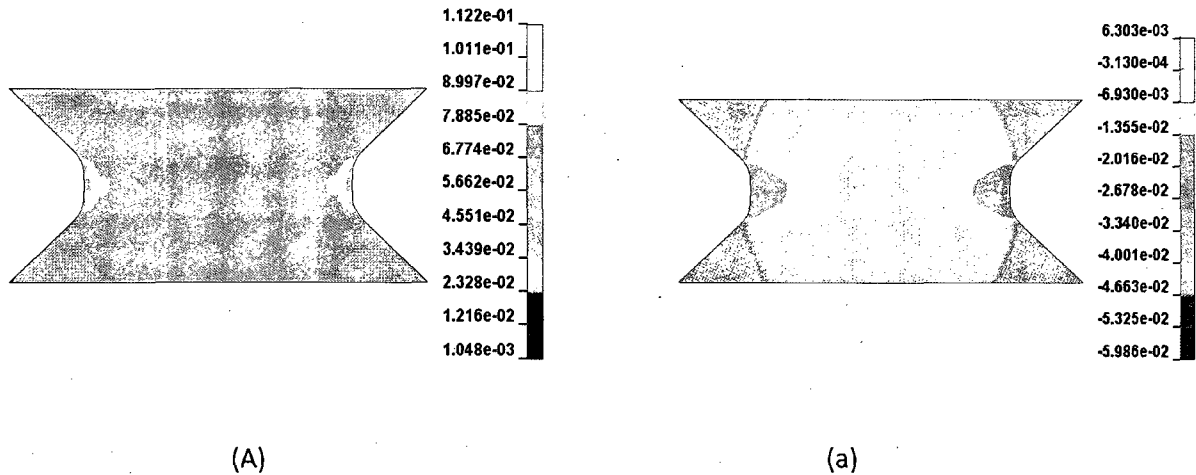


Figure 4.12 (A) Major and (a) minor strain distribution in DP600 plane-strain specimen predicted with LS-DYNA, at $\epsilon_1=0.0391$

Similar strain distributions can be observed between numerical and experimental results for both the major and minor strains. A maximum major strain of 0.1122 is predicted by the numerical model, which corresponds well with the maximum major strain of 0.1117 obtained experimentally. A minor strain of -0.0599 was obtained by numerical modeling, which is slightly larger than the maximum minor strain of -0.0461 obtained experimentally. The edge of the plane-strain specimen acts as a strain-concentrator, with maximum major strain values (and minimum minor strain values) occurring at the corners of the plane-strain region. A comparison of strain values throughout the specimen show a strong correlation between both numerical and experimental results. A slight decrease in strain occurs at the edge of the center-line cross-section for the predicted major strain that is not present in experimental results, however this discrepancy does not extend into the central part of the gauge area, and does not affect the results obtained.

Figure 4.13 shows the principal strains along the width of the gauge region of the plane-strain specimen as predicted by numerical modeling. While a slight decrease in strains is noticeable at the specimen edges, a clear region of plane-strain is visible.

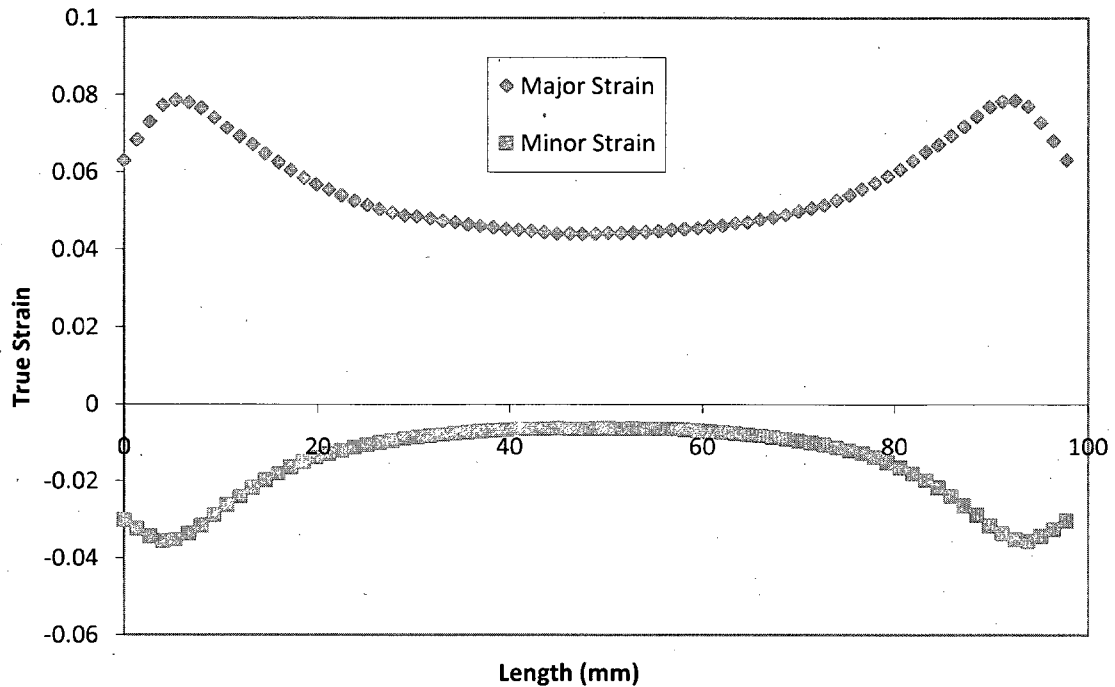


Figure 4.13 Distribution of major and minor true strains computed across the width of the gauge for numerical model of plane-strain DP600 specimen loaded in the rolling direction.

4.2.2 HSLA

As with DP600, numerical load predictions in plane-strain specimens were greater than those obtained experimentally. The load-stress response obtained for the HSLA plane-strain specimens is presented in Figure 4.14. It can be observed that the numerical model for the HSLA specimen does not present a linear relationship between load and stress. While this invalidates the assumption involved in the scaling factor, it can be observed that the degree of curvature in the load-stress curve is minimal, and as such, results obtained from the scaling method can be taken as an acceptable approximation of the plane-strain stress-strain behaviour. Some noise can be seen in the numerical data for the 90 degree specimen.

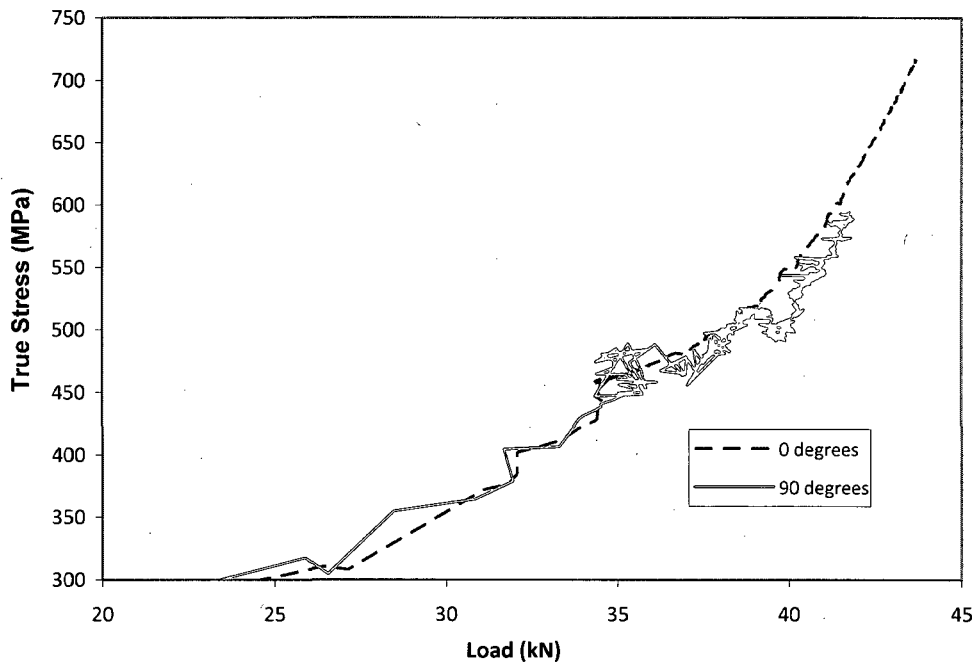


Figure 4.14 Load-stress behaviour of HSLA specimens in plane-strain tension obtained from numerical analysis

A comparison of the load versus strain data for the numerical results and scaled numerical results is shown in Figure 4.15 for the plane-strain tension in the rolling direction. As with the DP600 specimen, it can be seen that the numerical calculation over-predicts the load-true strain behaviour, and a sense of the over-prediction of the true stress-true strain response can be observed.

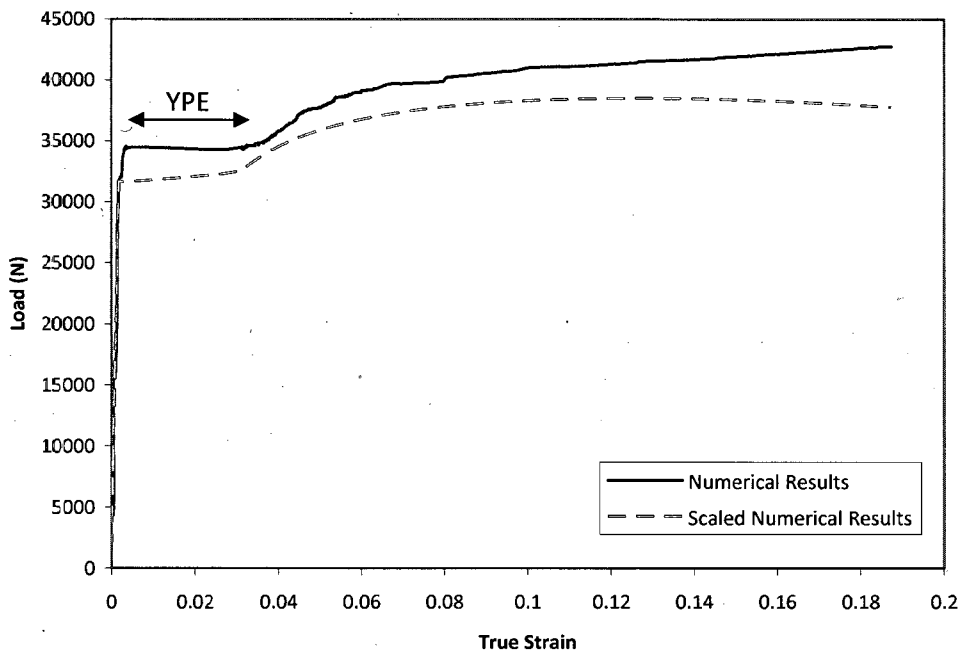


Figure 4.15 Numerical results for HSLA specimen in rolling direction before and after scaling in rolling direction.

The plane-strain stress-strain response of HSLA, obtained through the scaling of LS-DYNA results, is shown in Figure 4.16. Yield point elongation (YPE) can be seen up to a strain of about 0.033.

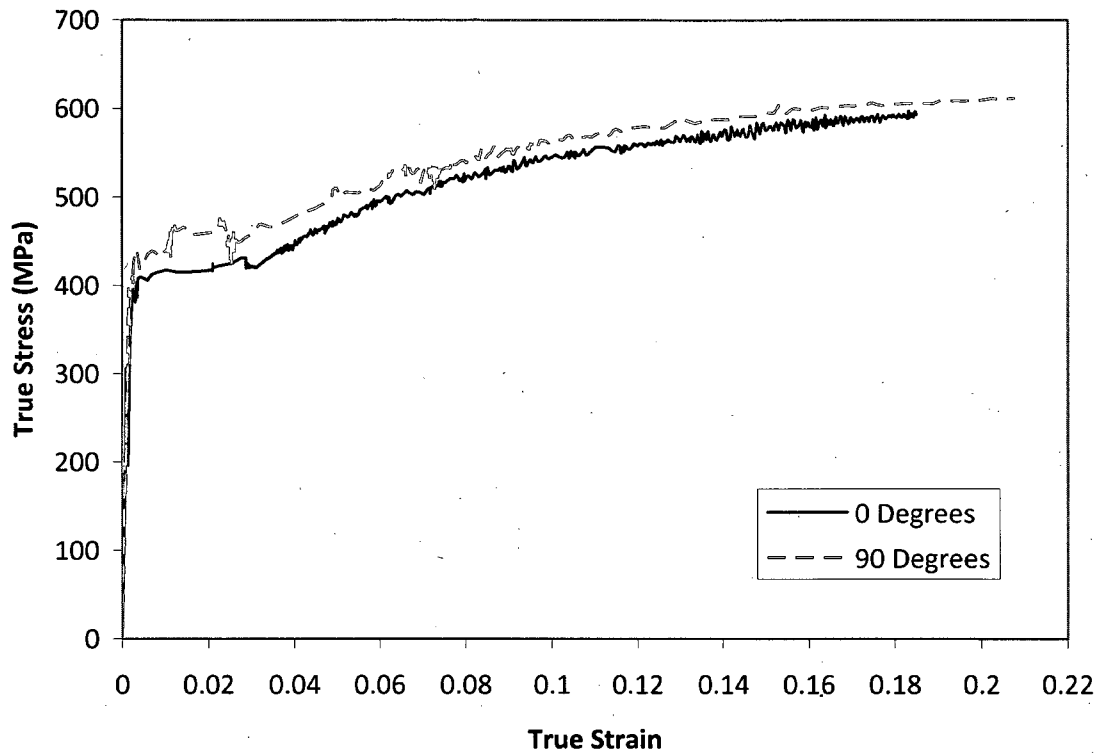


Figure 4.16 Estimated true stress-true strain behaviour of HSLA in plane-strain tension.

Figure 4.17 and Figure 4.18 show a comparison of stress-strain response predicted by Wagoner's method and scaled LS-DYNA analysis results. While HSLA plane strain results show a discrepancy between the Wagoner analysis and scaled LS-DYNA results, this results from both methods providing approximations of plane strain behaviour. An acceptable correlation between each method was observed. Scaled LS-DYNA results were used to obtain yield values, as shown in Figure 4.16.

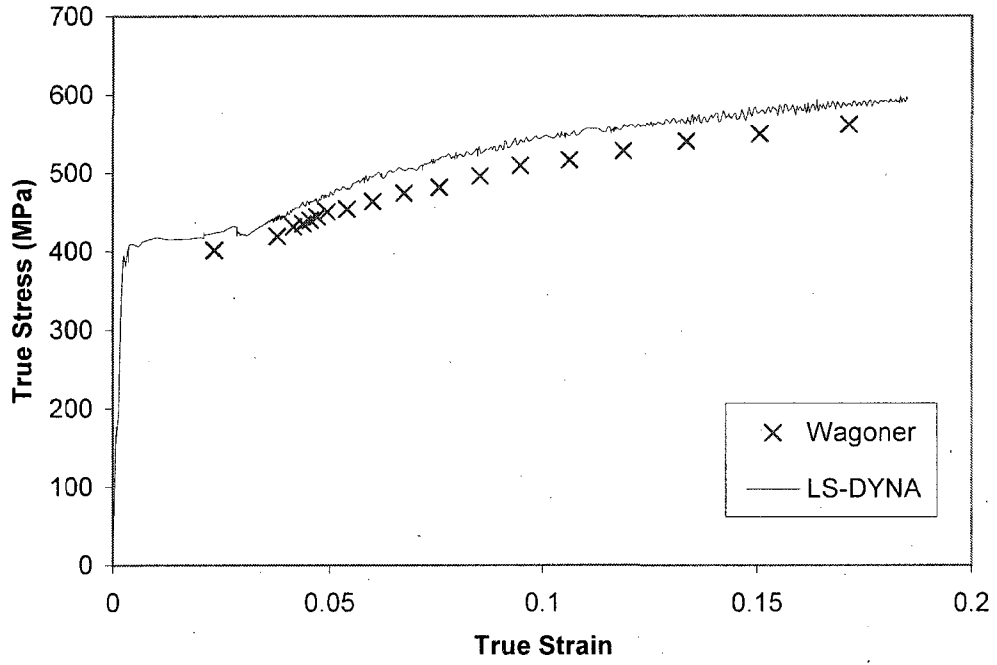


Figure 4.17 Comparison of the plane-strain behaviour of HSLA in the rolling direction as predicted by the Wagoner analysis method and by scaling the curves obtained from finite element simulation

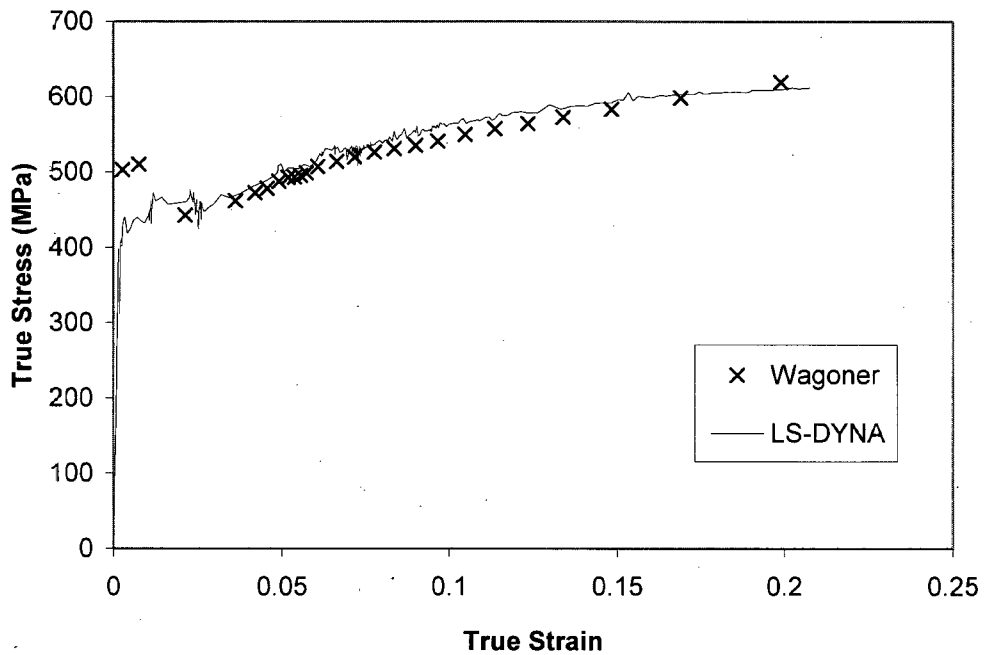


Figure 4.18 Comparison of the plane-strain behaviour of HSLA at 90 degrees to the rolling direction as predicted by the Wagoner analysis method and by scaling the curves obtained from finite element simulation

The strain distribution predicted for a representative plane-strain specimen corresponding to the experimental strain distribution shown in Figure 4.26 D ($\epsilon_1=0.0436$) is shown in Figure 4.19.

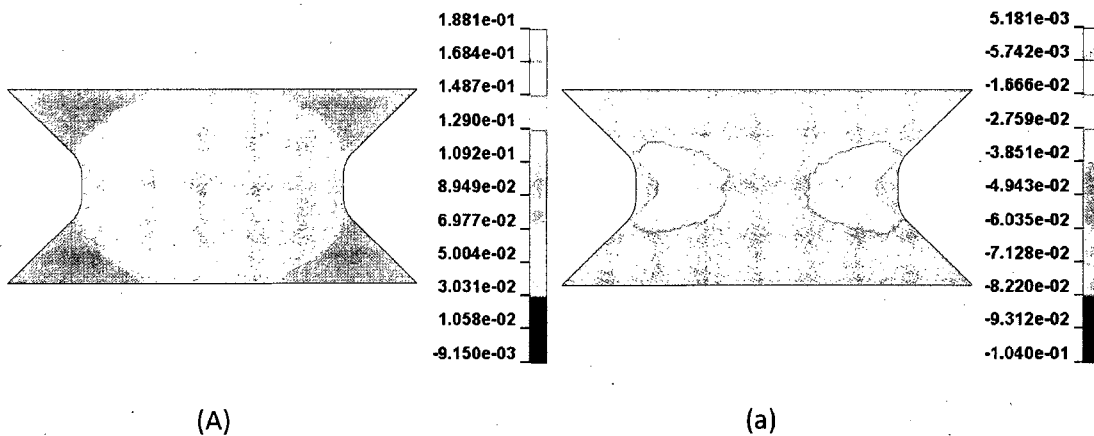


Figure 4.19 (A) Major and (a) minor strain distribution in DP600 plane-strain specimen predicted with LS-DYNA, at $\epsilon_1=0.0436$

While the numerical model predicts far larger values for both major and minor strains, it can be observed that these values are highly localized at the corner of the gauge region. A comparison of strains across the centre line of the gauge area shows similar distribution in both the numerically predicted and experimentally measured results. Similar strain distributions can be observed between numerical and experimental results for both the major and minor strains. It can be seen in the major strain distribution that strains in the transition region are minimal, which are observed to occur in experimental results during yield point elongation. A comparison of the numerical and experimental strain distribution of minor strains shows negligible strain values through most of the specimen.

Figure 4.20 presents the distribution of principal strains along the width of the gauge area of the plane-strain HSLA specimen, predicted by LS-DYNA.

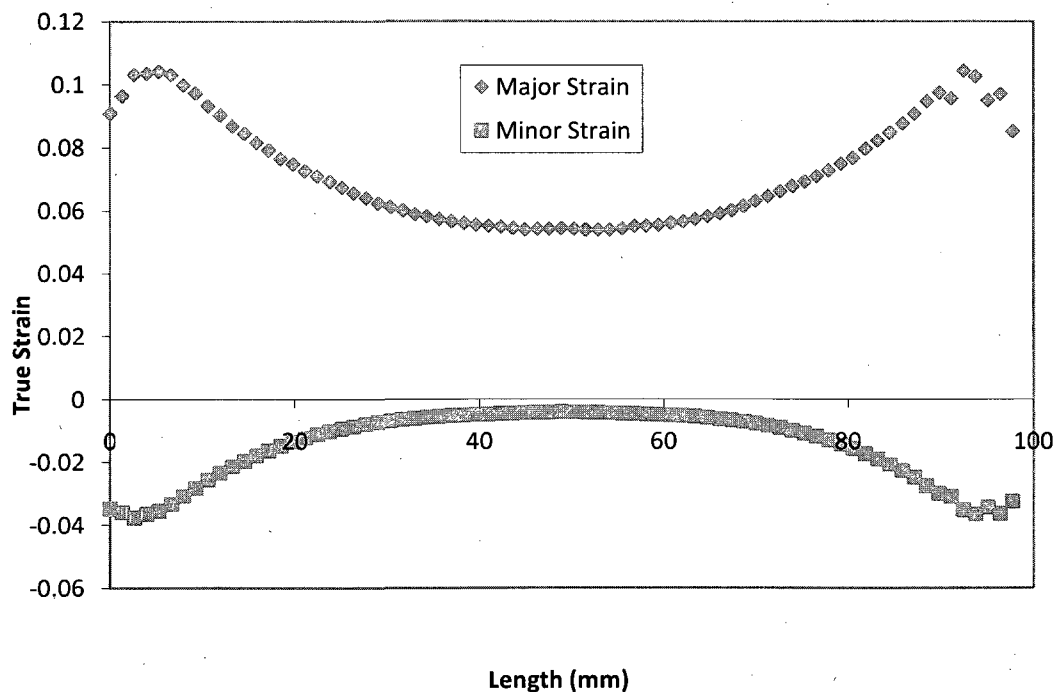


Figure 4.20 Distribution of true major and minor strains computed across the width of the gauge for numerical model of plane-strain HSLA specimen loaded in the rolling direction.

It should be noted that this numerical model was unable to predict the presence of Lüders bands in a material.

4.3 EXPERIMENTAL PLANE-STRAIN TENSION RESULTS

4.3.1 DP600

Figure 4.21 and Figure 4.22 show the experimental axial (Y) and transverse (X) strain distribution measured across the width of the gauge area of the 0 degree and 90 degree plane-strain specimens. Edge effects are evident; however, a plane-strain region can be observed in the centre of the specimen. Negligible minor strains can be observed across the width of the specimen, with the exception of the edge regions.

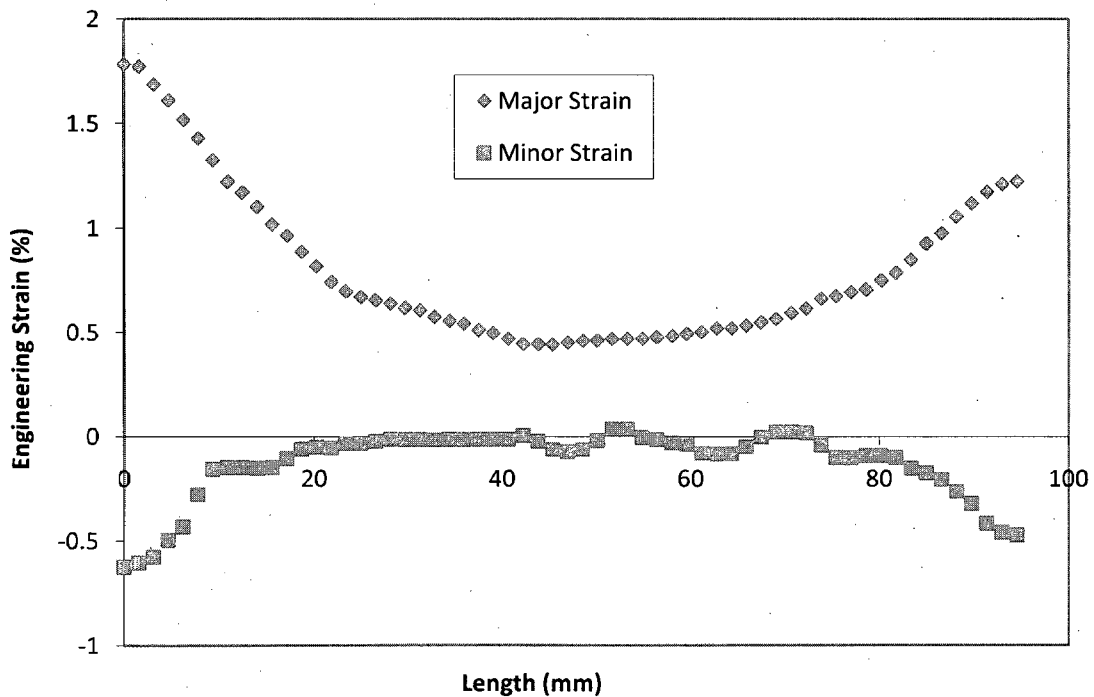


Figure 4.21 Distribution of axial major and minor engineering strains measured across the width of the gauge for plane-strain DP600 specimens loaded in the rolling direction.

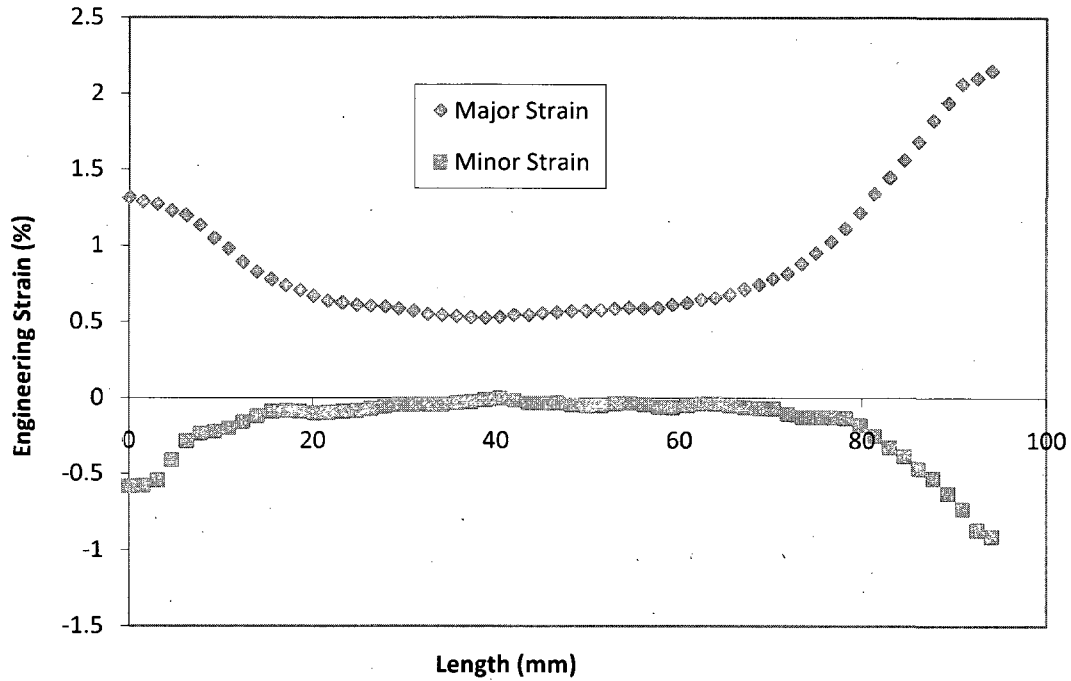
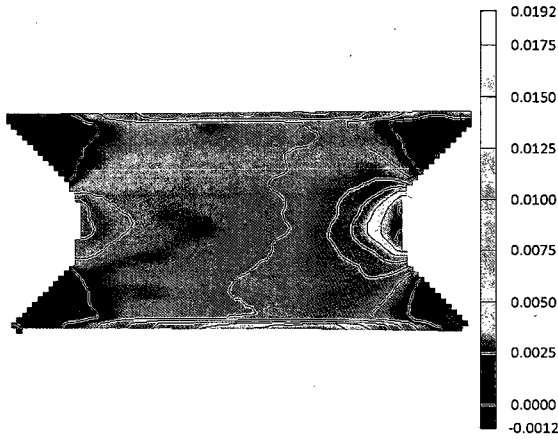
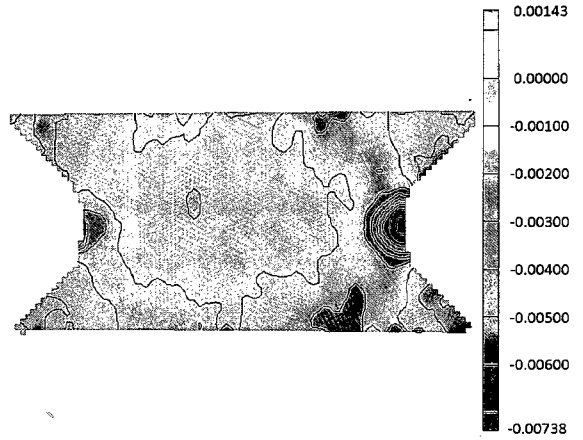


Figure 4.22 Distribution of axial major and minor engineering strains measured across the width of the gauge for plane-strain DP600 specimens loaded at 90 degrees to the rolling direction.

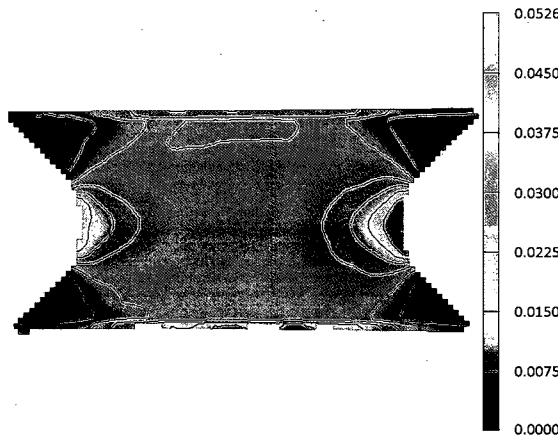
Figure 4.23 shows the strain distribution measured in the gauge area of the DP600 plane-strain specimen for different levels of deformation. Edge effects, as seen in Figure 4.21 and Figure 4.22 are evident for both the axial and transverse directions. However, a uniform strain state is evident in the centre of the gauge area.



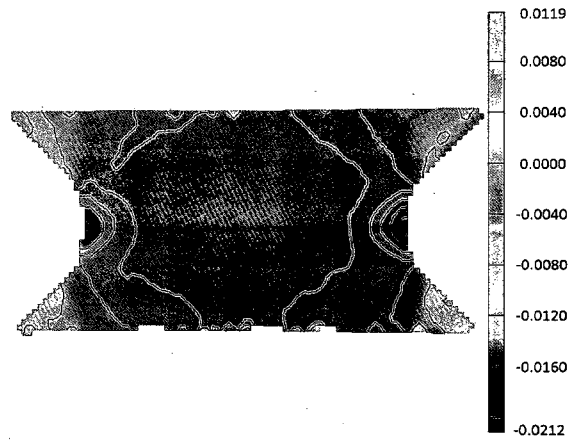
(A)



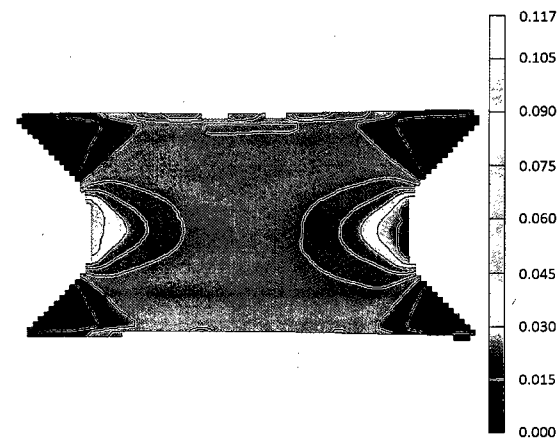
(a)



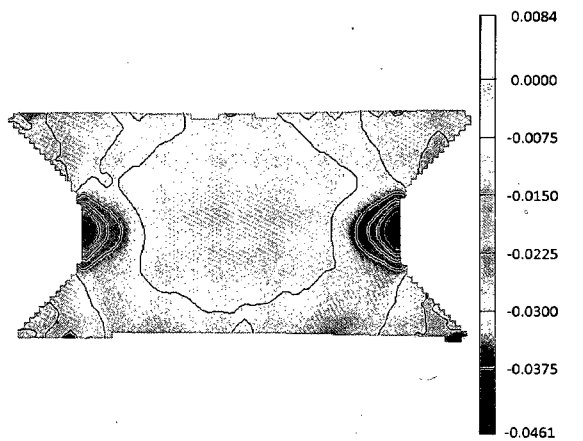
(B)



(b)



(C)



(c)

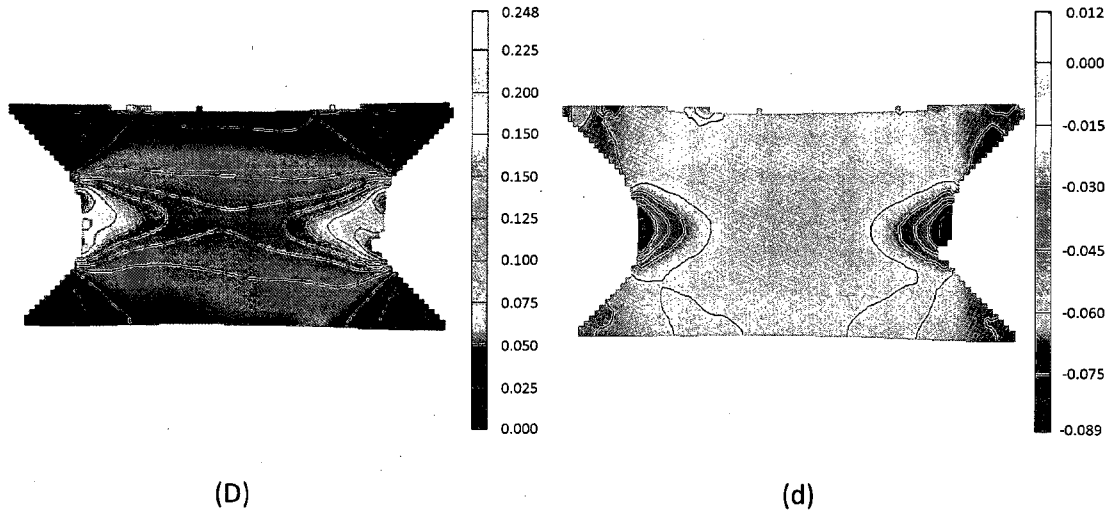


Figure 4.23 Distribution of (A-D) axial and (a-d) transverse true strains measured in the gauge area of DP600 plane-strain specimens, at (A) $\epsilon_1=0.00420$ (B) $\epsilon_1=0.0157$ (C) $\epsilon_1=0.0391$ (D) $\epsilon_1=0.103$

Yield values for the 0 and 90 degree plane-strain specimens are obtained from the scaled stress-strain curves (Figure 4.9) and listed in Table 7 and Table 8, respectively. It can be noted that plastic strain values were lower than those for the corresponding uniaxial tension work values. In some instances, a small amount of slipping was noted to occur during testing. Because of this, it is expected that yield stresses tending towards the upper end of the standard deviation provide a more accurate prediction of the plane strain response.

Plastic Work Per Unit Volume (MJ/m ³)	Yield Stress (MPa)	Standard Deviation (MPa)	Corresponding Plastic Strain
0.847	482	7.74	0.00187
2.27	536	7.32	0.00460
4.91	585	7.09	0.00924
10.6	642	7.78	0.0185
30.2	737	10.6	0.0463

Table 7 Flow stress in DP600 plane-strain specimens loaded in the sheet rolling direction

Plastic Work Per Unit Volume (MJ/m ³)	Yield Stress (MPa)	Standard Deviation (MPa)	Corresponding Plastic Strain
0.847	496	2.1	0.00182
2.27	550	4.4	0.00451
4.91	601	4.2	0.00908
10.6	662	2.5	0.0181
30.2	754	5.6	0.0454

Table 8 Flow stress in DP600 plane-strain specimens loaded in the sheet transverse direction

4.3.2 HSLA

Figure 4.24 and Figure 4.25 show the distribution of axial (Y) and transverse (X) engineering strains measured across the width of the gauge for HSLA plane-strain specimens. As with the DP600 plane-strain specimen, edge effects are apparent, but negligible transverse strains are evident in the centre of the specimen.

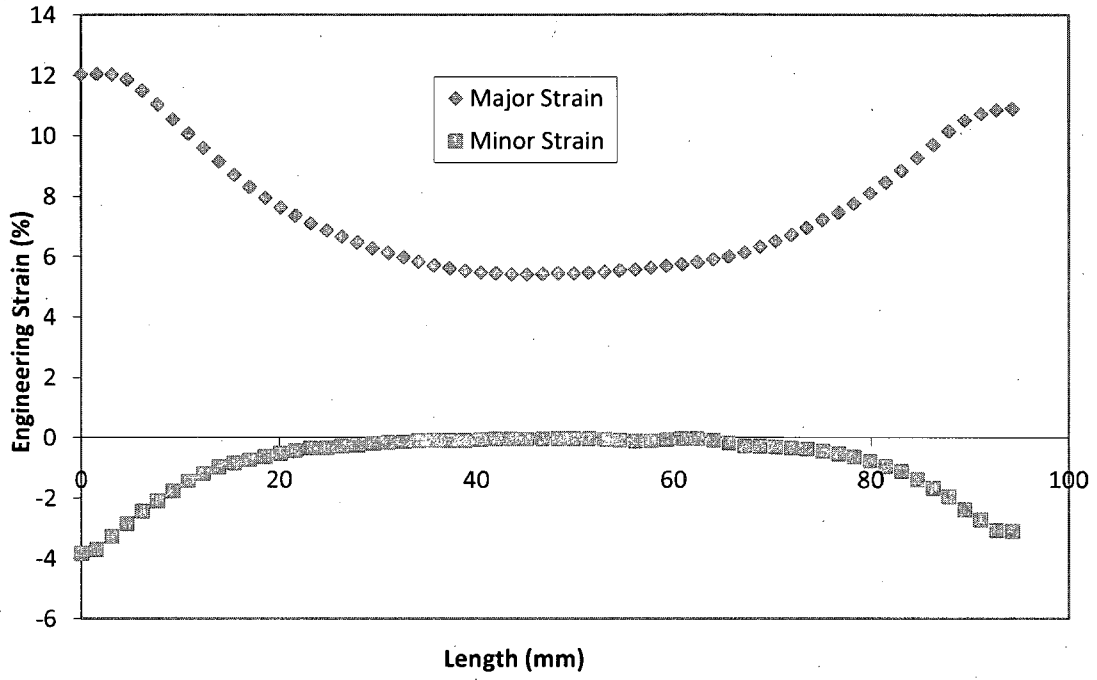


Figure 4.24 Distribution of axial major and minor engineering strains measured across the width of the gauge for plane-strain HSLA specimens loaded in the rolling direction.

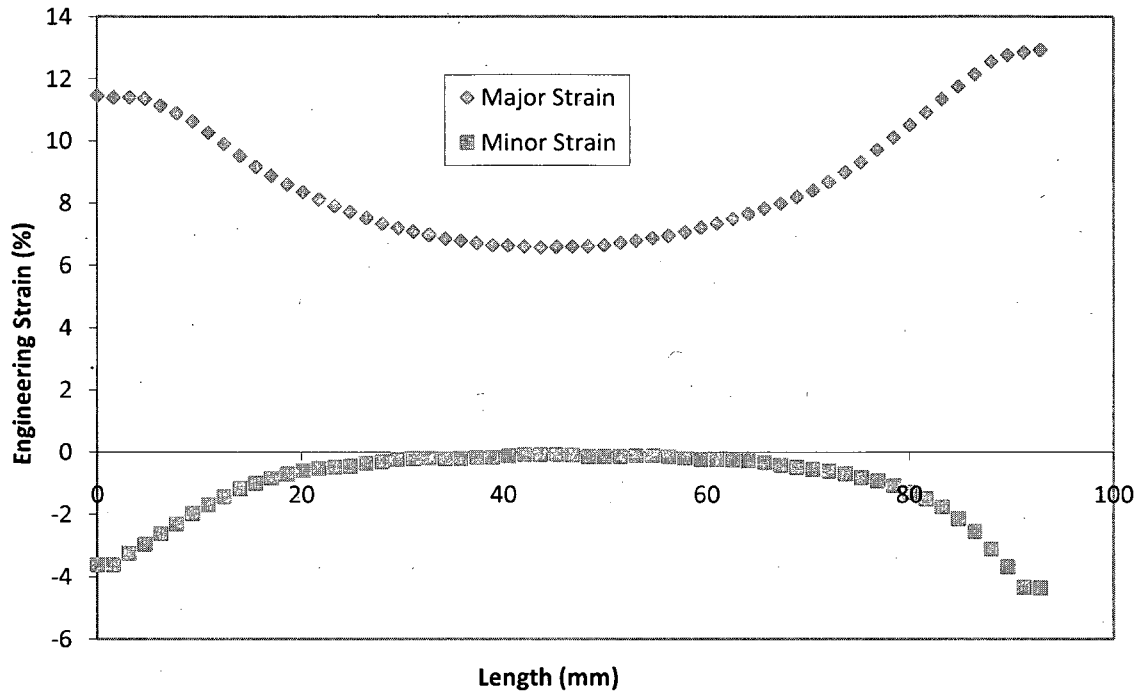
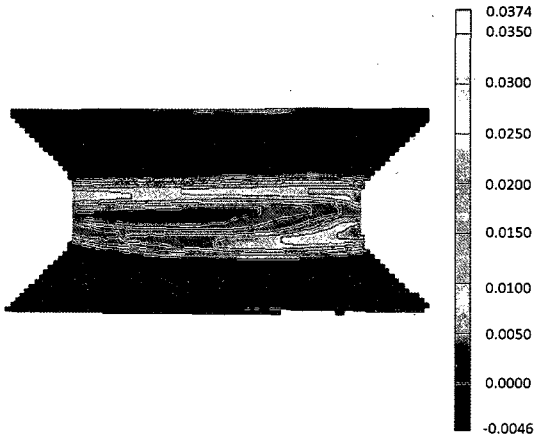
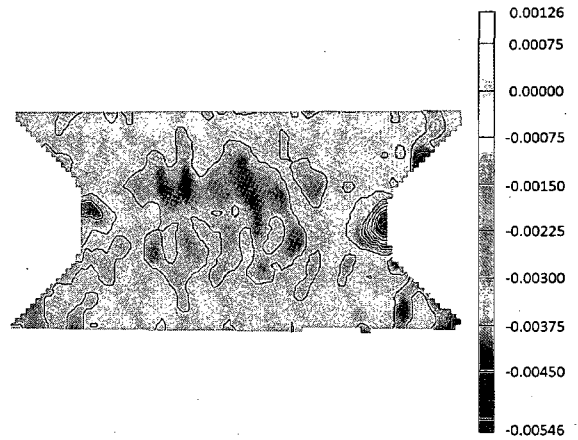


Figure 4.25 Distribution of axial major and minor engineering strains measured across the width of the gauge for plane-strain HSLA specimens loaded at 90 degrees to the rolling direction.

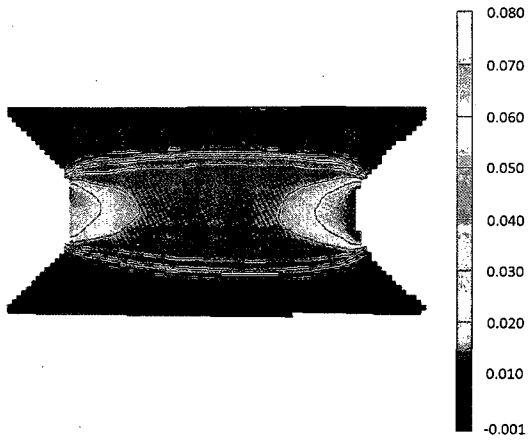
The strain distribution measured in the gauge area of the HSLA plane-strain specimens is shown in Figure 4.26. As with the tensile specimens, Lüders bands propagate through the plane-strain specimen as shown in Figure 4.26 A. Once the Lüders bands extend across the entire gauge of the specimen, a uniform strain distribution develops in the gauge, as shown in Figure 4.26 B, and regular strain hardening behaviour occurs, as shown in Figure 4.26 C. After a certain amount of work hardening, strain concentration at the edge of the gauge region cause increased strains (as indicated in Figure 4.26 D), and severe necking, following which fracture occurs at the edge of the gauge region, and propagates through the specimen. As shown in Figure 4.26 a-d, strain concentrations in compression occur at the edge of the gauge region. Transverse strains away from the edge of the gauge region are observed to be minimal.



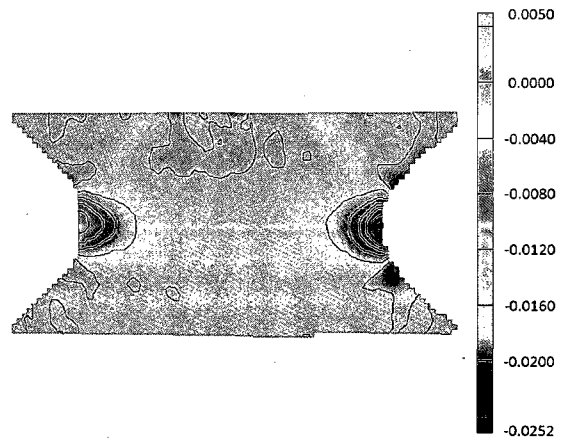
(A)



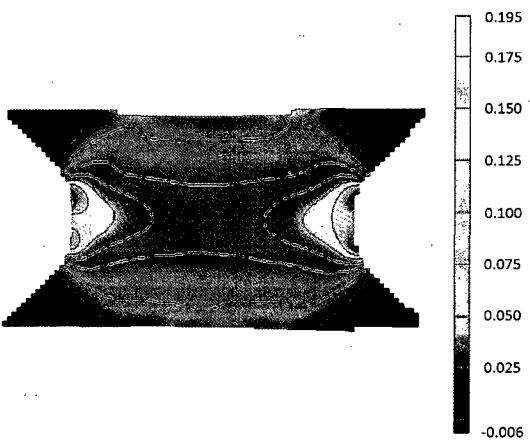
(a)



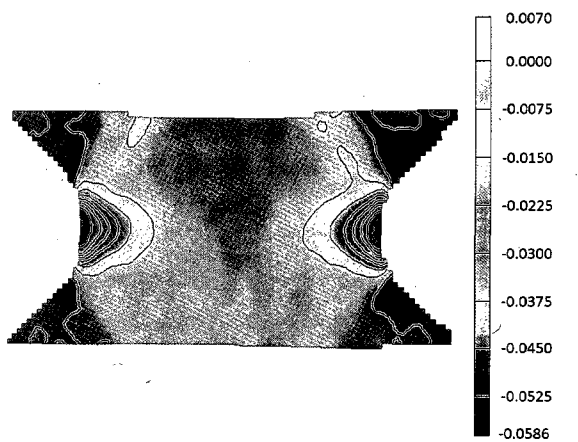
(B)



(b)



(C)



(c)

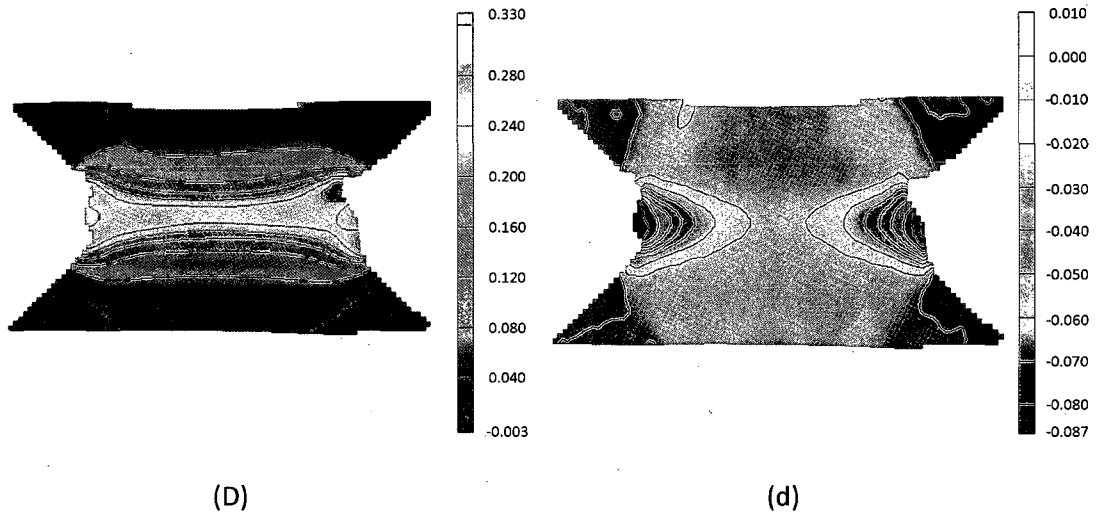


Figure 4.26 Distribution of axial (A-D) and transverse (a-d) true strains measured in the gauge area of HSLA plane-strain specimens, at (A) $\epsilon_1=0.00258$ (B) $\epsilon_1=0.0436$ (C) $\epsilon_1=0.0879$ (D) Fracture Onset

Table 9 lists the plane-strain yield stress values for HSLA, at 0 degrees to the rolling direction and Table 10 lists the corresponding values at 90 degrees to the rolling direction. With the exception of the initial yield value for 0 degrees, the plastic strain value is lower than the corresponding uniaxial tension work value. The reason for this exception is the similarity between the yield values (392 MPa for uniaxial tension in comparison to 409 MPa for plane-strain tension) and the use of an average plastic work value (a value of 0.918 was used for 0 degree plane-strain tension, as opposed to a value of 0.905 obtained for 0 degree uniaxial tension specimens).

Plastic Work Per Unit Volume (MJ/m ³)	Yield Stress (MPa)	Standard Deviation (MPa)	Corresponding Plastic Strain
0.918	414	4.95	0.00124
4.22	414	4.57	0.00520
8.34	421	3.12	0.0151
20.9	470	6.70	0.0481
44.4	536	6.39	0.0943

Table 9 Flow stress in HSLA plane-strain specimens loaded in the sheet rolling direction

Plastic Work Per Unit Volume (MJ/m ³)	Yield Stress (MPa)	Standard Deviation (MPa)	Corresponding Plastic Strain
0.918	446	8.75	0.00183
4.22	485	11.6	0.00794
8.34	460	12.9	0.0178
20.9	497	7.18	0.0423
44.4	558	8.84	0.0879

Table 10 Flow stress in HSLA plane-strain specimens loaded in the sheet transverse direction

4.4 UNIAXIAL COMPRESSION RESULTS

Uniaxial compression tests were performed on both DP600 and HSLA specimens. Due to the eccentricity in the testing equipment, buckling occurred at lower loads than predicted by Euler's equation. Figure 4.27 shows a representative stress-strain curve for DP600 up to the onset of buckling. The engineering stress-strain curves were converted to true-stress and yield values corresponding to 0.2% and 0.5% plastic strain offsets in tension were obtained for DP600 specimens. Unfortunately, HSLA specimens buckled at stresses of approximately 300 MPa, before yielding occurred, and therefore yield data in uniaxial compression was not obtained for this material.

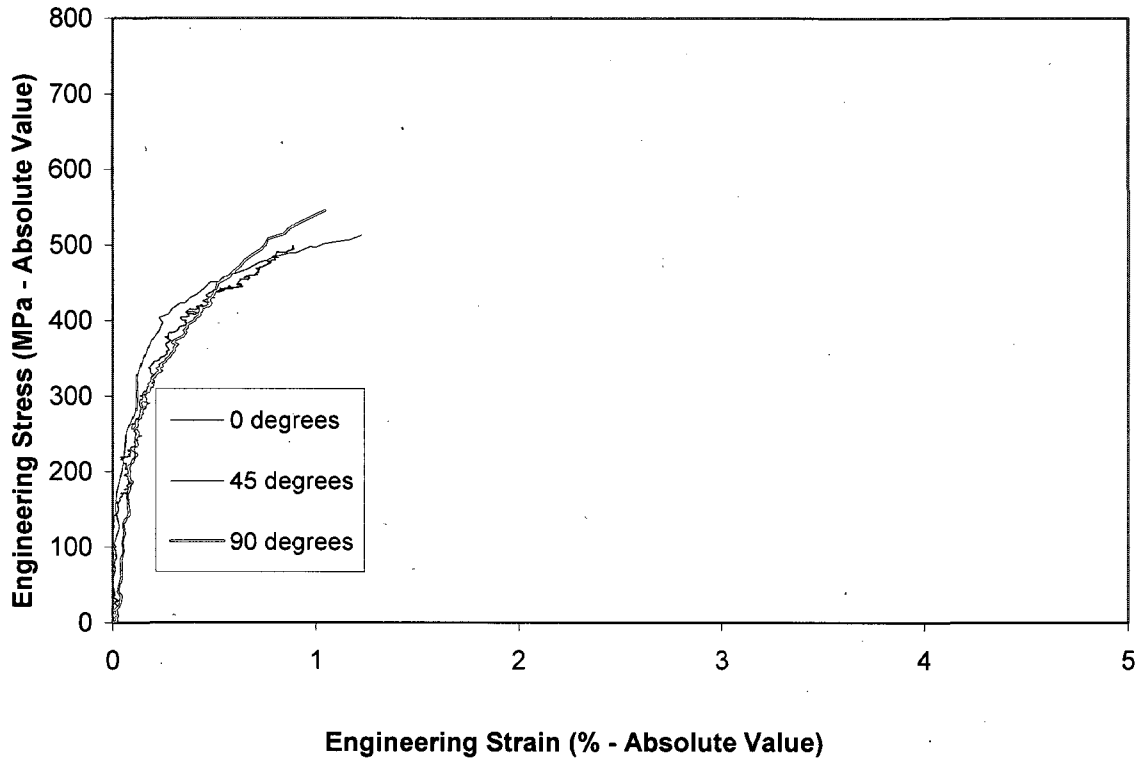


Figure 4.27 Engineering stress-strain response of DP600 specimens loaded in uniaxial compression

Yield stresses for various levels of plastic work per unit volume were obtained from uniaxial compression stress-strain data for 0 degree, 45 degree, and 90 degree specimens and are shown in Table 11, Table 12, and Table 13, respectively. Due to eccentricity in the system, large deviation values were observed in the compression results. Similar yield values and plastic strains were observed in uniaxial compression and uniaxial tension, however due to the averaging of uniaxial tension plastic work values, greater deviation of plastic strain was observed in the 0 degree results.

Plastic Work Per Unit Volume (MJ/m ³)	Yield Stress (MPa)	Standard Deviation (MPa)	Corresponding Plastic Strain
0.847	-390	24.0	-0.00253
2.27	-459	Insufficient Tests	-0.00600

Table 11 Flow stress in DP600 uniaxial compression specimens loaded in the sheet rolling direction

Plastic Work Per Unit Volume (MJ/m ³)	Yield Stress (MPa)	Standard Deviation (MPa)	Corresponding Plastic Strain
0.847	-418	23.4	-0.00197
2.27	-469	34.8	-0.00516

Table 12 Flow stress in DP600 uniaxial compression specimens loaded at 45 degrees to the sheet rolling direction

Plastic Work Per Unit Volume (MJ/m ³)	Yield Stress (MPa)	Standard Deviation (MPa)	Corresponding Plastic Strain
0.847	-437	36.7	-0.00216
2.27	-490	Insufficient Tests	-0.00519

Table 13 Flow stress in DP600 uniaxial compression specimens loaded at 90 degrees to the sheet rolling direction

It can be seen from Tables 11, 12, and 13, that due to premature buckling, the range of data is limited to low levels of plastic work. Bonded specimens buckled at loads similar to single thickness specimens, producing similar results.

4.5 OUTSOURCED TEST RESULTS

Stress-strain results for outsourced tests are shown in Appendix C. In this section, yield values for all outsourced tests are shown. In most instances, similar yield values and plastic strain values were observed for uniaxial compression results. Tables 15-18 present uniaxial compression yield values obtained from tests provided by Ohio State University. Due to the use of a support structure, buckling was prevented, allowing for larger yield values to be obtained over experimental results.

Plastic Work Per Unit Volume (MJ/m ³)	Yield Stress (MPa)	Corresponding Plastic Strain
0.847	-385	-0.00229
2.27	-461	-0.00566
4.91	-527	-0.0109
10.6	-595	-0.0209
30.2	-683	-0.0513

Table 14 Flow stress in DP600 uniaxial compression specimens loaded in the sheet rolling direction

Plastic Work Per Unit Volume (MJ/m ³)	Yield Stress (MPa)	Corresponding Plastic Strain
0.847	-453	-0.00197
2.27	-498	-0.00497
4.91	-547	-0.0100
10.6	-608	-0.0199
30.2	-699	-0.0495

Table 15 Flow stress in DP600 uniaxial compression specimens loaded at 90 degrees to the sheet rolling direction

Plastic Work Per Unit Volume (MJ/m ³)	Yield Stress (MPa)	Corresponding Plastic Strain
0.918	-382	-0.00232
4.22	-378	-0.0109
8.34	-374	-0.0219
20.9	-429	-0.0535
44.4	-483	-0.104

Table 16 Flow stress in HSLA uniaxial compression specimens loaded in the sheet rolling direction

Plastic Work Per Unit Volume (MJ/m ³)	Yield Stress (MPa)	Corresponding Plastic Strain
0.918	-428	-0.00205
4.22	-426	-0.00981
8.34	-422	-0.0194

Table 17 Flow stress in HSLA uniaxial compression specimens loaded at 90 degrees to the sheet rolling direction

It can be observed that yield stresses obtained for DP600 from Ohio State University data are in close agreement (within 4%) with experimental data obtained in-house.

Equibiaxial tension results, performed at the Alcoa Technical Center, were provided in the form of power law Hollomon and saturation stress Voce equations, which were fitted to the experimental data. The coefficients for these equations are listed in Table 18; however, it should be pointed out that neither Hollomon or Voce equations accurately predict initial plastic stress behaviour, as shown in Appendix C.

Specimen	Hollomon Model ($\sigma = K\varepsilon_p^n$)		Voce Model ($\sigma = A - B \exp(-C\varepsilon_p)$)		
	n	K, MPa	A, MPa	B, MPa	C
DP600 - 1	0.178	1168.61	842.15	385.41	18.187
DP600 - 2	0.177	1149.73	836.21	388.42	18.029
HSLA - 1	0.182	770.87	696.86	340.54	5.389
HSLA - 2	0.175	765.85	698.61	329.65	5.162

Table 18 Equibiaxial tension stress coefficients

Corresponding yield values for the equibiaxial tension tests are shown in Table 19 for DP600 and in Table 20 for HSLA. Stress values listed are the primary stress components, in the form $\sigma_{eb} = \sigma_x = \sigma_y$.

As with the plane-strain tension results, plastic strain values are less than the corresponding plastic strain values in uniaxial tension.

Plastic Work Per Unit Volume (MJ/m ³)	Yield Stress (MPa)	Standard Deviation (MPa)	Corresponding Plastic Strain
0.847	497	9.48	0.00128
2.27	521	4.62	0.00405
4.91	554	6.36	0.00891
10.6	605	6.70	0.0187
30.2	701	5.28	0.0483

Table 19 Flow stress in DP600 equibiaxial tension specimens

Plastic Work Per Unit Volume (MJ/m ³)	Yield Stress (MPa)	Standard Deviation (MPa)	Corresponding Plastic Strain
0.918	392	6.81	0.00191
4.22	412	1.93	0.0101
8.34	431	5.15	0.0198
20.9	473	7.33	0.0475
44.4	523	3.48	0.0952

Table 20 Flow stress in HSLA equibiaxial tension specimens

Results from the simple shear tests, as performed at the Université de Bretagne-Sud are shown in Table 21 and Table 22 for DP600 and HSLA, respectively. It can be observed that plastic strain values are considerably larger than corresponding uniaxial tension plastic work values; this is because yield stresses are also considerably lower; therefore, larger plastic strain values are required for corresponding plastic work values. As the ratio between shear stress and uniaxial tension values is greater than the ratio between plane-strain tension and uniaxial tension, the difference in plastic strain values is greater. Values of the primary stresses are shown in the form $\sigma_{xy} = \sigma_x = -\sigma_y$. Yield point elongation can also be observed in simple shear for HSLA.

Plastic Work Per Unit Volume (MJ/m ³)	Yield Stress (MPa)	Corresponding Plastic Strain
0.847	226	0.00384
2.27	259	0.00947
4.90	286	0.0188
10.6	319	0.0374
30.2	367	0.0934

Table 21 DP600 - Simple shear yield values

Plastic Work Per Unit Volume (MJ/m ³)	Yield Stress (MPa)	Corresponding Plastic Strain
0.918	198	0.00265
4.22	199	0.0185
8.34	201	0.0392
20.9	231	0.0990
44.4	262	0.193

Table 22 HSLA - Simple shear yield values

4.6 YIELD LOCI

Following the analysis of the experimental data for uniaxial tension and compression tests, plane-strain and equibiaxial tension tests, and simple shear tests, experimental yield stresses were determined for each of the deformation modes and plotted in principal stress space. The yield data is presented in the form of constant work loci, since all yield stresses were determined for consistent levels of plastic work per unit volume.

For each set of yield data, the various yield functions described in Section 2.2 were also plotted in principal stress space using R-values and yield stresses to determine anisotropy coefficients. For

each level of plastic work per unit volume, yield stresses were normalized with respect to the yield stress in the rolling direction.

Hill's 1948 R-based yield criterion is independent of yield stress, and remains constant for each level of plastic work. Since \bar{R} is also independent of yield stress, the exponent m in Hill's 1979 function is the only value that is dependent on yield stress. For Hill's 1948 stress-based yield criterion, and Barlat's Yld2000-2d yield function coefficients are dependent on yield stresses, and evolve with yield offsets. Both DP600 and HSLA have BCC structures and, as such, the value $\alpha = 6$ was used.

For each level of plastic work, the loci are shown in Figures 4.26 - 4.35.

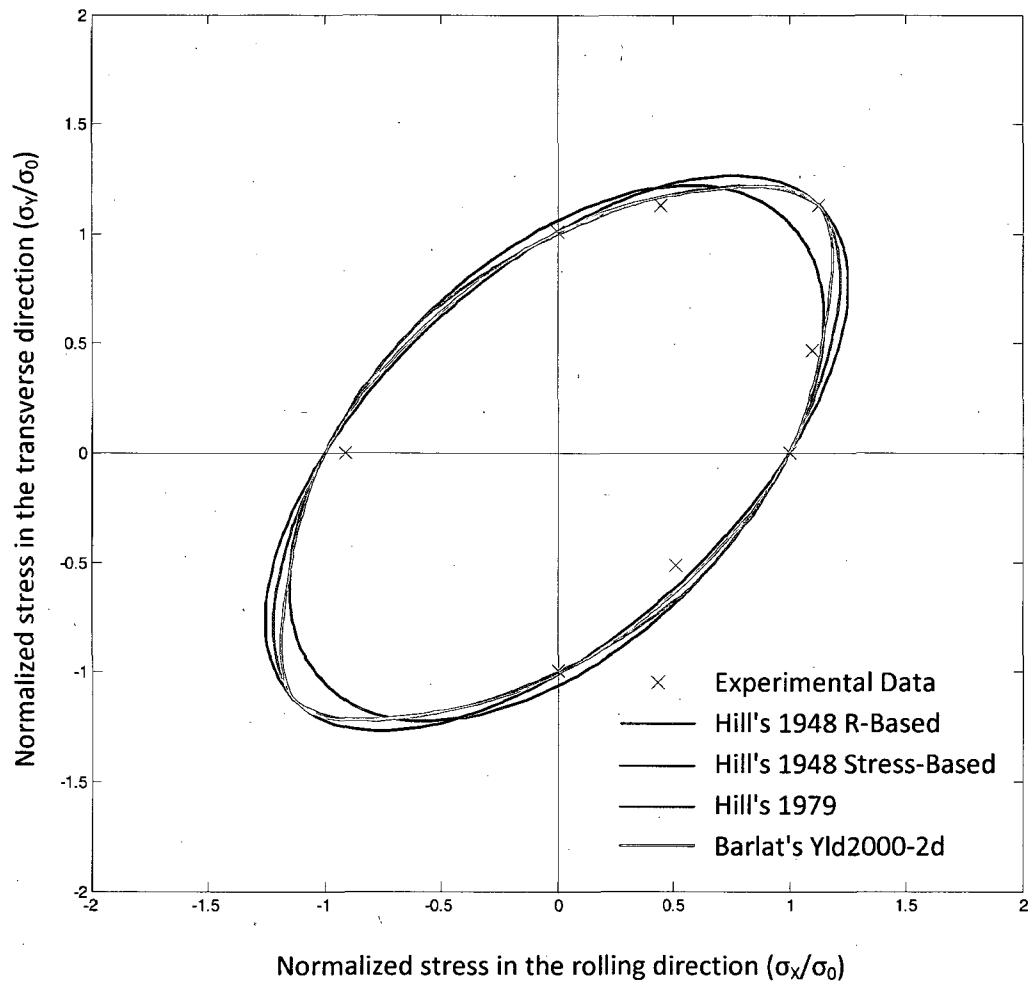


**Figure 4.28 DP600 yield loci for plastic work value of 0.870 MJ/m^3
(0.2% plastic strain offset in uniaxial tension)**

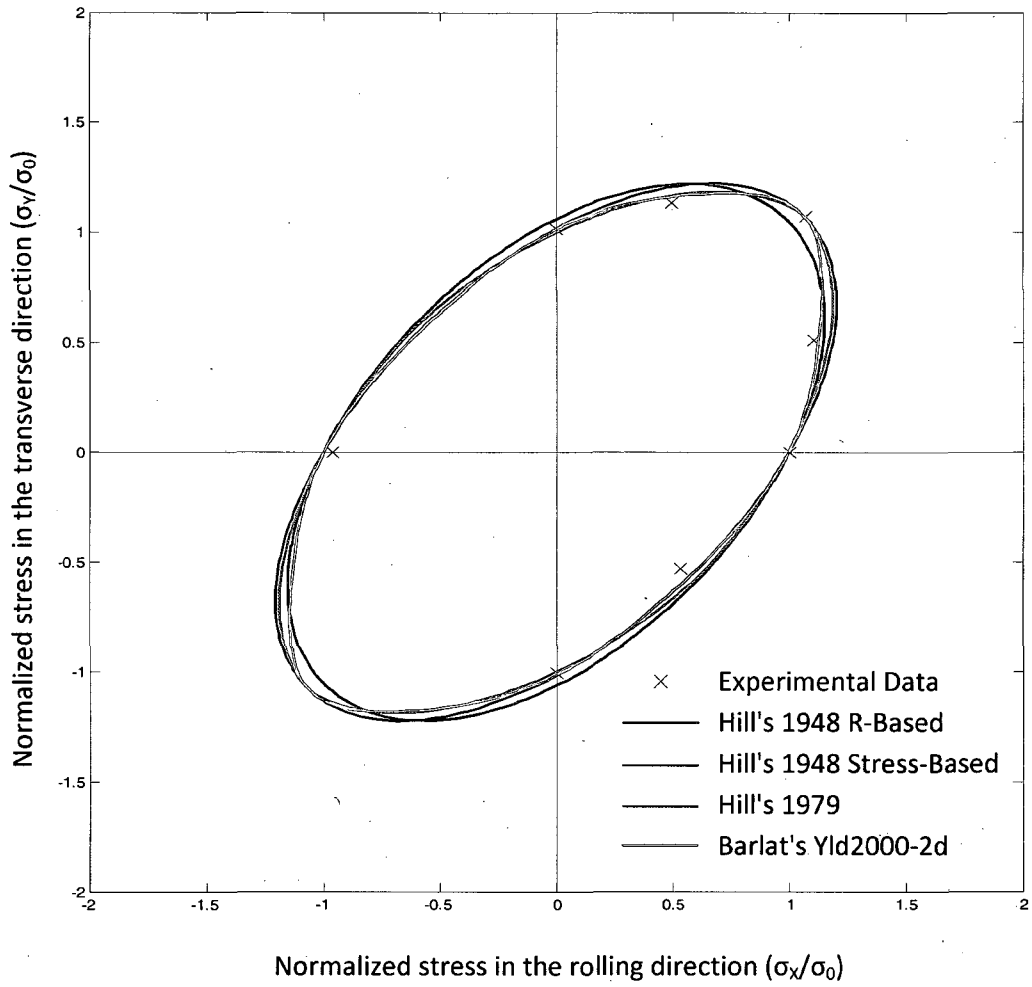


**Figure 4.29 DP600 yield loci for plastic work value of 2.30 MJ/m^3
(0.5% plastic strain offset in uniaxial tension)**

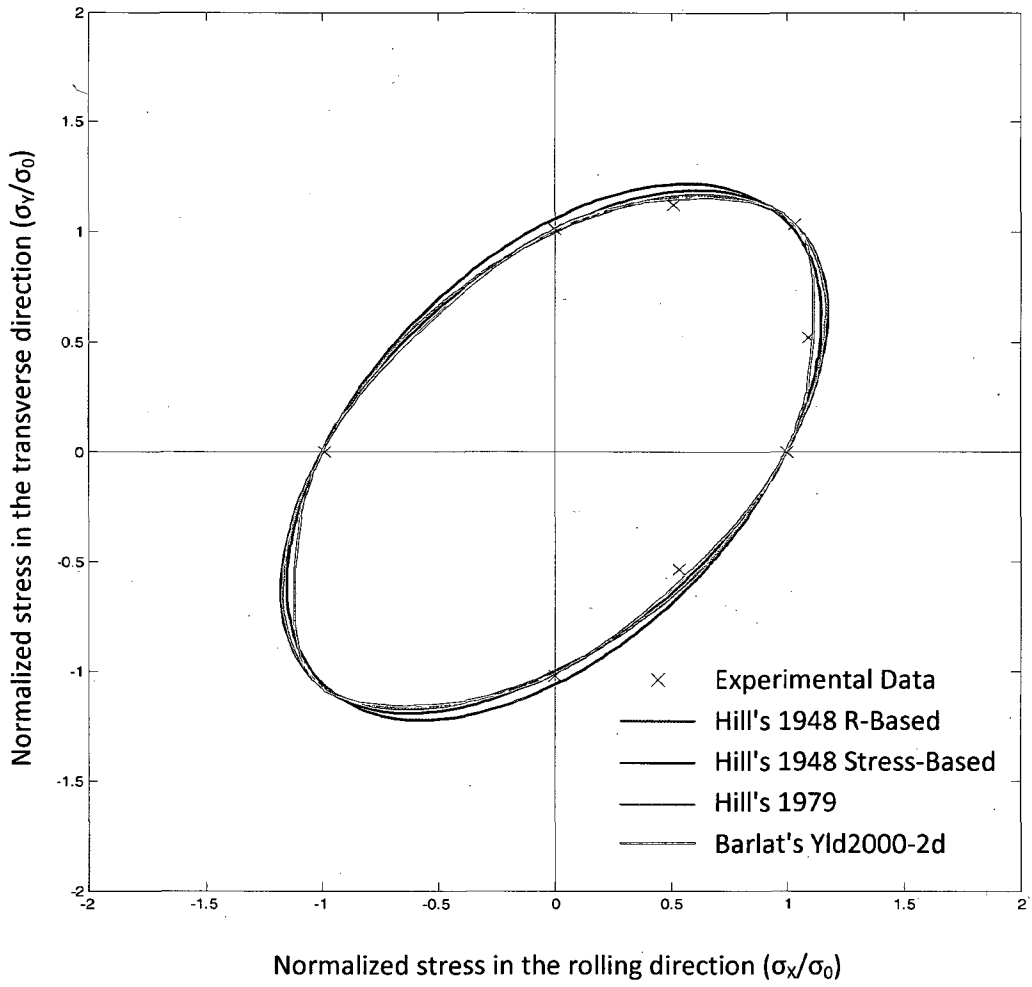


**Figure 4.30 DP600 yield loci for plastic work value of 4.95 MJ/m^3
(1.0% plastic strain offset in uniaxial tension)**

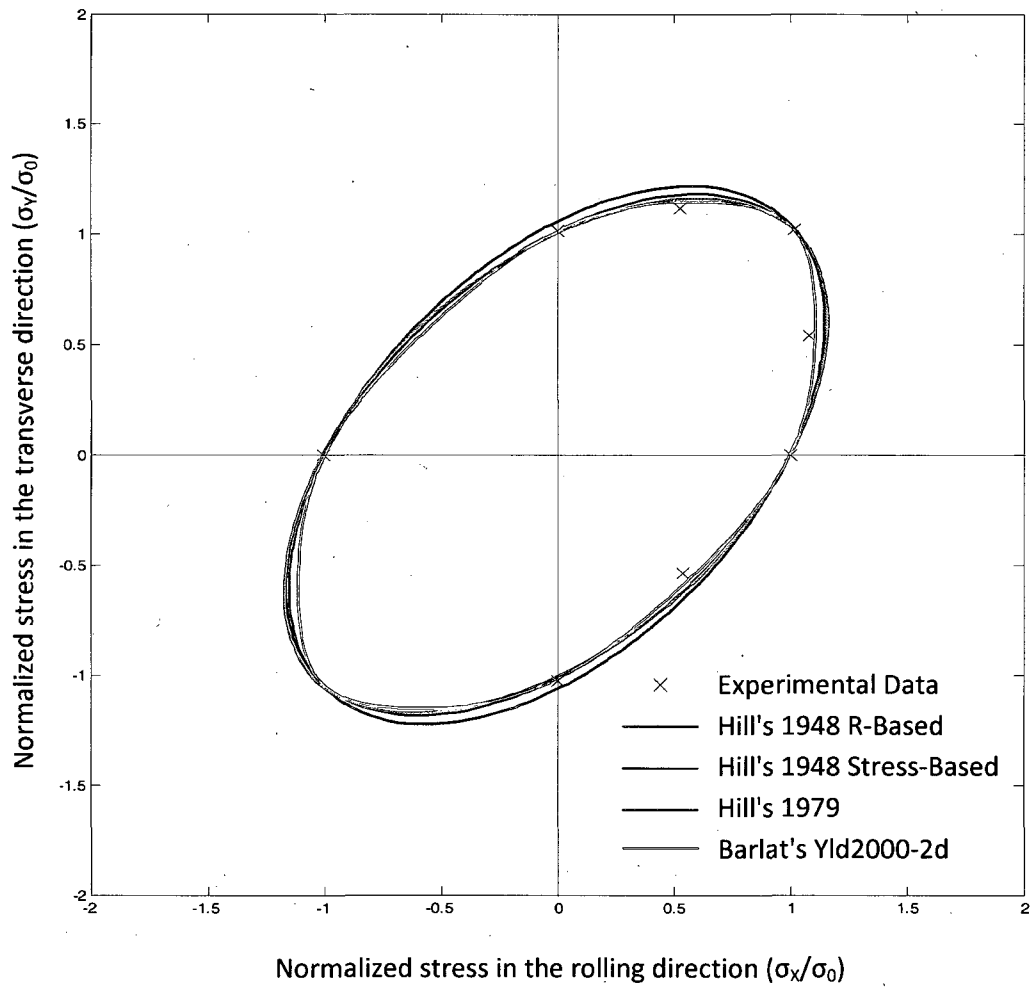


**Figure 4.31 DP600 yield loci for plastic work value of 10.7 MJ/m^3
(2.0% plastic strain offset in uniaxial tension)**

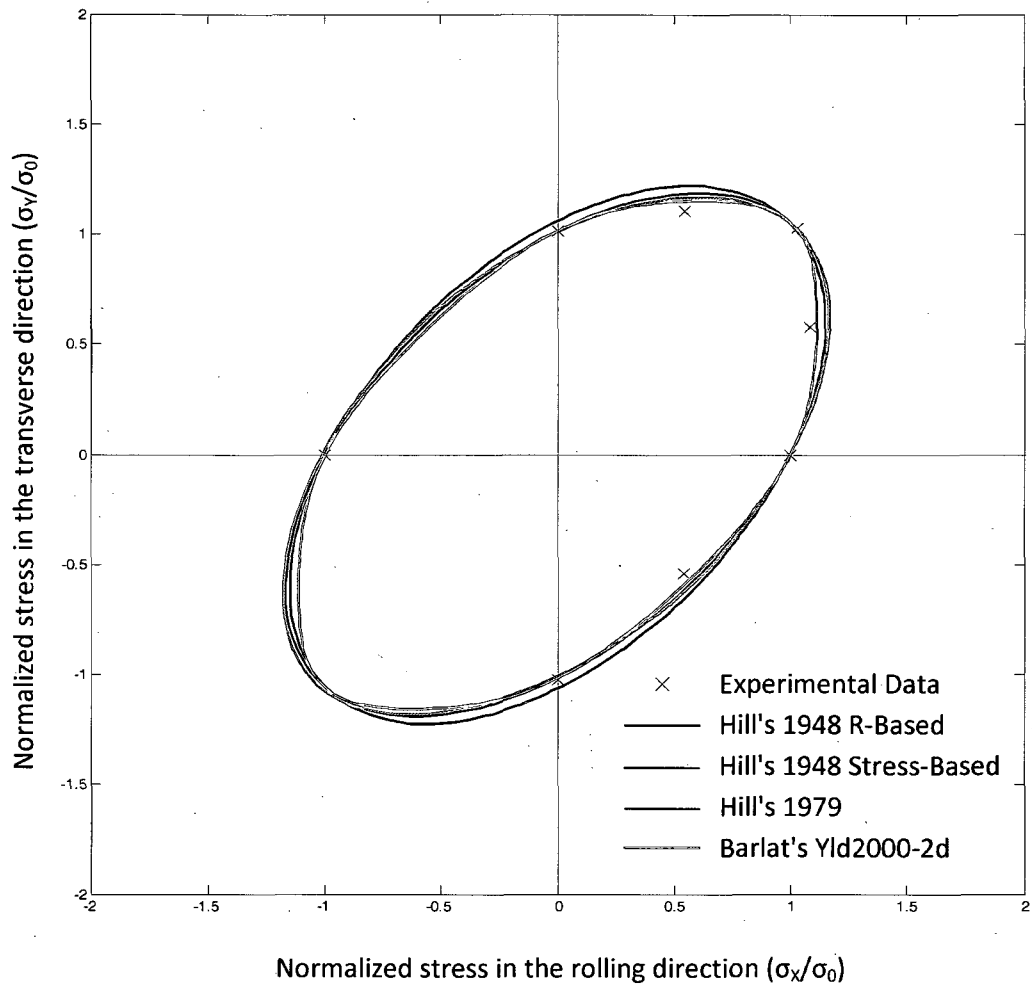


**Figure 4.32 DP600 yield loci for plastic work value of 30.4 MJ/m^3
(5.0% plastic strain offset in uniaxial tension)**

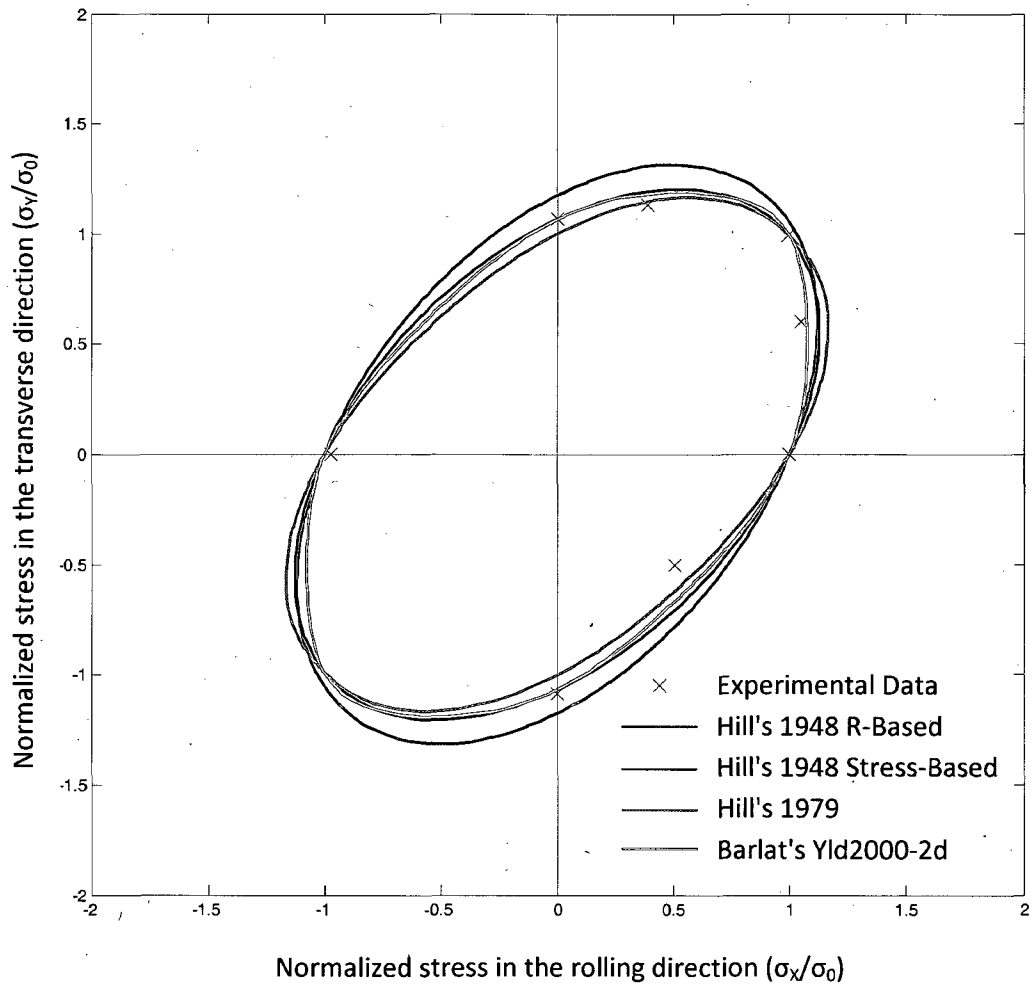


**Figure 4.33 HSLA yield loci for plastic work value of 0.918 MJ/m^3
(0.2% plastic strain offset in uniaxial tension)**

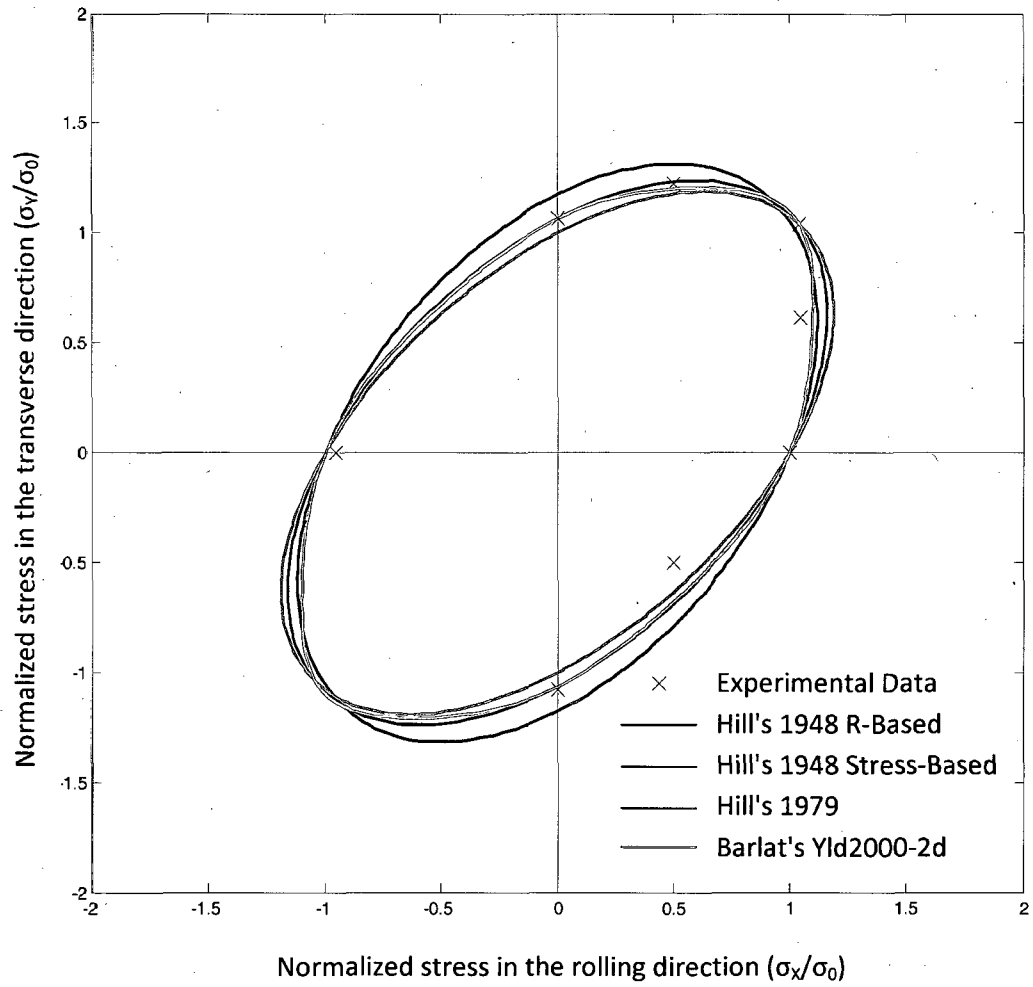


**Figure 4.34 HSLA yield loci for plastic work value of 4.22 MJ/m^3
(1.0% plastic strain offset in uniaxial tension)**

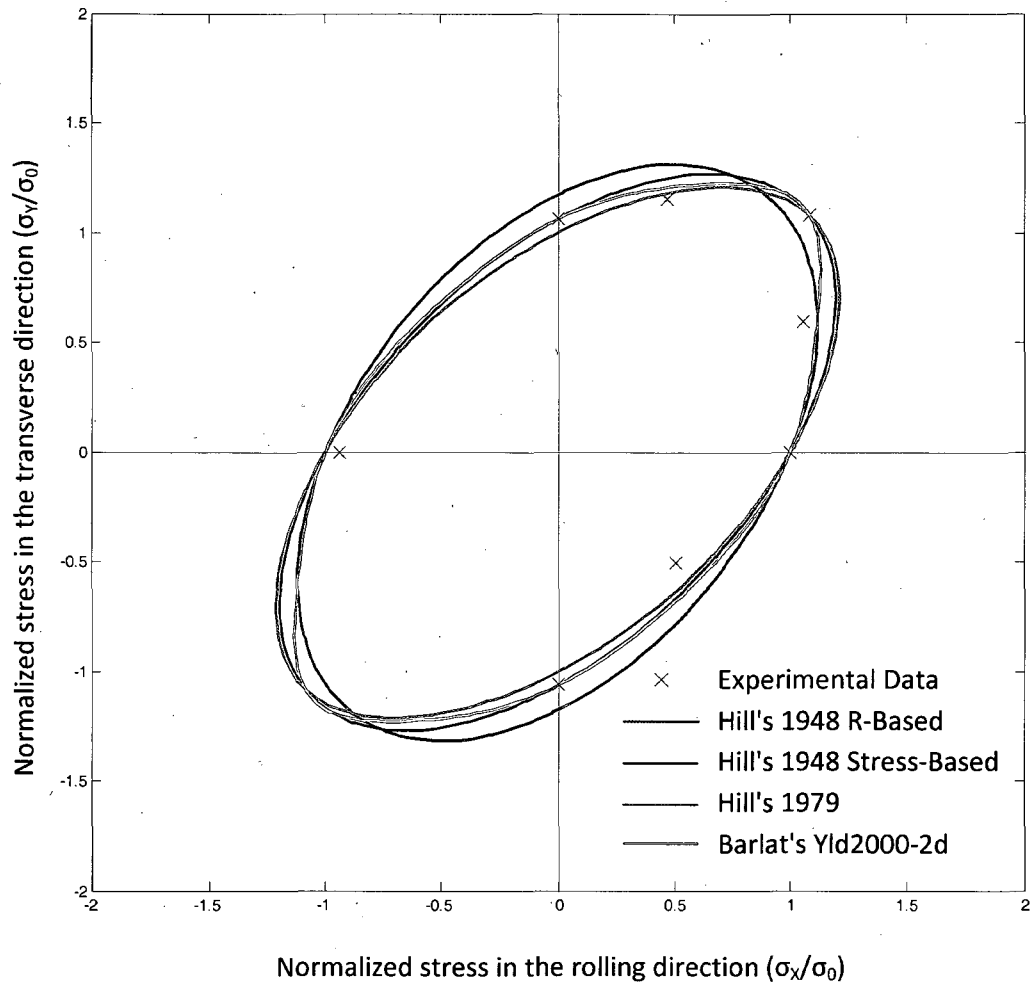


**Figure 4.35 HSLA yield loci for plastic work value of 8.34 MJ/m³
(2.0% plastic strain offset in uniaxial tension)**

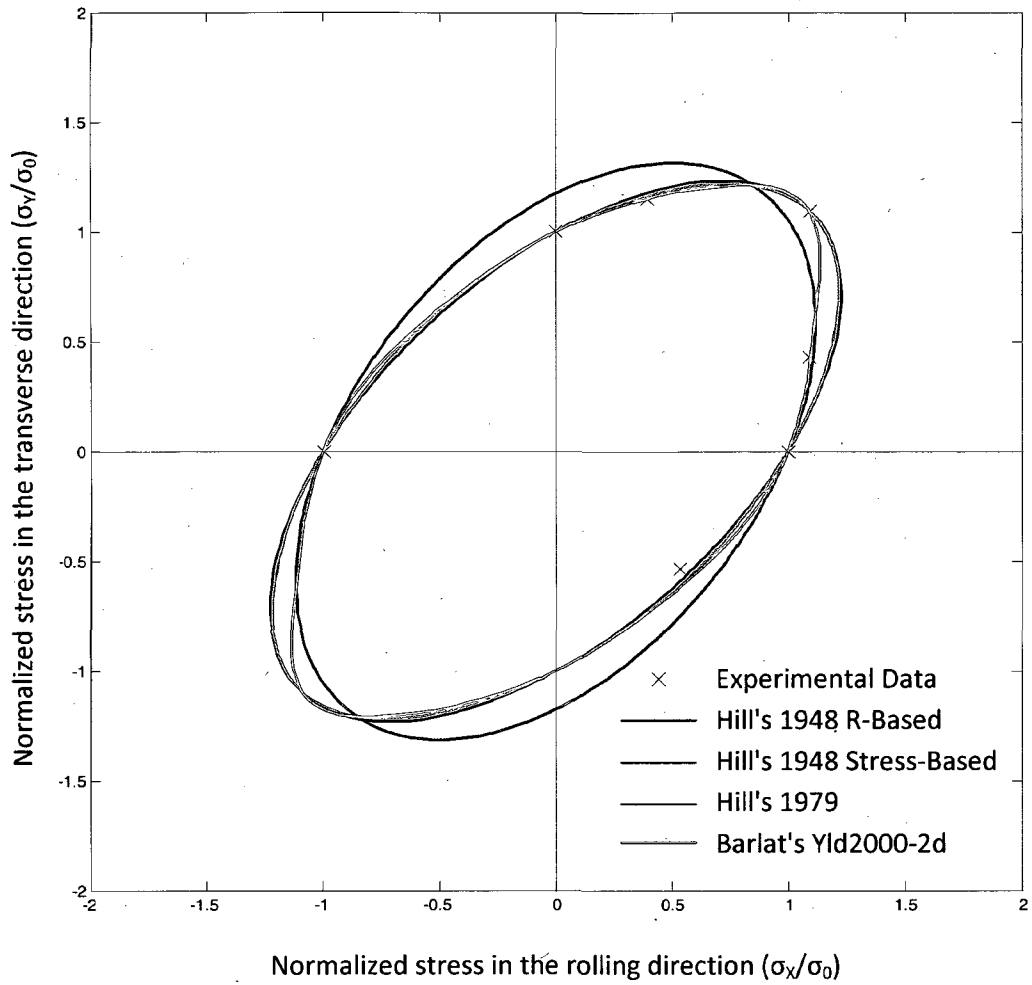


**Figure 4.36 HSLA yield loci for plastic work value of 20.9 MJ/m³
(5.0% plastic strain offset in uniaxial tension)**

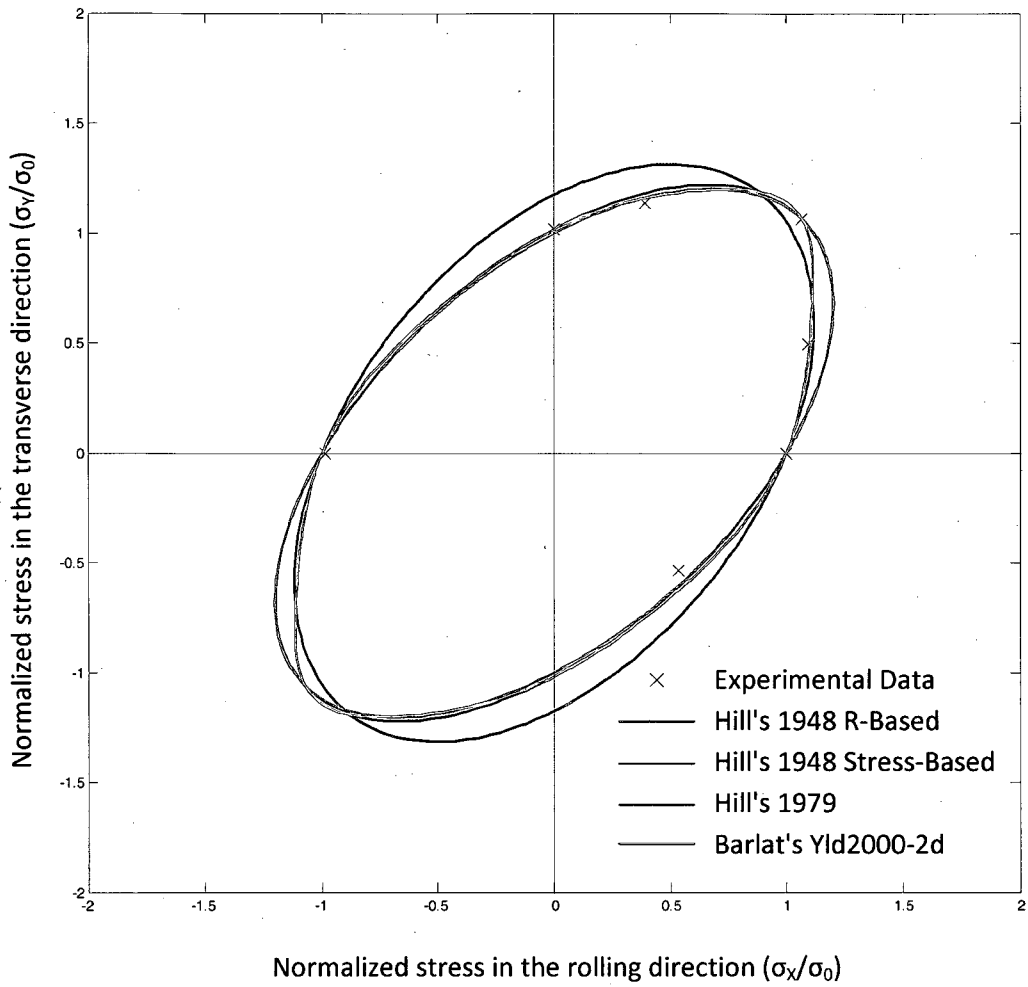


**Figure 4.37 HSLA yield loci for plastic work value of 44.4 MJ/m^3
(10.0% plastic strain offset in uniaxial tension)**

4.6.1 DP600

Hill's 1948 R-based yield function was obtained using equation 2.10 with values indicated in section 4.1.1. As this function is independent of yield stresses, it can be observed that the corresponding yield function does not change with increasing values of plastic work per unit volume.

Hill's 1948 stress-based yield function was obtained with equations 2.4-2.9. The corresponding anisotropy coefficients are listed for each level of plastic work in Table 23.

Anisotropy Coefficient	Plastic Work Per Unit Volume (MJ/m ³)				
	0.870	2.30	4.95	10.7	30.4
F	0.3820	0.4198	0.4537	0.4634	0.4574
G	0.4025	0.4512	0.4768	0.4946	0.4885
H	0.5975	0.5488	0.5232	0.5054	0.5115
N	1.6078	1.5645	1.5348	1.5210	1.5271

Table 23 Anisotropy coefficients for Hill's 1948 stress-based yield function

Hill's 1979 yield function was obtained using equation 2.12, with the m parameter obtained by fitting the yield function to the equibiaxial yield stress. m values of 1.6863, 1.8022, 1.8838, 1.9222, and 1.9053 were obtained for each level of plastic work.

Barlat's Yld2000-2d yield function was obtained using equation 2.13. Anisotropy coefficients for Yld2000-2d are listed in Table 24.

	Plastic Work Per Unit Volume (MJ/m ³)				
Anisotropy Coefficient	0.870	2.30	4.95	10.7	30.4
α_1	0.9168	0.9544	0.9640	0.9766	0.9737
α_2	1.0151	0.9995	1.0082	0.9984	0.9988
α_3	0.7512	0.8527	0.9083	0.9407	0.8387
α_4	0.9354	0.9511	0.9644	0.9680	0.9658
α_5	0.9648	0.9868	1.0005	1.0059	1.0032
α_6	0.7530	0.8678	0.9444	0.9787	0.9635
α_7	0.9507	0.9644	0.9784	0.9800	0.9802
α_8	1.1182	1.0539	1.0312	1.0064	1.0201

Table 24 Anisotropy coefficients for Barlat's Yld2000-2d

The effect of the equibiaxial yield stress on the yield locus is apparent in the obtained yield loci. For plastic work values of 0.870 and 2.30, the corresponding yield stress in equibiaxial tension is greater than in plane-strain tension. This is a result of the difficulties associated with obtaining accurate data at low strains, as indicated in section 2.3.2. Increased equibiaxial tension yield values result in the elongation of the yield locus. This elongation is evident when the yield loci are compared to Hill's 1948 R-based yield locus, which is independent of yield values.

For levels of plastic work in which the equibiaxial yield stress is less than the corresponding plane-strain yield stress, there is good agreement between the different yield functions. It can be observed that, for values of plastic work where the equibiaxial yield stress is greater than the corresponding plane-strain yield stresses, plane-strain yielding occurs with a larger minor stress compared to those predicted by Hill's 1948 R-based yield function. This occurs as a result of the elongation of the yield locus, and similar minor stresses are predicted in instances where the equibiaxial yield stress is less than the corresponding plane-strain yield stress.

Hill's 1948 R-based yield function provides an accurate representation of experimentally obtained yield values for levels of plastic work where the equibiaxial yield stress was less than the corresponding plane-strain yield stress. As a larger R-value was obtained in the 90 degree direction than the 0 degree direction, a slight elongation of the yield locus occurred along the σ_2 axis. It can be seen that this results in a slight over-prediction of the uniaxial yield stress in the transverse direction. With the exception of plastic work values of 0.870 and 2.30, Hill's 1948 R-based yield function is able to accurately predict yielding in equibiaxial tension. The discrepancy at lower values of plastic work occurs due to experimental error associated with equibiaxial tension tests at low strain levels as indicated in section 2.3.2.

The form of Hill's 1948 stress-based yield function ensures that, unlike Hill's 1948 R-based yield function, it exactly predicts the yield stresses in uniaxial tension in both the rolling and transverse directions and in equibiaxial tension. It can be observed that Hill's 1948 stress-based yield criterion provides the greatest over-prediction of yielding in plane-strain tension in the rolling and transverse directions. The amount to which Hill's 1948 stress-based yield function over-predicts plane-strain yielding is minimal.

As Hill's 1979 yield function describes normal anisotropy (planar isotropy), it is evident that it will predict the same uniaxial yield stress in both the rolling and transverse directions. This results in Hill's 1979 yield function slightly under-predicting yielding in the transverse direction, where the yield stress is greater than in the rolling direction, and providing a more accurate representation of plane-strain in the transverse direction than in the rolling direction.

Barlat's Yld2000-2d locus appears closer to the shape of the Tresca yield locus in the vicinity of plane-strain tension, and as a result, corresponds more accurately to the plane-strain condition. It can also be noted that, with the exception of plastic work values of 0.870 and 2.30, Barlat's Yld2000-2d yield function provides the most accurate prediction of yielding in pure shear. Alpha coefficients for Barlat's Yld2000-2d can be observed to be in the vicinity of 1.0. This indicates a low level of

anisotropy, which can also be observed in the small degree of deviation between yield values, and the proximity of R-values to 1.0.

It can be seen in Figure 4.38 that, when the range of plane-strain values obtained are considered, Barlat's Yld2000-2d is able to provide a close approximation of plane-strain yield stresses, providing an accurate representation of yielding in the positive σ_1 - σ_2 quadrant.

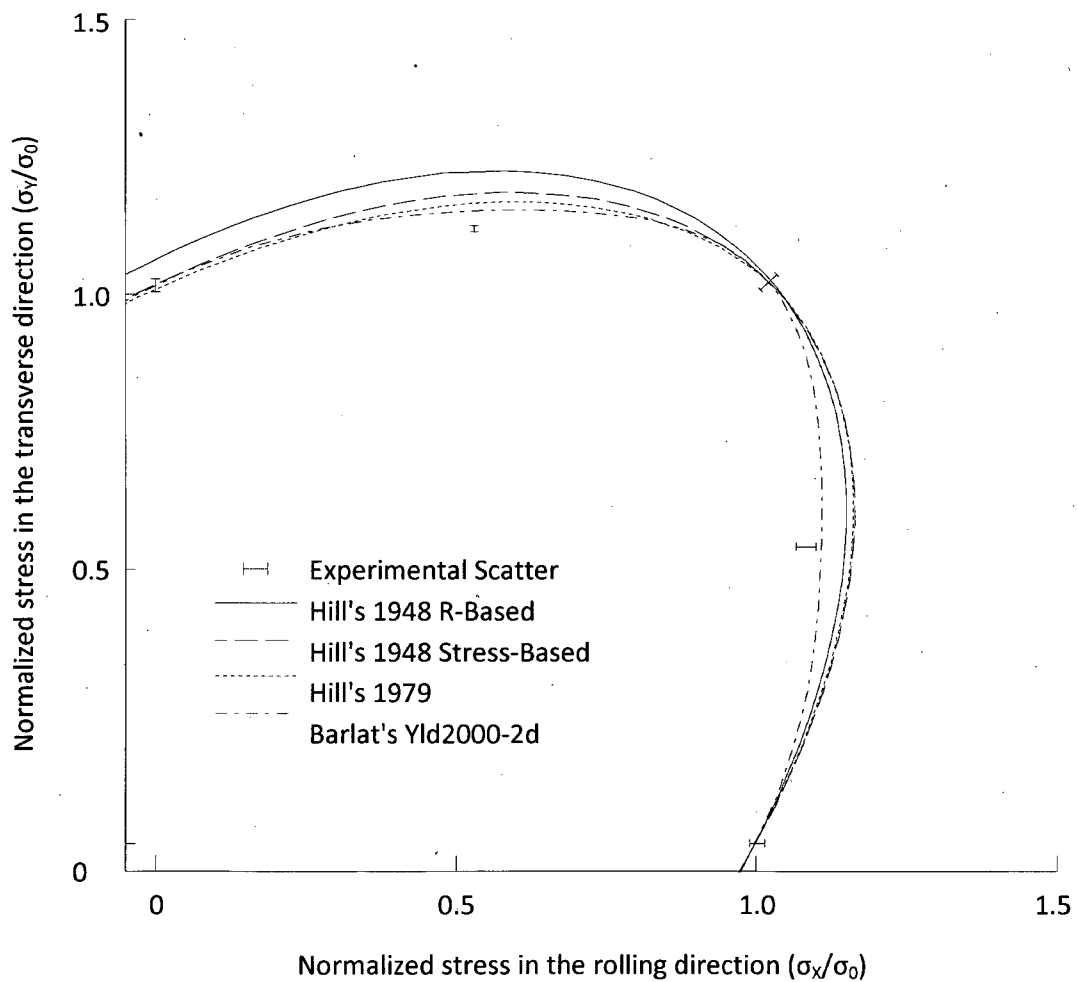


Figure 4.38 Yield loci in the σ_1 - σ_2 quadrant with error bars

It can be noted, that all yield functions over-predict the yield value in pure shear. While DP600 does not exhibit pure Tresca behaviour, the curvature of the yield functions causes them to over-predict

the yield stress in pure shear. It should be noted, however, that the yield functions only slightly over-predict yielding in pure shear. With the exception of the plastic work values of 0.870, Barlat's Yld2000-2d provides the most accurate representation of yielding in pure shear, while Hill's 1948 R-based yield function provides the worst prediction. Figures 4.39 and 4.40 provide a comparison between experimentally obtained flow stresses and stresses predicted by the various yield functions for plane-strain in the transverse direction and for simple shear.

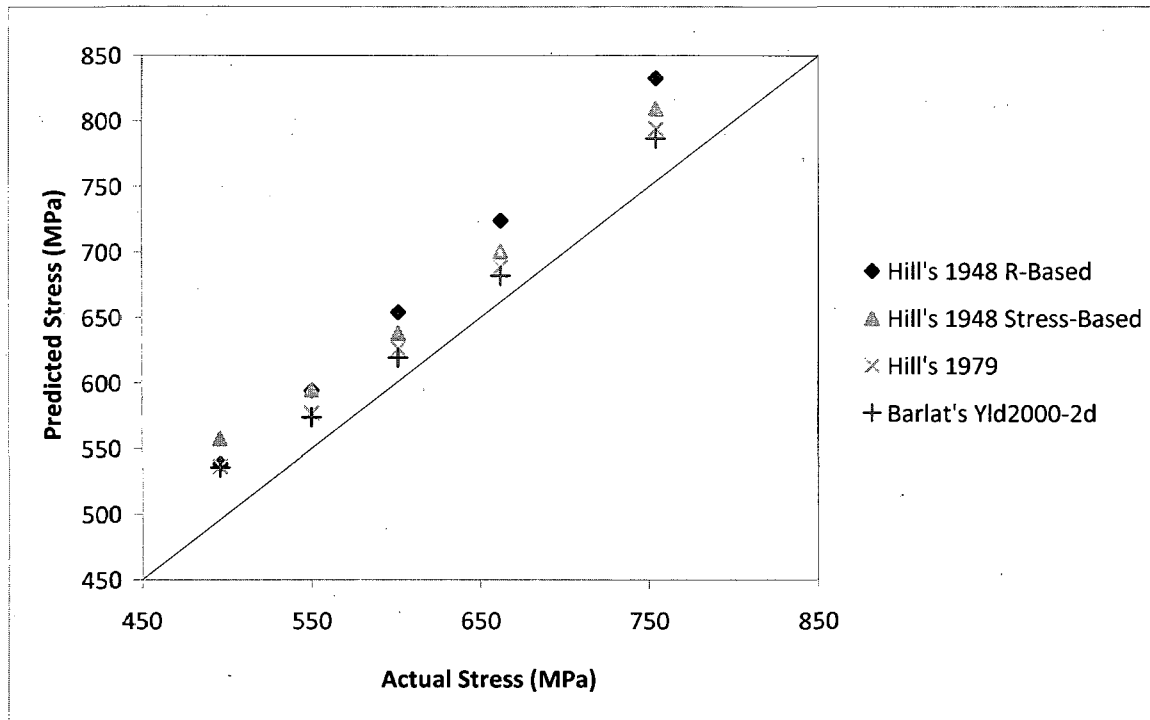


Figure 4.39 Comparison of experimental flow stresses to stresses predicted by the yield functions for plane-strain in the transverse direction

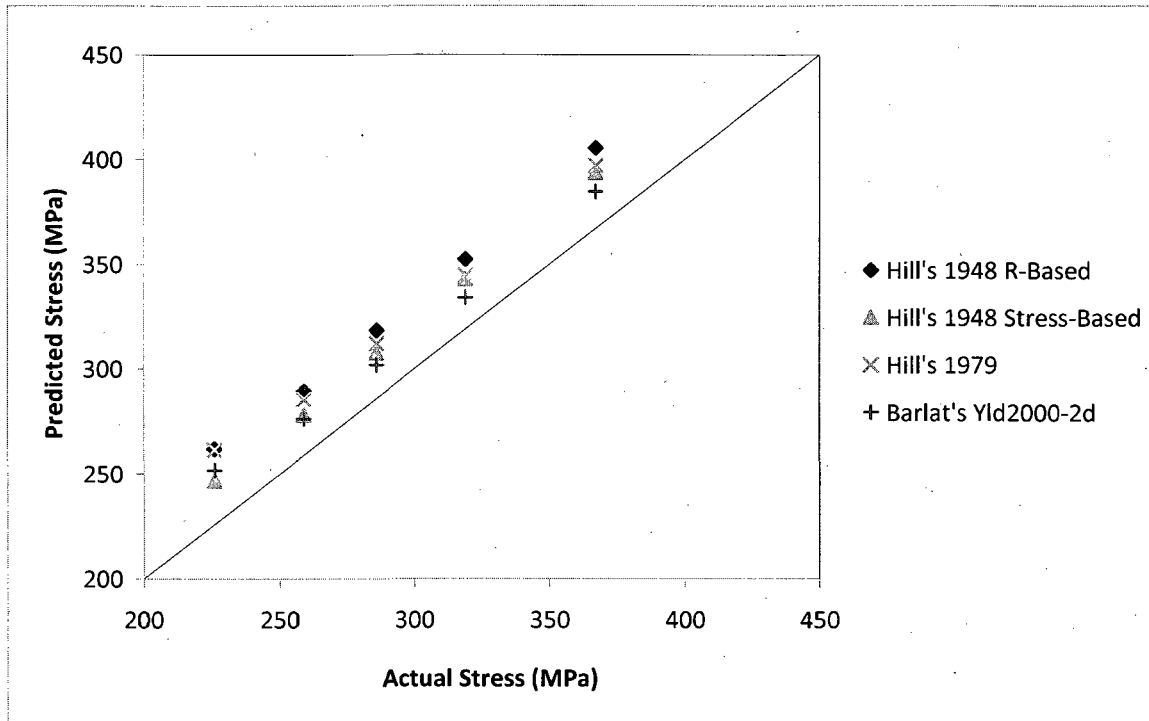


Figure 4.40 Comparison of experimental flow stresses to stresses predicted by the yield functions for simple shear

For levels of plastic work where the equibiaxial yield stress was less than the corresponding plane-strain values there is good agreement between the yield functions, however Barlat's Yld2000-2d can be observed to provide a more accurate over-all representation of the yield behaviour of DP600 specimens.

4.6.2 HSLA

Coefficients for Hill's 1948 stress based yield function are listed in Table 25, and anisotropy coefficients for Yld2000-2d are provided in Table 26.

	Plastic Work Per Unit Volume (MJ/m ³)				
Anisotropy Coefficient	0.918	4.22	8.34	20.9	44.4
F	0.4430	0.4022	0.3690	0.4148	0.4210
G	0.5672	0.5216	0.4837	0.4194	0.4568
H	0.4328	0.4784	0.5163	0.5806	0.5432
N	1.4949	1.5381	1.5736	1.5829	1.5611

Table 25 Anisotropy coefficients for Hill's 1948 stress-based yield function

	Plastic Work Per Unit Volume (MJ/m ³)				
Anisotropy Coefficient	0.918	4.22	8.34	20.9	44.4
α_1	0.9816	0.9377	0.8911	0.7963	0.8496
α_2	0.9260	0.9500	0.9754	1.1140	1.0593
α_3	0.9666	0.9037	0.8442	0.7618	0.8161
α_4	0.9374	0.9248	0.9123	0.9321	0.9330
α_5	1.0392	1.0197	1.0034	1.0064	1.0141
α_6	1.0634	0.9438	0.8417	0.8299	0.8850
α_7	1.0538	1.0417	1.0206	1.0815	1.0779
α_8	0.9474	0.9894	0.9995	1.1655	1.1228

Table 26 Anisotropy coefficients for Barlat's Yld2000-2d

For Hill's 1979 yield criterion, m values of 2.1580, 2.0263, 1.9213, 1.8943, and 1.9581 were obtained by fitting the shape of the yield locus to the experimental equibiaxial yield stress.

It can be observed that the Yld2000-2d α -coefficients for HSLA deviate from isotropy to a larger extent than DP600. This is evident from the greater range of in-plane R-values and from the true stress-true strain response of HSLA.

The effect of a wide range of in-plane R-values of HSLA compared to DP600 is evident in Hill's 1948 R-based yield function. The greater R-values at 90 degrees cause an elongation of the yield locus in the transverse direction. However, this elongation causes Hill's 1948 R-based yield function to over-predict the yield stress in the transverse direction. This elongation also results in Hill's 1948 R-based yield function providing the worst prediction in pure shear.

At the uniaxial tension yield offset of approximately 5.0%, a similar true stress-true strain response is noted in the rolling and transverse directions. This can be seen by the similarity between Hill's 1948 stress based yield function and Hill's 1979 planar isotropic yield function. For yield offsets below 5.0%, the anisotropic behaviour of HSLA is evident through the deviation between Hill's 1948 stress based yield locus and Hill's 1979 yield locus.

As shown in Appendix C (Figures A.8 and A.9), Hollomon and Voce equations are unable to accurately represent yielding behaviour at lower strains in equibiaxial tension. The error associated with low-level stress-strain response, resulted in equibiaxial yield stress values greater than the corresponding plane-strain values. This error leads to a slightly exaggerated elongation of the yield locus at lower levels of plastic strain.

As with DP600, the Yld2000-2d locus exhibits behaviour similar to Tresca's yield locus in the vicinity of plane-strain tension, and as a result, provides a more accurate representation of plane-strain tension than Hill's 1948 stress-based yield function. For larger values of plastic work Figure 4.41 shows that, while Yld2000-2d is able to predict the yield stress in plane-strain reasonably accurately, it nevertheless over-estimates the experimental plane-strain yield condition in the rolling and transverse directions.

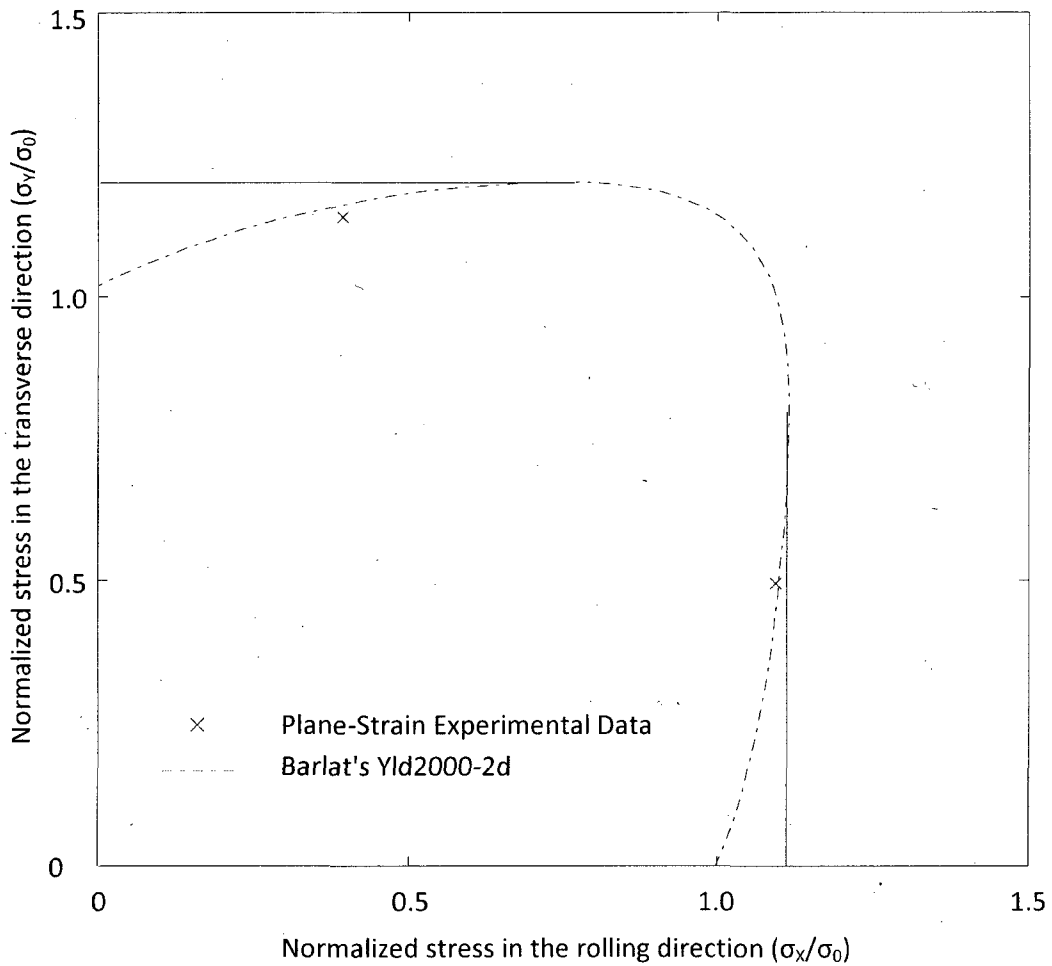


Figure 4.41 Comparison of Yld2000-2d plane-strain prediction to experimental results

A comparison between experimentally obtained flow stresses and stresses predicted through the yield functions for plane-strain in the transverse direction and simple shear is provided in Figures 4.42 and 4.43, respectively.

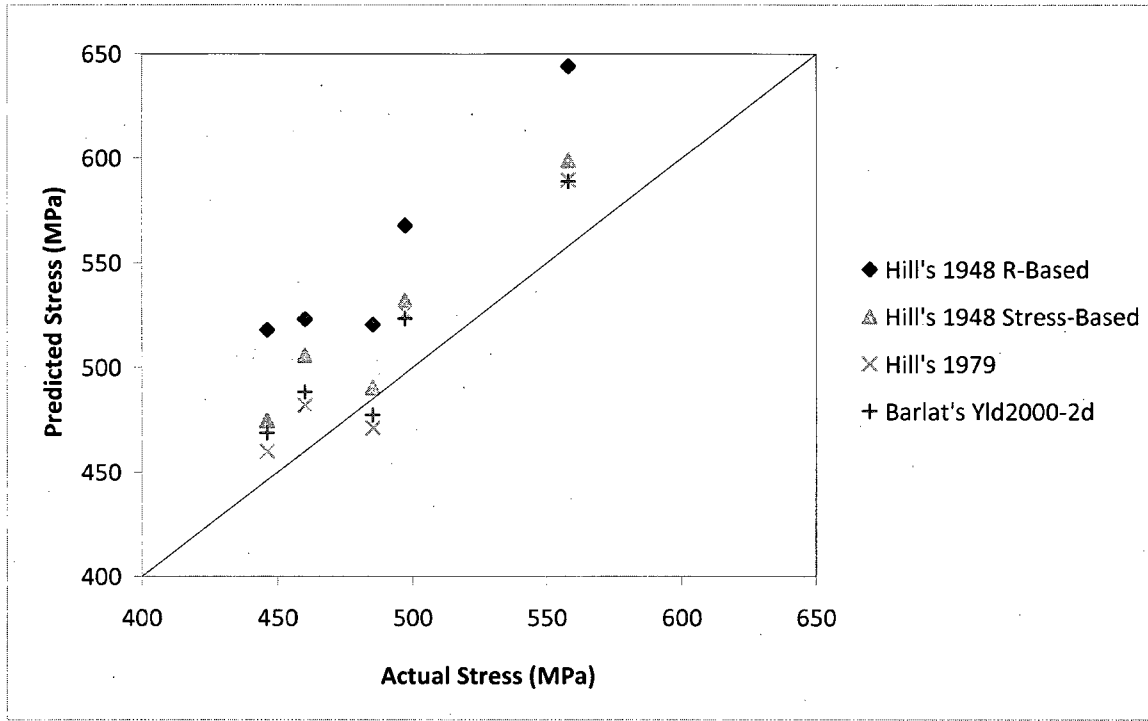


Figure 4.42 Comparison of experimental flow stresses to stresses predicted using yield functions for plane-strain in transverse direction

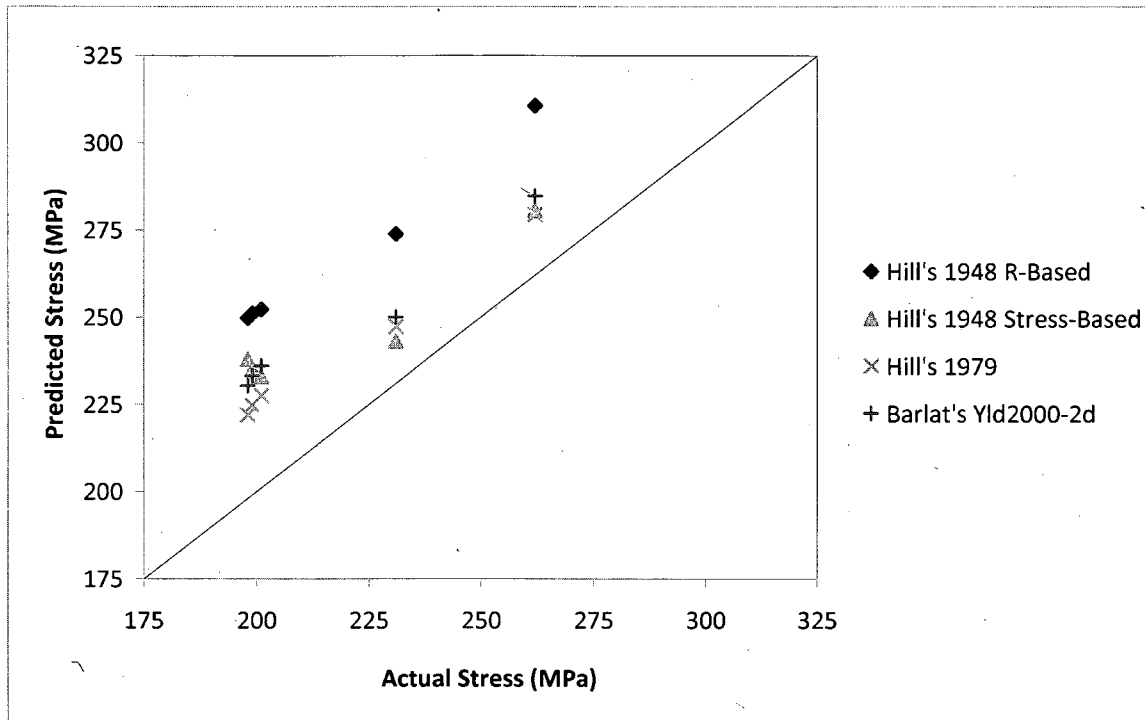


Figure 4.43 Comparison of experimental flow stresses to stresses predicted using yield functions for simple shear

Due to a more pronounced in-plane anisotropy evidenced by the range of R-values, neither Hill's 1948 R-based yield function nor Hill's 1979 planar isotropic yield function, are able to accurately represent the yielding behaviour of HSLA. Although Figures 4.42 and 4.43 indicate that Hill's 1979 yield function consistently provides a more accurate representation of the transverse plane-strain and simple shear responses, it can be observed in Figures 4.33 - 4.37 that this yield criterion consistently over-predicts the plane-strain results in the rolling direction, and under-predicts the yield stress in uniaxial tension in the transverse direction for yield offsets below 5.0%. Due to the ability of Yld2000-2d to more accurately predict plane-strain behaviour, it is considered to provide the best representation of HSLA behaviour.

5. CONCLUSION

The yielding and work hardening behaviour of two anisotropic steel sheets (DP600 and HSLA) were experimentally determined. Uniaxial tension and compression and plane-strain tension tests were carried out along the rolling and transverse directions of each sheet, and the use of DIC allowed for experimental determination of the strain distribution throughout the gauge region. The yield stresses in each deformation mode were determined for various levels of plastic work from the stress-strain response. Theoretical anisotropic yield criteria were evaluated against the experimental yield data obtained.

DP600 was observed to exhibit ductile behaviour. A low degree of anisotropy was also noted for DP600, as evident by the yield stresses and R-values. HSLA was observed to exhibit yield point elongation, and this behaviour was observed in every deformation mode. HSLA was also noted to exhibit a greater degree of in-plane anisotropy than DP600, as observed from both the yield stresses and R-values obtained.

A comparison of the experimental and numerically predicted strain distribution in plane-strain specimens provides a degree of confidence in the results obtained. The use of DIC to obtain the complete strain distribution in the specimen provides more strain data than would be obtained through the use of other strain measuring techniques.

Comparison of the stress-strain response of plane-strain specimens for both DP600 and HSLA showed a good correlation between results predicted with the help of LS-DYNA simulations and those estimated through Wagoner's analysis procedure. It is expected that the stress-strain curves predicted with LS-DYNA (and scaled down so that the predicted loads corresponded with the experimental loads) provided a reasonably accurate representation of the stress-strain response in plane strain. Indeed, numerically predicted stress and strain values were obtained from a single centrally located element, while Wagoner's analysis obtained a prediction of the plane-strain

response along a large portion of the gauge-area; however, the good correlation between both predictive methods provides confidence in the results obtained.

Experimental results for uniaxial compression tests showed relatively poor repeatability, and specimen buckling occurred at lower loads than predicted. The use of adhesive bonding of multiple specimens in an attempt to increase the critical buckling load was unsuccessful. Despite the wide range of yield stresses obtained in these uniaxial compression tests, a good correlation was observed with the average values obtained from tests carried out at Ohio State University with an anti-buckling support fixture. Once again, this correlation with third-party data provides a measure of confidence in the experimental results obtained.

Hill's 1948 yield criterion (both R-based and stress-based), Hill's 1979 planar isotropy criterion, and Barlat's Yld2000-2d anisotropic yield function were evaluated against the experimental yield data. For DP600, all yield functions provided a good description of the experimental yield data. Due to the increased planar anisotropy of the HSLA, only Hill's 1948 stress-based and Barlat's Yld2000-2d yield functions correlated with experimental yield data. While there is good agreement between Hill's 1948 R-based and stress-based yield functions for DP600, this was not the case for HSLA. Finally, it was observed that, for both DP600 and HSLA materials, Barlat's Yld2000-2d yield criterion was the most accurate of those evaluated in this work. While the degree of anisotropy was low for materials tested, it can be assumed that Barlat's Yld2000-2d would continue to provide a more accurate representation of yielding behaviour for materials with a higher degree of anisotropy.

Future work in this area should consider obtaining the stress-strain response for uniaxial compression specimens at larger strain values using digital image correlation. This can be achieved through the design of a support fixture which does not interfere with the acquisition of images for strain measurements. Also, an analysis of the evolution of the yield locus under non-proportional or reverse loading (e.g. to account for the Bauschinger effect) would help to increase the accuracy of material models used to simulate complex forming processes.

APPENDIX A

ARAMIS SPECIFICATIONS

SYSTEM SPECIFICATIONS

Processor: AMD Opteron 2x2.4 GHz (64-Bit) with 8GB RAM

Trigger-box Input: 12 bit analog, with +/-10V range.

Camera Resolution: 1280 x 1024 pixels

Lenses: 50mm macro Schneider Kreuznach lenses

CALIBRATION PARAMETERS

The calibration parameters are shown in Table A.1, with base length and measuring distance corresponding to Figure A.1. Measurement values were obtained from the users manual for ARAMIS v5.4.1 [46].

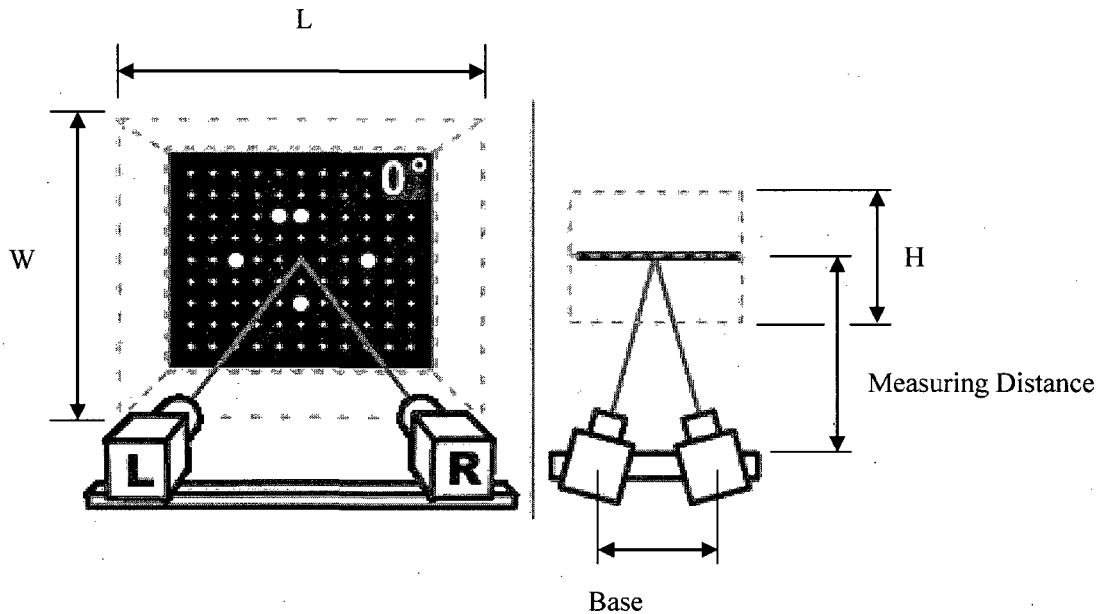


Figure A.1 Calibration set-up

Specimen	Calibration Volume (L x W x H)	Base Length	Measuring Distance
Uniaxial Tension	65 x 52 x 52 mm	240 mm	510 mm
Plane Strain Tension	135 x 108 x 108 mm	400 mm	960 mm
Uniaxial Compression	35 x 28 x 28 mm	130 mm	305 mm

Table A.1 Calibration parameters

CALCULATION PARAMATERS

The computation size value represents the number of adjacent points used in the calculation of strain. A computation size of five indicates a 5x5 facet grid is used in strain calculations. Small computation size values allow for the calculations of strains near discontinuities and edges, while larger computation values provide a reduction in noise. The validity quote presents the percentage of adjacent points that are required for strain calculations. The facet size value represents the pixel width of a facet, and the facet step represents the number of pixels between the centre point of adjacent facets. A facet overlap is achieved when the facet step is smaller than the facet size. The values used during this research are listed below:

Computation size: 5

Validity quote: 75%

Facet size: 15 pixels

Facet step: 13 pixels

APPENDIX B

PLANE-STRAIN ANALYSIS

In order to relate plane-strain tension results obtained from numerical modelling to experimental results, a scaling factor was obtained based on the ratio of the experimentally measured load-strain response to the predicted values obtained from numerical results. In order to obtain a point-by-point scaling factor, a curve of best fit was applied to the experimentally obtained results, providing an interpolation to which strain values could be compared. The curve of best fit was obtained using TableCurve 2D. Curve fit and R^2 values are presented in this appendix. Equations were chosen based on accuracy of results and ease of implementation. Equations are presented in the form $y=f(x)$ where y represents applied load in Newtons, and x represents true strain.

DP600

Rolling Direction

Specimen 1

$$y = 25142.351 + 24054.753x \ln(x) - 70881.344x^{0.5} \ln(x) + 0.0036896108 \ln(x) / x^2$$

$$R^2=0.99913468$$

Specimen 2

$$y = 26617.56 - 45499.096x - 65044.412x^{0.5} \ln(x) + 0.0039187493 \ln(x) / x^2$$

$$R^2=0.99945116$$

Specimen 3

$$y = -44698.323 - 130159.78x^{0.5} \ln(x) - 9228.1113 \ln(x) - 0.033236804 / x^2$$

$$R^2=0.99918725$$

Specimen 4

$$y = 14860.254 - 1071443.6x^{1.5} - 193944.67/\ln(x) + 0.0046446532\ln(x)/x^2$$

$$R^2=0.99968246$$

Specimen 5

$$y = 26973.917 - 7207.8612x^{0.5} \ln(x) + 30719.97x^{0.5} - 222.54884/x^2$$

$$R^2=0.99907277$$

Transverse Direction

Specimen 1

$$y = 490442.02 - 486910.52e^x - 273636.77/\ln(x) + 0.0048278959\ln(x)/x^2$$

$$R^2=0.99959899$$

Specimen 2

$$y = 45381.443 + 4637793.6x + 28833665x^2 + 16732264x/\ln(x) - 0.80083985/x^{1.5}$$

$$R^2=0.99967298$$

Specimen 3

$$y = 79065.874 - 1756276.4x^3 - 968.81518(\ln(x))^2$$

$$R^2=0.99934913$$

Specimen 4

$$y = 43755.586 + 4898430.5x + 30251288x^2 + 17585420x/\ln(x) - 0.030972586/x^2$$

$$R^2=0.99959633$$

Specimen 5

$$y = 507171.21 - 506465 - 78e^x - 288973.43/\ln(x) + 0.0039725703\ln(x)/x^2$$

$$R^2=0.99957837$$

HSLA

Rolling Direction

Specimen 1

Yield Elongation Strain Range: 0.001835-0.031188

$$y = -107698.91 + 415000.12x\ln(x) - 9637.1008\ln(x) - 526127.49/\ln(x)$$

$$R^2=0.91867484$$

Work Hardening Strain Range: 0.031188-0.185237

$$y = 41592.632 - 153493.96x^{2.5} - 280.5964/x$$

$$R^2=0.99691269$$

Specimen 2

Yield Elongation Strain Range: 0.002063-0.033061

$$y^{-1} = 3.1888567e-05 + 0.00011204368x/\ln(x) - 8.5323753e(-13)/x^2$$

$$R^2=0.96936816$$

Work Hardening Strain Range: 0.033061-0.145374

$$y = 64299.51 - 97334.726x - 2638.6907/x^{1.5} + 197.87721\ln(x)/x^2 + 1123.0335/x^2$$

$$R^2=0.99605165$$

Specimen 3

Yield Elongation Strain Range: 0.001597-0.028433

$$y^{-1} = 3.1509055e(-05) - 0.00040748457x^2 + 1.2728628e(-11)/x^{1.5}$$

$$R^2=0.76435048$$

Work Hardening Strain Range: 0.028433-0.194125

$$y = -16908.177 - 1645171.9x - 2287018.1x^2 \ln(x) + 527182.03x^{0.5}$$

$$R^2=0.9972282$$

Specimen 4

Yield Elongation-1 Strain Range: 0.002046-0.014641

$$y = 205018.36 - 14003248x^{0.5} + 4.6311677e(08)x - 8.0060086e(09)x^{1.5} + 7.6347481e(10)x^2 - 3.8054422e(11)x^{2.5} + 7.7380901e(11)x^3$$

$$R^2=0.93037641$$

Yield Elongation-2 Strain Range: 0.014641-0.037813

$$y = \frac{33045.877 + 26299.45 \ln(x) + 6906.8813(\ln(x))^2 + 599.82184(\ln(x))^3}{1 + 0.79562216 \ln(x) + 0.20891721(\ln(x))^2 + 0.018142273(\ln(x))^3}$$

$$R^2=0.99245076$$

Work Hardening Strain Range: 0.037813-0.231054

$$y = 40485.156 - 98326.945x^{2.5} - 47.640523/x^{1.5}$$

$$R^2=0.99768267$$

Specimen 5

Yield Elongation Strain Range: 0.003-0.033845

$$y = 42342.169 - 101596.19x \ln(x) + 72180.878/\ln(x)$$

$$R^2=0.96393796$$

Work Hardening Strain Range: 0.033845-0.191718

$$y^2 = -8.2652678e(08) - 3.0441162e(09)x^{0.5} \ln(x)$$

$$R^2=0.99626615$$

Transverse Direction

Specimen 1

Yield Elongation Strain Range: 0.002134-0.039802

$$y = -6.6160701e(08) - 6.6155435e(08)x - 3.3643035e(08)e(x) + 6.6164195e(08) - 0.00040523946 \ln(x) / x^2$$

$$R^2 = 0.98438514$$

Work Hardening Strain Range: 0.039802-0.194484

$$\ln(y) = 9.3736011 - 1.5791949x^{0.5} \ln(x) + 0.024123632 / x^{0.5}$$

$$R^2 = 0.98747471$$

Specimen 2

Yield Elongation Strain Range: 0.00252-0.033069

$$y = 34840.523 + 5177275.8x^{2.5} - 0.00033894353 \ln(x) / x^2$$

$$R^2 = 0.93164548$$

Work Hardening Strain Range: 0.033069-0.196681

$$y = 23388.932 + 6947.5469 / x - 1128.6982 / x^2 + 91.272209 / x^3 - 3.9474068 / x^4 + 0.086460307 / x^5 - 0.00075170979 / x^6$$

$$R^2 = 0.99733449$$

Specimen 3

Yield Elongation Strain Range: 0.003226-0.032087

$$y = 36674.077 - 8.2065443/x + 0.31119139/x^{1.5}$$

$$R^2 = 0.73181177$$

Work Hardening Strain Range: 0.032087-0.125483

$$y = -2.0786865e(08) + 6.748081e(09)x^{0.5} - 9.388627e(10)x + 7.1915877e(11)x^{1.5} \\ - 3.1728446e(12)x^2 + 6.9777481e(12)x^{2.5} + 1.617636e(12)x^3 - 5.3941077e(13)x^{3.5} \\ + 1.4576445e(14)x^4 - 1.7764068e(14)x^{4.5} + 8.6475468e(13)x^5$$

$$R^2 = 0.97628234$$

Specimen 4

Yield Elongation Strain Range: 0.00148-0.03836

$$y = 2.9686265e(-05) - 0.024727463x^3 + 2.1367907e(-07)\ln(x)$$

$$R^2 = 0.90835878$$

Work Hardening Strain Range: 0.03836-0.224617

$$y = 10.646712 - 2.7657645x^{2.5} - 0.0010934783/x^{1.5}$$

$$R^2 = 0.99622622$$

Specimen 5

Yield Elongation Strain Range: 0.002181-0.032666

$$y = 3.0212739e(-05) - 0.037000186x^3 - 5.6132916e(-08)/x^{0.5}$$

$$R^2 = 0.84407271$$

Work Hardening Strain Range: 0.032666-0.20352

$$y^{-1} = 2.4225787e(-05) + 0.00017089817x^3 - 4.2351203e(-08)\ln(x)/x$$

$$R^2 = 0.98614768$$

APPENDIX C

OUTSOURCED STRESS-STRAIN RESULTS

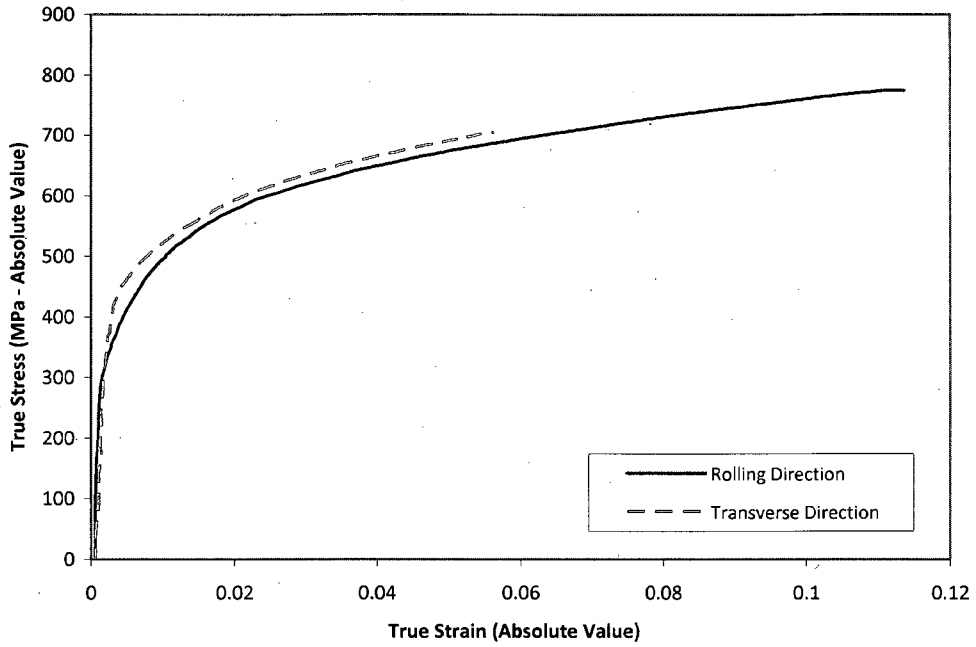


Figure A.2 True stress-true strain behaviour of DP600 in uniaxial compression (data provided by Dr Wagoner, Ohio State University)

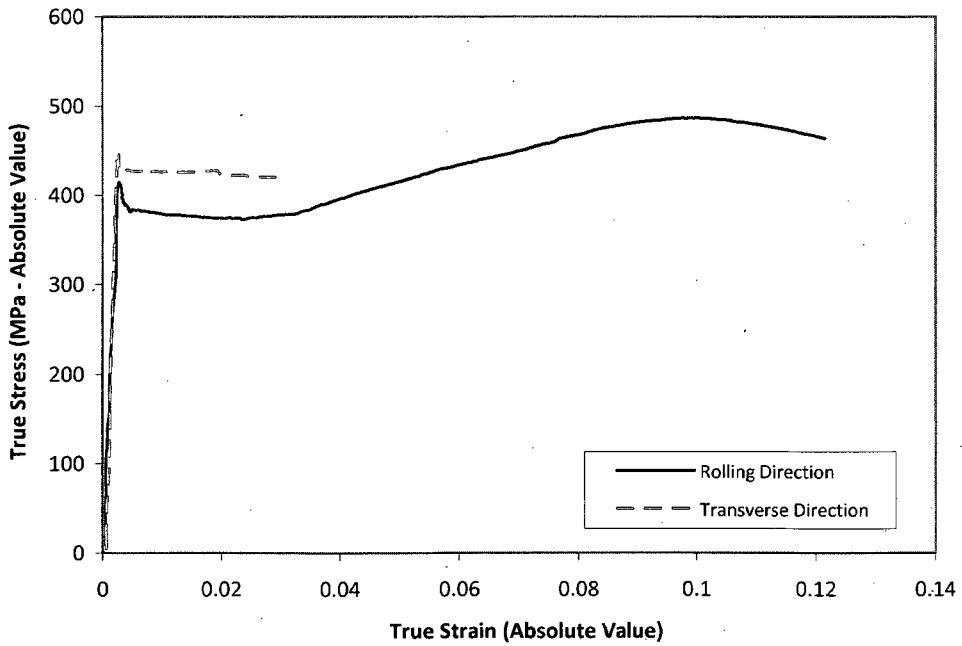
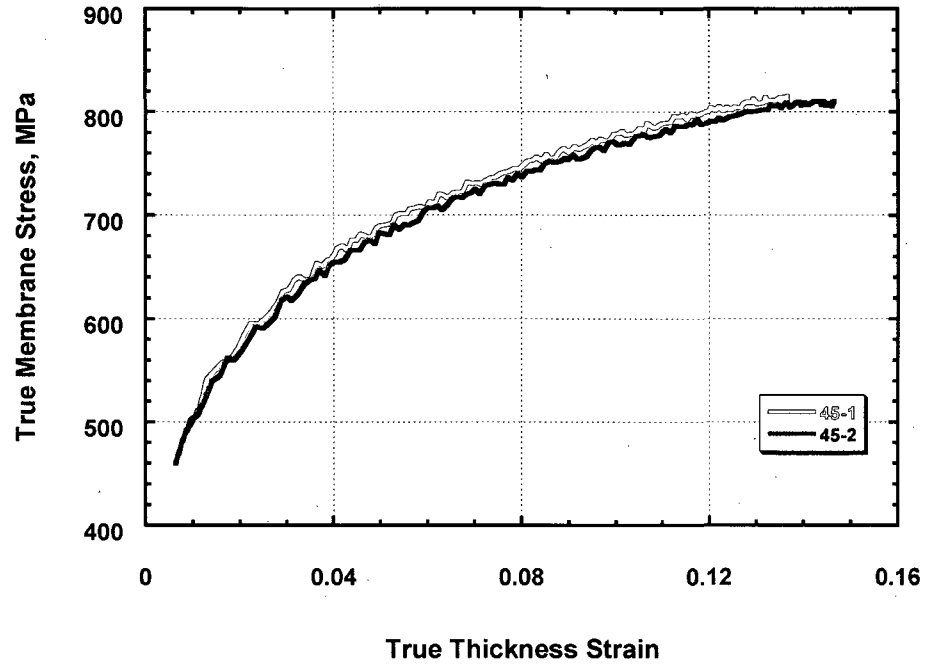


Figure A.3 True stress-true strain behaviour of HSLA in uniaxial compression (data provided by Dr Wagoner, Ohio State University)

**FIGURE 2. Equal Biaxial σ - ϵ Relationships
DP600 Steel Sheet - S.No. 842278**



**Figure A.4 Experimental true stress-true strain behaviour of DP600 in equibiaxial tension
(data provided by Dr Yoon, Alcoa Technical Centre)**

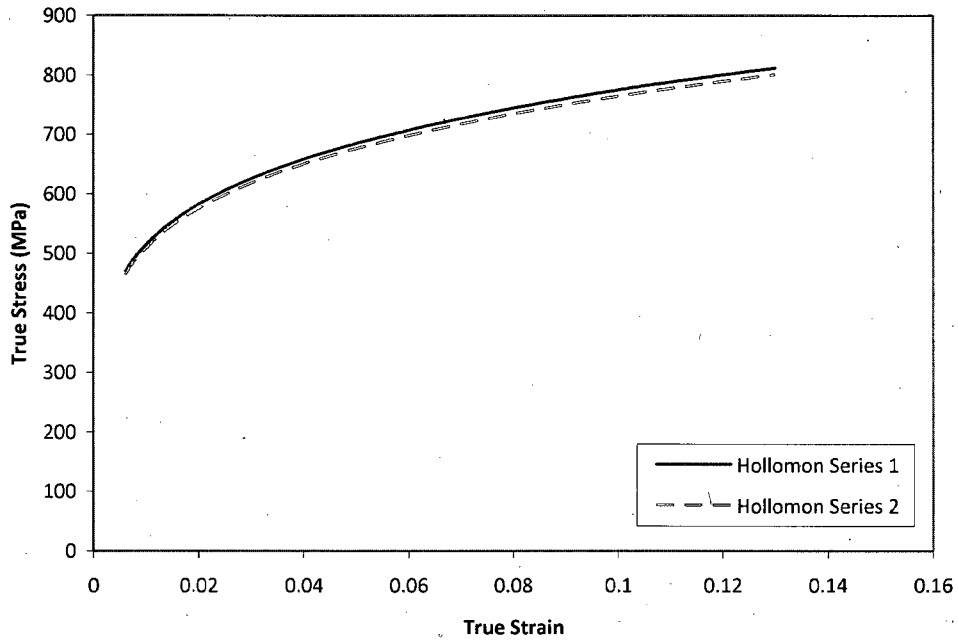


Figure A.5 Equibiaxial work hardening behaviour of DP600 described by Hollomon's law and fitted to experimental data

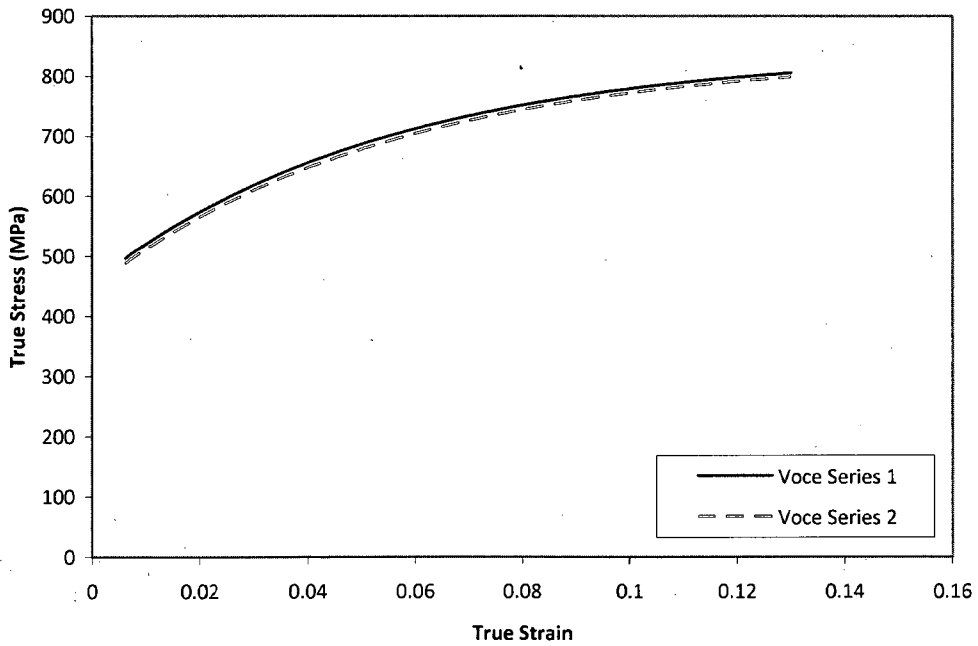
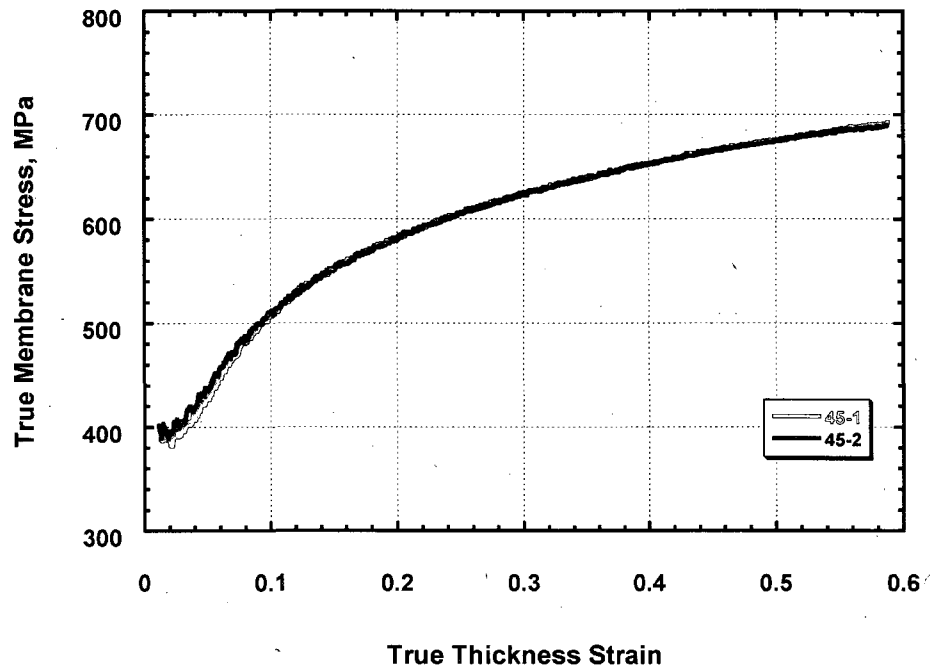


Figure A.6 Equibiaxial work hardening behaviour of DP600 described by Voce's law and fitted to experimental data

**FIGURE 3. Equal Biaxial σ - ϵ Relationships
HSLA Steel Sheet - S.No. 842279**



**Figure A.7 Experimental true stress-true strain behaviour of HSLA in equibiaxial tension
(provided by Dr. Yoon, Alcoa Technical Centre)**

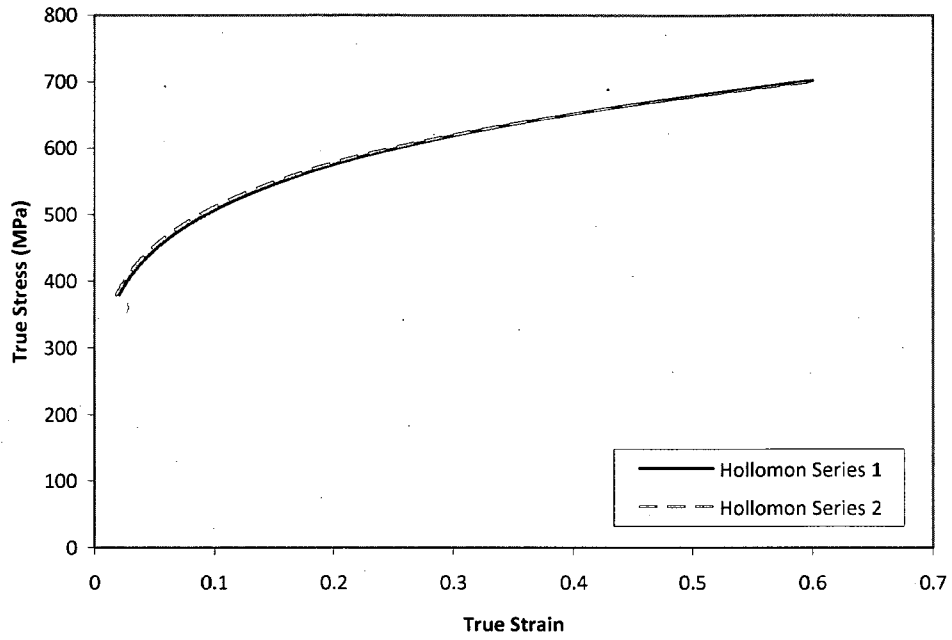


Figure A.8 Equibiaxial work hardening behaviour of HSLA described by Hollomon's law and fitted to experimental data

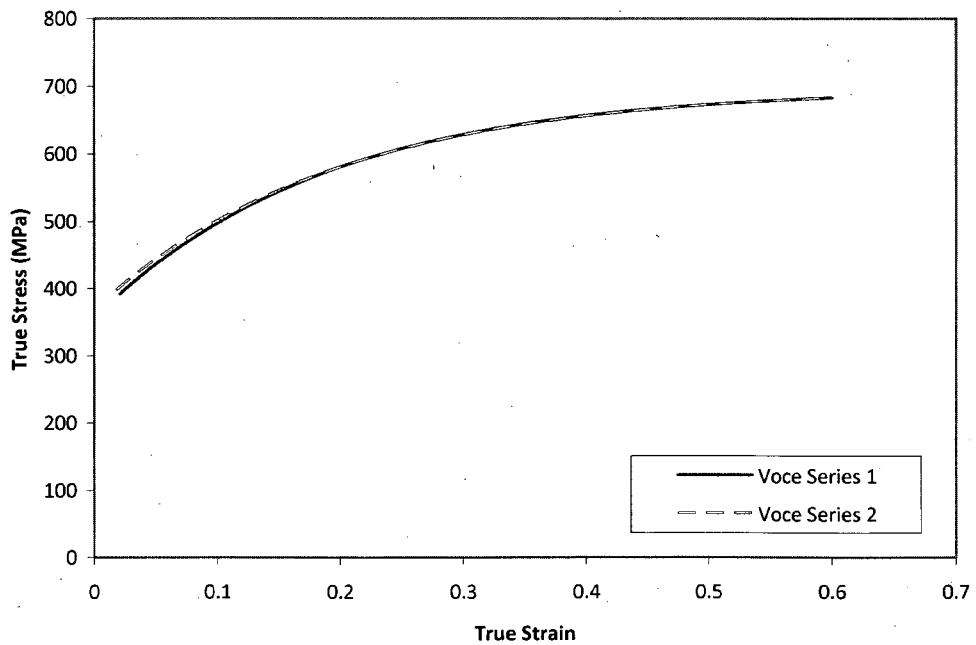


Figure A.9 Equibiaxial work hardening behaviour of HSLA described by Voce's law and fitted to experimental data

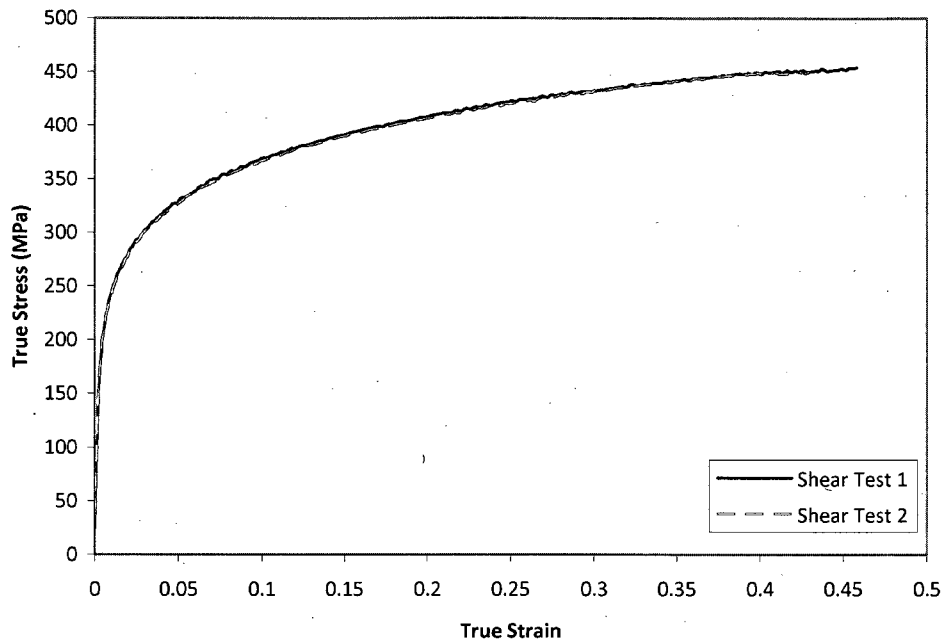


Figure A.10 True stress-true strain behaviour of DP600 in pure shear (data provided by Dr. Thuillier, Université de Bretagne-Sud)

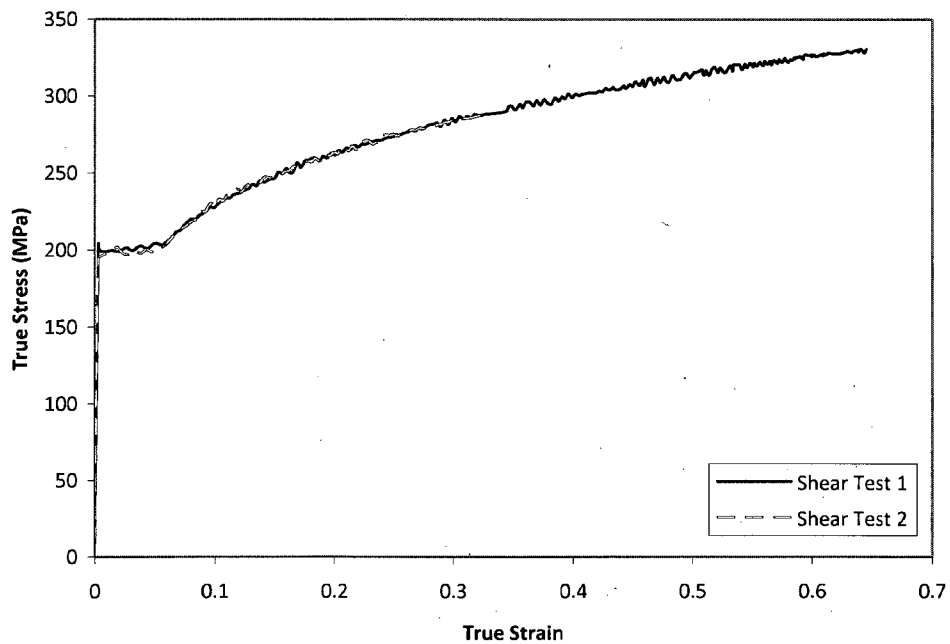


Figure A.11 True stress-true strain behaviour of HSLA in pure shear (data provided by Dr. Thuillier, Université de Bretagne-Sud)

REFERENCES

1. *UltraLight Steel Auto Body Final Report*. 1998, American Iron & Steel Institute.
2. Porsche Engineering Services Inc, *ULSAB Program Phase 2 Final Report*. 1998, Ultra Light Steel Auto Body Consortium.
3. International Iron & Steel Institute Committee on Automotive Applications, *Advanced High Strength Steel (AHSS) Application Guidelines*. 2006.
4. *Numisheet 2005 The Numisheet 2005 Benchmark Study*. in *AIP Conference*. Detroit, MI, U.S.A.
5. Wagoner, R.H., *Comparison of plane-strain and tensile work hardening in two sheet steel alloys*. Metallurgical Transactions A (Physical Metallurgy and Materials Science), 1981. **12A**(5): p. 877-82.
6. Taghvaipour, M. & Mellor, P.B., *Plane strain compression of anisotropic sheet metal*. Proceedings of the Institution of Mechanical Engineers, 1970. **185**(29): p. 593-606.
7. Hill, R., *A Theory of the Yielding and Plastic Flow of Anisotropic Metals*. Proceedings of the Royal Society of London. Series A, Mathematical and Physical Sciences, 1948. **193**(1033): p. 281-297.
8. Pearce, R., *Some aspects of anisotropic plasticity in sheet metals*. International Journal of Mechanical Sciences, 1968. **10**(12): p. 995-1006.
9. Parmar, A. & Mellor, P.B., *Predictions of limit strains in sheet metal using a more general yield criterion*. International Journal of Mechanical Sciences, 1978. **20**(6): p. 385-91.
10. Hill, R., *Theoretical plasticity of textured aggregates*. Mathematical Proceedings of the Cambridge Philosophical Society, 1979. **85**: p. 179-91.
11. Barlat, F., Brem, J. C., Yoon, J. W., Chung, K., Dick, R. E., Lege, D. J., Pourboghra, F., Choi, S. H. & Chu, E., *Plane stress yield function for aluminum alloy sheets - Part 1: Theory*. International Journal of Plasticity, 2003. **19**(9): p. 1297-1319.
12. Yoon, J.W., Barlat, F., Dick, R. E., Kwansoo, C. & Tae Jin, K., *Plane stress yield function for aluminum alloy sheets - part II: FE formulation and its implementation*. International Journal of Plasticity, 2004. **20**(3): p. 495-522.
13. Wagoner, R.H., *Measurement and analysis of plane-strain work hardening*. Metallurgical Transactions A (Physical Metallurgy and Materials Science), 1980. **11A**(1): p. 165-75.
14. Vegter, H., Ten Horn, C., An, Y., Atzema, E., Pijlman, H., Van Den Boogaard, T. & Huétink, H., *Characterisation And Modelling Of The Plastic Material Behaviour And Its Application In Sheet Metal Forming Simulation*. VII International Conference on Computational Plasticity, 2003: p. 20.

15. Wagoner, R. H. & Neng-Ming, W., *An experimental and analytical investigation of in-plane deformation of 2036-T4 aluminum sheet*. International Journal of Mechanical Sciences, 1979. **21**(5): p. 255-64.
16. Young, R. F., Bird, J. E. & Duncan, J. L., *Automated Hydraulic Bulge Tester*. Journal of Applied Metalworking, 1981. **2**(1): p. 11-18.
17. Green, D. E., Neale, K. W., MacEwen, S. R., Makinde, A. & Perrin, R., *Experimental investigation of the biaxial behaviour of an aluminum sheet*. International Journal of Plasticity, 2004. **20**(8-9): p. 1677-706.
18. Ferron, G. & Makinde, A., *Design and development of a biaxial strength testing device*. Journal of Testing and Evaluation, 1988. **16**(3): p. 253-6.
19. Makinde, A., Thibodeau, L. & Neale, K. W., *Development of an apparatus for biaxial testing using cruciform specimens*. Experimental Mechanics, 1992. **32**(2): p. 138-44.
20. Demmerle, S. & Boehler, J. P., *Optimal design of biaxial tensile cruciform specimens*. Journal of the Mechanics and Physics of Solids, 1993. **41**(1): p. 143.
21. Boehler, J. P., Demmerle, S. & Koss, S., *A new direct biaxial testing machine for anisotropic materials*. Experimental Mechanics, 1994. **34**(1): p. 1-9.
22. Hoferlin, E., Van Bael, A., Van Houtte, P., Steyaert, G. & De Mare, C., *The design of a biaxial tensile test and its use for the validation of crystallographic yield loci*. 2000. UK: IOP Publishing.
23. Shiratori, E. & Ikegami, K., *Experimental study of the subsequent yield surface by using cross-shaped specimens*. Journal of the Mechanics and Physics of Solids, 1968. **16**(6): p. 373-94.
24. Mueller, W. & Pohlandt, K., *New experiments for determining yield loci of sheet metal*. Journal of Materials Processing Technology, 1996. **60**(1-4): p. 643-648.
25. Kuwabara, T., Ikeda, S. & Kuroda, K., *Measurement and analysis of differential work hardening in cold-rolled steel sheet under biaxial tension*. Journal of Materials Processing Technology, 1998. **80-81**: p. 517-523.
26. Pohlandt, K., Lange, K., Banabic, D. & Schock, J., *Consistent parameters for plastic anisotropy of sheet metal (part 1-uniaxial and biaxial tests)*. 2007. USA: AIP.
27. Berg, J. S. & Adams, D. F., *An evaluation of composite material compression test methods*. Journal of Composites Technology and Research, 1989. **11**(2): p. 41-6.
28. Kotanchik, J. N., Woods, W. & Weinberger, R. A., *Investigation of methods of supporting single-thickness specimens in fixture for determination of compressive stress-strain curves*. 1945, National Advisory Committee for Aeronautics: Washington, DC, United States. p. 10.
29. Aitchison, C. S. & Tuckerman, L. B., *"Pack" method for compressive tests of thin specimens of materials used in thin-wall structures*. 1939, National Advisory Committee for Aeronautics (United States Advisory Committee for Aeronautics): Washington, DC, United States. p. 11.

30. Aitchison, C.S., *Extension of pack method for compressive tests*. 1940, National Advisory Committee for Aeronautics (United States Advisory Committee for Aeronautics), Washington, DC, United States. p. 6.
31. Moore, A. A. & McDonald, J. C., *Compression testing of magnesium alloy sheet*. American Society for Testing Materials -- Bulletin, 1945(135): p. 27-30.
32. Tian, H., Kang, D. & Lin, J., *Determining sheet metal hardening curve by laminated specimen*. Key Engineering Materials, 2004. **274-276**(1): p. 793-798.
33. ASTM E9 - 89a, *Standard Test Methods for Tension Testing of Metallic Materials*. 2002.
34. Yoshida, F., Uemori, T. & Fujiwara, K., *Elastic-plastic behavior of steel sheets under in-plane cyclic tension-compression at large strain*. International Journal of Plasticity, 2002. **18**(5): p. 633-659.
35. Boger, R. K., Wagoner, R. H., Barlat, F., Lee, M. G. & Chung, K., *Continuous, large strain, tension/compression testing of sheet material*. International Journal of Plasticity, 2005. **21**(12): p. 2319-2343.
36. Kuhn, H.A., *Uniaxial Compression Testing*. ASM Handbook Volume 8 Mechanical Testing and Evaluation, 2003.
37. Madden, J.B.C., *Method of testing thin sheet material in compression*. Journal of the Aeronautical Sciences, 1946. **13**(7): p. 346-352.
38. Kuwabara, T., *Advances in experiments on metal sheets and tubes in support of constitutive modeling and forming simulations*. International Journal of Plasticity, 2007. **23**(3): p. 385-419.
39. Miyauchi, K. *Stress Strain Relationship in Simple Shear of In-Plane Deformation for Various Steel Sheets*. in IDDRG. 1984.
40. Thuillier, S. & Manach, P. Y., *Comparison of the work-hardening of metallic sheets using tensile and shear strain paths*. International Journal of Plasticity. **In Press**.
41. Carbonnière, J., Thuillier, S., Sabourin, F., Brunet, M. & Manach, P. Y., *Comparison of the work hardening of metallic sheets in bending-unbending and simple shear*. International Journal of Mechanical Sciences. **In Press**.
42. Rao, K. P. & Mohan, E. V. R., *A unified test for evaluating material parameters for use in the modelling of sheet metal forming*. 2001. Seoul: Elsevier Science Ltd.
43. Rao, K. P. & Mohan, E. V. R., *A vision-integrated tension test for use in sheet-metal formability studies*. 2001: Elsevier Science Ltd.
44. Tyson, J.S., T. *Advanced Photogrammetry For Robust Deformation And Strain Measurement*. in SEM 2002 Annual Conference. 2002. Milwaukee, WI.
45. Orteu, J. J., Cutard, T., Garcia, D., Cailleux, E. & Robert, L., *Application of stereovision to the mechanical characterisation of ceramic refractories reinforced with metallic fibres*. Strain, 2007. **43**(2): p. 96-108.

46. GOM mbH, *ARAMIS User Manual*. 2005: Germany.
47. ASTM E8M *Standard Test Methods for Tension Testing of Metallic Materials*. 2002. p. 60-81.
48. Olsson, R., Iwarsson, J., Melin, L. G., Sjogren, A. & Solti, J., *Experiments and analysis of laminates with artificial damage*. *Composites Science and Technology*, 2003. **63**(2): p. 199-209.
49. Turton, N., Majumder, A., Altenhof, W., Green, D., Vijayan, V., An, H. & Jin, S. Y., *Numerical and Experimental Determination of Strains in the Vicinity of a Centrally Located Circular Discontinuity in AA6061-T6 Square Extrusions during Axial Crushing*, in *10th International LS-DYNA Users Conference*. 2008: Dearborn, Michigan USA.

Vita Auctoris

NAME	Neil Turton
PLACE OF BIRTH	Orillia, Ontario
YEAR OF BIRTH	1983
EDUCATION	St Mary's High School, Owen Sound, Ontario 1997-2002 University Of Windsor, Windsor, Ontario 2002-2006 B.A.Sc. University Of Windsor, Windsor, Ontario 2006-2009 M.A.Sc.